CLARKSON UNIVERSITY

Wave Propagation under Ice Covers

A Dissertation

By

Xin Zhao

Department of Civil and Environmental Engineering

Submitted in partial fulfillment of the requirements

for the degree of
Doctor of Philosophy, Civil and Environmental Engineering

November, 2014

Accepted by the Graduate School

_____ _____

Date Dean

The undersigned have examined the thesis entitled **"Wave Propagation under Ice Covers"** presented by **Xin Zhao,** a candidate for the degree of **Doctor of Philosophy in Civil and Environmental Engineering**, and hereby certify that it is worthy of acceptance.

Nov. 18, 2014
Date

Prof. Hayley Shen – Advisor

Nov. 17 2014
Prof. Brian Helenbrook – Examining Committee

Nov. 17, 2014
Prof. Hungtao Shen – Examining Committee

Nov. 17, 20014
Prof. Weiming Wu – Examining Committee

Nov. 18, 2014
Prof. Poojitha Yapa – Examining Committee*

*Chair of the examination committee

ABSTRACT

The operational ocean wave model needs a sea ice component to simulate the global ocean waves. Current ocean wave models treat ice covered regions crudely. The purpose of this thesis is to provide a unified continuum model for the wave ice interaction. Sea ice is constantly subject to environmental forcing. As a result, its physical appearance and mechanical properties vary dynamically. There are three existing classic wave ice interaction models: viscous layer, mass loading, and thin elastic plate models. Viscous layer models may be used to simulate grease ice, mass loading model is probably suitable for pancake ice, and thin elastic plate model may be used to describe a continuous ice sheet floating in water. This situation means that for different kind of sea ice we need different wave ice interaction models. Recently, a proposed viscoelastic wave ice interaction model synthesized the three classic models into one model. Under suitable limiting conditions this model converges to the three previous models. Based on this new development, the present study expands the viscoelastic model for wave propagation through two connected ice covered ocean regions. By doing so, the complete theoretical framework for evaluating wave propagation through various ice covers may be implemented in the operational ocean wave models. In this thesis, we introduce a three-layer viscoelastic model to include the eddy viscosity in turbulent boundary layer under the ice cover into previous viscoelastic model and the methods to calculate wave reflection and transmission. We also use recent results of a laboratory study to determine the viscoelstic model parameters with an inverse method. The thesis concludes with a numerical procedure for implementing the viscoelastic dispersion relation into the ocean wave model and some ideas of model parameterization.

ACKNOWLEDGEMENT

I would like to express my deepest gratitude to my advisor, Prof. Hayley Shen, who supports my Ph.D study and provides tremendous help during my stay at Clarkson. Thanks to my committee members, Profs. Helenbrook, H. T. Shen, Wu, and Yapa.

Thanks also to my family who have been extremely understanding and supportive of my studies. I would like to give my special thanks and deep love to my wife, Ms. You, who supports me all the time.

Also, I really appreciate the help from Dr. Ruixue Wang, Dr. Ian Knack, Mr. Fengbin Huang, Ms. Shanshan Sun, Mr. Jiajia Pan, Mr. Sukun Cheng, Mr. Jingkai Li, Ms. Yu Wang, Mr. Christopher Callinan and Mr. Chao Li.

Thanks to Mr.Sukun Cheng for the help on writing section 2.6.

The research reported in this thesis was supported by funds from the Office of Naval Research grant #N00014-13-1-0294. The support is gratefully acknowledged.

TABLE OF CONTENTS

LIST OF SYMBOLS

Symbol	Unit	Property
N	m/s	Wave action density spectrum
A	m/s	Incident or transmitted part of wave action density spectrum
B	m/s	Scattered or reflected part of wave action density spectrum
$\overline{B}$	m/s	Isotropic part of B
B'	m/s	Anisotropic part of B
E	m/s^2	Energy density spectrum of surface elevation
S	m/s^3	Source term in the ocean wave model
ω	$1/s$	Angular frequency
f	$1/s$	Wave frequency
T	s	Wave period
t	s	Time
k	$1/m$	Complex wave number
k_r, κ	$1/m$	Real part of wave number
k_i, q	$1/m$	Imaginary part of wave number, or wave attenuation
$\mathbf{k}$	$1/m$	Wave number vector
$\mathbf{U}$	m/s	Velocity vector
u	m/s	Velocity along x direction
v	m/s	Velocity along y direction
w	m/s	Velocity along z direction
c_g, V_g	m/s	Group velocity
c	m/s	Celerity

θ		Angle of wave direction
g	m/s^2	Gravitational acceleration
h	m	Ice thickness
b	m	Boundary layer thickness under ice cover
H	m	Water depth
ρ_{water}	kg/m^3	Density of water
ρ_{ice}	kg/m^3	Density of ice
ν_{ice}	m^2/s	Viscosity of ice
ν_t	m^2/s	Eddy viscosity
ν_e	m^2/s	Effective viscosity (combination of ice viscosity and shear modulus)
ν_p		Poisson ratio of ice
G	Pa	Shear modulus of ice
E	Pa	Young's modulus or elasticity of ice
p	N/m^2	Pressure
$\boldsymbol{\tau}$	N/m^2	Stress tensor
$\mathbf{S}$		Strain tensor
$\dot{\mathbf{S}}$	$1/s$	Strain rate tensor
I		Magnitude of incident wave
R		Reflection coefficient
T		Transmission coefficient
c_{ice}		Ice concentration
l_i	m	Ice diameter
α_s	$1/m$	Wave scattering attenuation

η	m	Wave surface elevation
φ	$1/s$	Potential function
ψ	$1/s$	Stream function

CHAPTER 1 INTRODUCTION

1.1 Overview

Wave propagation under sea ice covers is a key issue in contemporary marine science and engineering. Its significance may be explained from two perspectives: one from the wave modeling and the other from the ice modeling. Global wave climate has both environmental and engineering implications. It contributes to and is in turn influenced by all mass, momentum, and energy exchange between air and sea. Shipping, deep sea and offshore operations need accurate information of the wave condition. Forecasts and hindcasts of wave conditions have relied on wave models with a long history of development [1]. Because of the lack of economic needs and the negligible wave intensity in the polar regions, these wave models have focused on the lower latitudes. As the ice reduction accelerates in recent years, particularly in the Arctic region, wave intensity has dramatically increased [2]. Simultaneously increasing interests in economic development and environmental concerns in this region push for a wave model that may be applied in the ice covered seas.

From the ice modeling point of view, sea ice covers about 7% of the Earth's surface, or about 10% of the world's oceans. In the north, it is found in the Arctic Ocean and a few sub-Arctic seas. In the Antarctic, it occurs in various areas around the continent of Antarctica. Like wave models, sea ice models have had a long history of development as well [3]. The recent rapid decline of Arctic ice that exceeds all model predictions indicates that important processes are still missing from these models. One of such processes is the wave induced fracture of ice cover. Fractured ice covers effectively

increase their surface for heat exchange and hence the melting rate [4], which could accelerate ice reduction. In addition, waves may contribute to the dynamics of ice cover by causing it to drift [5] and raft [6]. To improve the existing sea ice models, we need to examine the missing wave effects.

At present, existing operational wave models can only treat ice covers crudely. For example, in WAVEWATCH III (WW3) [7], an ice cover is considered as a stepwise filter in such a way that the fraction of wave energy flux at any location varies linearly between 0 and 1, with two threshold values controlling this stepwise linear variation, both are related to the local ice concentration. The group velocity is assumed unaltered from the open water condition. This model was established at a time when the only available ice parameter was the ice concentration and the wave conditions in the Arctic were not of great concern. In reality, waves can penetrate into ice-covered seas over a very long distance. Along its passage, wave energy is dissipated by the ice field [8]. The attenuation rate depends on the wave period, ice concentration, thickness and floe size distribution [9-11]. In turn, waves may break the ice floes and further complicate their interactive nature [12]. In addition, wind-wave generation may be modified greatly in the presence of a partial ice cover [13, 14]. In view of the rapidly changing wave and ice conditions in the Arctic, there is an urgent need to improve the crude parameterization of wave propagation under sea ice. Integrating ice effects into wave models will advance wave predictions in ice-covered seas. With better remote sensing capabilities, information on ice conditions will improve. Wave models that can utilize this improvement need to be developed.

An ice covered region may be classified roughly into landfast ice, shear zone, and the marginal ice zone (MIZ). This classification is based on the distance from the coast. Farthest from the coast, the MIZ is adjacent to open water. In this zone, sea ice has significant dynamic behavior influenced by ocean waves. In turn, the wave field is also significantly modified by the presence of ice covers. For different kinds of ice covers, there are three classic models of wave propagation under an ice cover: mass loading [15, 16], thin elastic plate [17-20] and the viscous layer model [21, 22]. All these models can reflect some material properties of the sea ice. Wang and Shen [23] generalized these three models to synthesize them into one viscoelastic model. It is hoped that such generalized model may be able to smoothly bridge different types of ice covers by a proper parameterization scheme.

In the following chapters, we first briefly review the framework for a wave model with sea ice effect. We will focus on the dispersion properties of ice covers, the way they might change the wave speed and attenuate wave energy. Based on the recent viscoelastic models, we then discuss the transmission and reflection between ice covers of different material properties. Two mathematical approaches are introduced. The methods of implementation and parametrization for the viscoelastic model are discussed.

In the following sketch, we show the relations among chapters. To expand the ocean wave model by including the sea ice effects, we first need to know the ice morphology from remote sensing. With experimental and field study, we can bridge ice morphology and ice parameters, such as elasticity and viscosity. Inputing these parameters into the three-layer viscoelastic model, we can calculate wave attenuation and

reflection/transimission coefficients. With these results, the sea ice source term can be determined.

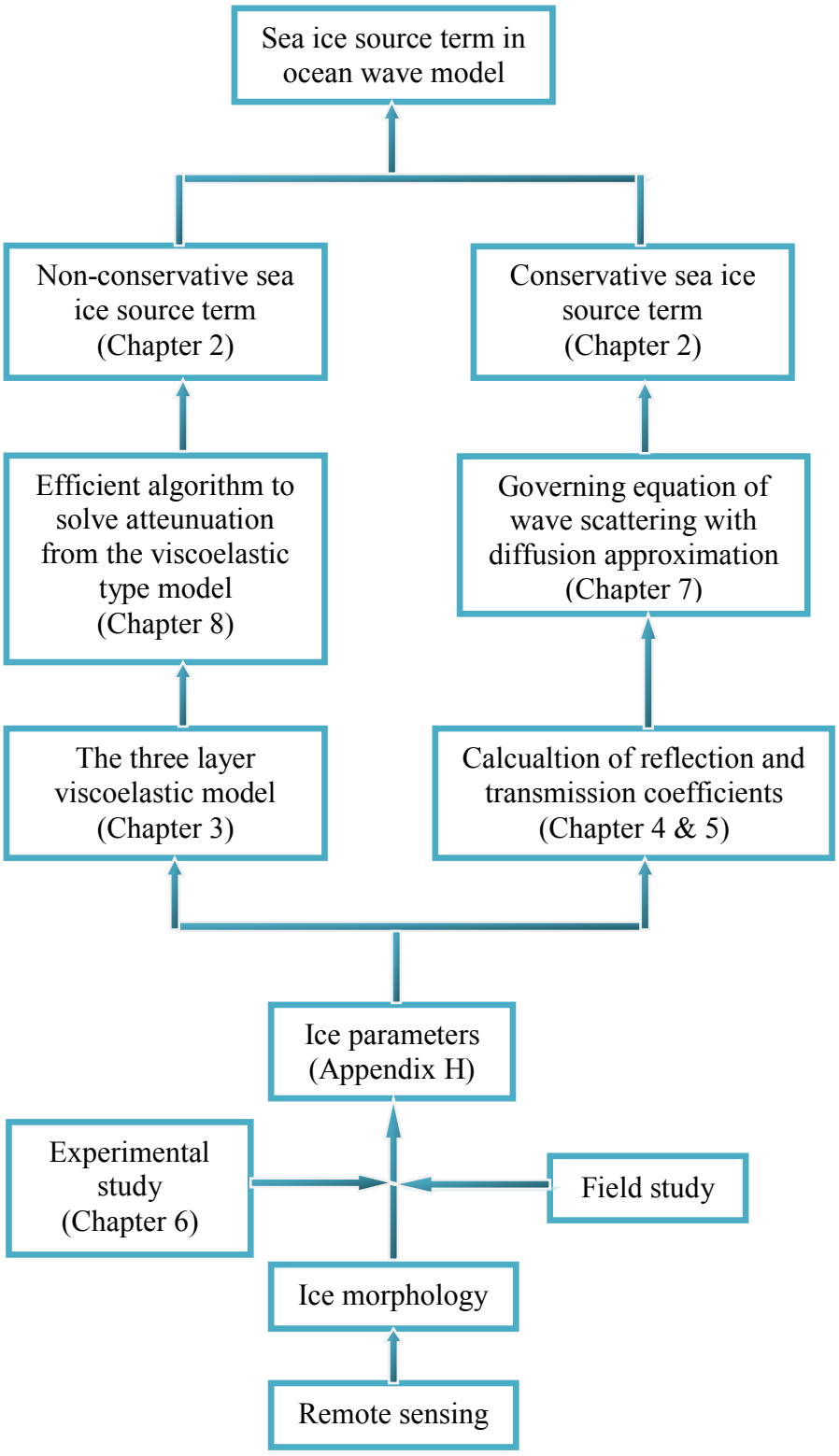

1.2 Research accomplishments

This thesis consists of eight completed tasks:

1. Reviewed previous theories and research on wave ice interaction;
2. Developed a three-layer viscoelastic model to generalize previous classic wave ice interaction models;
3. Designed an efficient numerical method to implement viscoelastic model into ice covered ocean wave model;
4. Investigated the reflection and transmission coefficients between two connected ice-covered ocean region using the approximate solution method;
5. Investigated the reflection and transmission coefficients between two connected ice-covered ocean region using the variational method;
6. Experimentally studied the wave propagation under ice covers;
7. Numerically simulated the gravitational waves of viscous and viscoelastic material in a rotating tank with large eddy simulation (LES) and level set method;
8. Governing equations for wave scattering by randomly distributed ice floes for global ocean wave model.

1.3 Contribution of the present research

The present theoretical study helps to build a comprehensive viscoelastic model capable of describing wave propagation through a variety of ice covers. This model is completed by an efficient algorithm interface with WW3, solving the energy transmission/reflection between different ice, using inverse method to determine the model parameters, unified the dissipation from water body and the ice cover into one single model.

CHAPTER 2 BACKGROUND

In this chapter we provide the background of ocean surface wave propagation under ice covers.

2.1 Operational ocean wave model

Ocean surface wave models are used to describe the evolution of the ocean wave energy generated by wind and modified by various transport and source/sink mechanisms. These models consider atmospheric wind forcing, nonlinear wave interactions, and dissipation. They output statistics describing wave heights, periods, and propagation directions for regional seas or global oceans. Such wave hindcasts and wave forecasts are extremely important for shipping and offshore construction interests, coastal management, and short or long term ecological and environmental evaluations.

For WW3, the governing equations for the wave state are [24]

$$\frac{\partial}{\partial t}N+\frac{\partial}{\partial x}\dot{x}N+\frac{\partial}{\partial y}\dot{y}N+\frac{\partial}{\partial k}\dot{k}N+\frac{\partial}{\partial \theta}\dot{\theta}N=\frac{S}{\omega} \tag{2.1}$$

$$\dot{x}=c_g\cos\theta+U_x \tag{2.2}$$

$$\dot{y}=c_g\sin\theta+U_y \tag{2.3}$$

$$\dot{k}=-\frac{\partial\omega}{\partial H}\frac{\partial H}{\partial s}-\mathbf{k}\cdot\frac{\partial \mathbf{U}}{\partial s} \tag{2.4}$$

$$\dot{\theta}=-\frac{1}{k}\left[\frac{\partial\omega}{\partial H}\frac{\partial H}{\partial m}-\mathbf{k}\cdot\frac{\partial \mathbf{U}}{\partial m}\right] \tag{2.5}$$

Where N is the wave action density spectrum, it equals to the energy density of the surface elevation divided by the angular frequency: $N=E/\omega$. Formally, N and S

depend on wave number k, direction θ, $\mathbf{k} = (k\cos\theta, k\sin\theta)$, the spatial coordinates $\mathbf{x} = (x, y)$ and time t; $N = N(k, \theta; x, y, t)$ and $S = S(k, \theta; x, y, t)$. $\mathbf{U} = (U_x, U_y)$ is the velocity vector of the current. Here $E = 2g|\hat{\eta}(\mathbf{k}; \mathbf{x}, t)|^2$, in which η is the surface elevation. H is the water depth, $c_g = \partial\omega/\partial k$ is the group velocity, s is a coordinate in the direction θ, m is a coordinate perpendicular to s, and S represents the net source term from wave generation and various dissipations. The source S contains several terms:

$$S = S_{in} + S_{nl} + S_{ds} + S_{ice} \tag{2.6}$$

Here, S_{in} is the energy input term from wind effect, S_{nl} is the nonlinear interaction term, S_{ds} is the dissipation term, and S_{ice} is the term due to sea ice effects.

2.1.1 Wind input term

The wind input term represents the energy transfer from air motion to water wave motion. The main issue for this term is how to derive the wave energy growth rate, γ_g.

$$S_{in} = \gamma_g N \tag{2.7}$$

Current ocean wave models are mainly based on linear or quasi-linear theories to estimate the wave energy growth rate. Such kinds of theories started from Miles [25] who developed a quasi-laminar approach to predict wind wave generation. This theory considered the resonant interaction between the wave-induced pressure fluctuations and the free surface waves and captured the main mechanism for wind wave generation. After Miles' theory, improvements were made to include the effect of boundary layer turbulence with mixing-length modeling or turbulent energy closure for calculating the

turbulent Reynolds stress [26-30]. For ice covered regions, the current models multiply this source term by the available free surface fraction.

2.1.2 Nonlinear wave-wave interactions term

The nonlinear wave-wave interactions play an important role in the evolution of ocean wave spectrum. The reason is that ocean waves are regarded most of the time as weakly nonlinear and dispersive. The vertical displacement of the free surface is still assumed with small amplitude. Therefore, the nonlinear wave governing equations are obtained by means of a perturbation expansion with starting point being the linear, freely propagating ocean waves. The evolution equations for wave action density spectrum were first derived by Hasselmann [31-33] with a quasi-normal assumption. Later, Zakharov [34] derived the evolution equations using the Hamiltonian variational approach [35]. No adjustment is made to this term in ice covered regions.

2.1.3 Dissipation term

The dissipation term describes the energy loss by continuous viscous dissipation and intermittent process of wave breaking. Different from laminar flow, turbulent motions and other organized motions such as Langmuir circulation may further enhance the dissipation. The key issue is to estimate the wave energy decay rate γ_d.

$$S_{ds} = -\gamma_d N \tag{2.8}$$

There are three main models for the dissipation term. The first model assumed that the dissipation as local in the spatial domain by Hasselmann [36]. In the second model, Phillips [37] assumed that the dissipation was local in the wavenumber domain. The third model from Jenkins [38] considered the effect of large scale ocean motions and ocean

turbulence with eddy viscosity. All of these models were constructed for open water. If one includes the effect of ice cover, the problem becomes more complex. In that case, the dissipation term and the ice term may have overlaps in the models. No theoretical work has been conducted on how the presence of ice may affect the above three models. In the current operational wave models, S_{ds} is multiplied by the fraction of open water for ice covered regions.

2.1.4 Ice term

There are two identified mechanisms that may change the forward propagating wave energy under ice covers: attenuation and scattering. Considering both mechanisms, the ice source may be split into two terms:

$$S_{ice} = S_{ice,c} + S_{ice,nc} \tag{2.9}$$

Where $S_{ice,c}$ is the term that describes the directional redistribution of wave energy by scattering. This is a conservative term. $S_{ice,nc}$ is the term that describes the wave energy dissipation due to ice cover. This is a non-conservative term. The non-conservative term can be modeled as the following [39]:

$$S_{ice,nc} / E = -2c_g k_i \tag{2.10}$$

Here k_i is the wave attenuation rate of the ice-covered ocean, and c_g is the group velocity of the wave propagating in the ice-covered ocean [40, 41]. The conservative term results from the wave scattering effect due to ice floes. As will be discussed later, this term is related to the wave reflection and transmission at any discontinuity of the ice cover. For $S_{ice,c}$, Masson and LeBlond [13] first derived the linear Boltzmann equation.

With the Green function method they calculated the scattering function due to rigid circular ice floes. They then used the result to study the wave spectra evolution by including wind energy input, wave breaking damping, and nonlinear wave interactions. Meylan et al. [42] developed another form of the linear Boltzmann equation to calculate wave scattering by circular ice floes. The derivations for the two models are compared in Meylan and Masson [43]. Masson and LeBlond's formulation was used by Perrie and Hu [14] together with another wave attenuation model proposed by Liu and Mollo-Christensen [41] to study wave spectra evolution including wind source, wave breaking, and nonlinear interaction. They compared the calculated wave amplitude change with field data reported in [44], in which, a roll-over phenomenon was observed, i.e. attenuation did not monotonically increase with wave frequency, instead, after some peak value, further increase of wave frequency resulted in decrease of the attenuation rate. Perrie and Hu [14] were able to demonstrate the roll-over effect with respect to wave frequency.

The non-conservative term $S_{ice,nc}$ comes from ice induced damping. There have been several mechanisms proposed in the past: eddy viscosity beneath the ice cover [41], inelastic hysteresis effects within the ice cover [45], and floe-floe collisions [46]. Each of these terms needs to be modeled.

In addition to these source/sink terms discussed above, the group velocity under different ice types has to be determined as well.

2.2 Types of sea ice covers

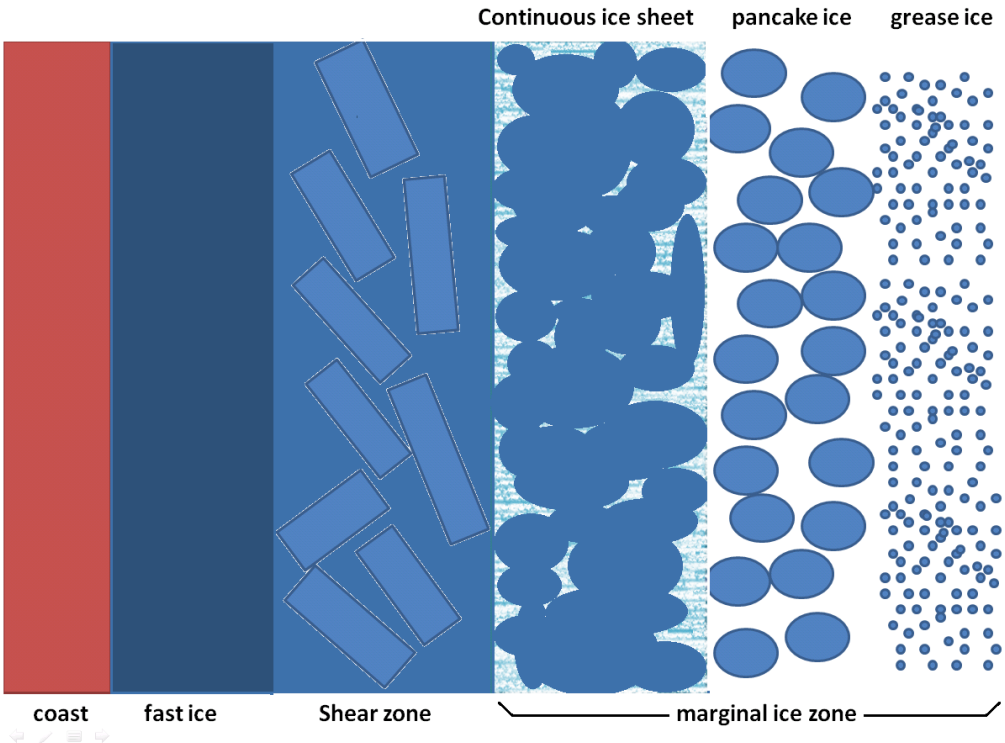

Fig. 2-1 Sketch on the spatial distribution of sea ice

As mentioned earlier, according to its proximity to land or sea, sea ice covers may be roughly divided into landfast ice (also called fast ice), the shear zone, and the marginal ice zone (MIZ), Fig. 2-1. Fast ice is frozen to the coast, often grounded by icebergs or ice ridges. In shear zone and the MIZ ice may drift. In the densely packed shear zone drifting causes divergence/convergence and shear. These large scale deformations create leads and ridges. In the marginal ice zone the ice thickness is relatively low, hence divergence/ convergence and shear do not change the surface morphology as significantly as in the shear zone. (See http://aspect.antarctica.gov.au/home/glossary-and-image-library, http://nsidc.org/gallery for examples of different ice types.) Here is the description of the three different sea ice zones from Wadhams [17]:

"Fast ice: This is ice which grows seaward from a coast and which stays in place throughout the winter, while breaking up, drifting away or melting in spring. The fast ice is stabilized by the presence of grounded pressure ridges in its outermost parts. Only long waves may travel into this region. All high frequency waves are generally attenuated before they arrive at the coast.

The shear zone: This ice forms when drifting pack ice moves against a coastal boundary which can be either fast ice or the land itself. The shearing and convergence of the pack's motion generates a band of highly deformed ice which has a higher density of ridging than the ice further out in the ocean. Waves that propagate into this region can be severely scattered due to the ridges.

The marginal ice zone (MIZ): the MIZ is that part of the ice cover which is close enough to the open ocean boundary to be affected by its presence. Ice in the MIZ has much greater freedom of movement than ice in the other two regions, and a number of ice-ocean-atmosphere interaction phenomena occur."

In the MIZ, due to the high wave energy, it is known that waves may fracture ice floes to change the floe size distribution. They may enhance frazil ice production by increasing heat transfer. They may regulate the pancake ice size, as well as causing floe rafting. Therefore, to model the ice-covered ocean dynamics in the marginal ice zone, we need to provide a wave ice interaction model.

The MIZ is usually divided into three distinct subzones [47]: the edge zone, the transition zone and the interior zone. In the edge zone, the intensity of waves is high and floes are relatively small, from a few millimeters for grease ice to few meters for pancakes. In the transition zone, the wave amplitude and wavelength is moderate after the

incoming wave energy is dissipated, floes sizes increase with increasing distance from the ice edge. In the interior zone, the incoming wave has been attenuated significantly so that no floe fracture occurs, the floe sizes increase abruptly to form a continuous sheet. The evolution from open water to grease ice to a continuous sheet is called the "pancake ice cycle" [48]. It is observed during the early formation season. Once formed, the continuous sheet can break during episodes of strong waves, or pressure variations and shear. After breaking, the open water part can form new grease/pancake ice. Very freshly broken cover is just a collection of polygonal floes. If no wind and no complex wave spectrum, only gentle swells, the ice floe aggregates may remain that way, with open water in between if no new ice growth and with grease/pancake gradually forming in between otherwise. If there is strong wave, the floes can be pulverized into brash ice. As ice edge advances further into the open sea, previously formed collections of ice floes, pancake or grease ice, all freeze together to become a continuous ice sheet. Continuous ice sheets are populated with cracks, ridges and leads due to wind and current actions. The morphology of an ice cover in the MIZ is thus dynamically changing.

2.3 Wave ice interaction model

There are three classic wave propagation models in the MIZ: mass loading model, thin elastic plate model and viscous layer model. For continuous ice sheet, the thin elastic plate model is probably a good model. Mass loading model can describe the disconnected pancake ice region, since pancake ice is very small relative to the significant wavelength. The viscous layer model is probably a good model for the grease ice region, because the dominant effect from grease ice is viscous damping. All three models are useful under specific ice conditions. However, field ice conditions are usually a mixture of these

distinct types. Hence in an operational ocean wave model it is desirable to have a unified formulation to simulate all types of sea ice. Motivated by this need, Wang and Shen [47] proposed a viscoelastic sea ice model to include all three classic models into one sea ice model.

2.3.1 Mass loading model

The mass loading model was the first model for wave propagation under a sea ice cover. This model was developed by Peters [15] and Weitz and Keller [16]. The ice floes are assumed to be mass points. The material properties of these mass points are irrelevant. The dispersion relation derived is,

$$\frac{\rho_{water}\omega^2}{\rho_{water}g - \rho_{ice}h\omega^2} = k\tanh kH\ . \tag{2.11}$$

Here, ρ_{water} is the density of water, ρ_{ice} is the density of ice, h is the thickness of ice, and H is the water depth. If the ice thickness goes to zero, the dispersion relation converges to the open water case when either the ice density or its thickness vanishes:

$$\omega^2 = kg\tanh kH\,. \tag{2.12}$$

2.3.2 Thin elastic plate model

The thin elastic plate model [17] assumed that the ice cover was a very thin uniform elastic layer so that the bending theory for a thin elastic plate may be applied. The dispersion relation is,

$$\frac{\rho_{water}\omega^2}{Lk^4 + \rho_{water}g - \rho_{ice}h\omega^2} = k\tanh kH \tag{2.13}$$

Here, $L = Eh^3 / 12(1-\nu_p^2)$ is the flexural rigidity, E is the elasticity, and ν_p is the Poisson ratio. If the rigidity goes to zero, the thin elastic plate model converges to the mass loading model. Squire [49] compared the difference between the two models.

2.3.3 Viscous layer model

The viscous layer model was first derived by Keller [21]. In this model, the ice cover was assumed as a layer of viscous fluid, and the water part was assumed as inviscid. The vertical velocity and stresses are matched along the interfaces of air-ice and ice-water. Using these equations together with the matched boundary conditions, Keller obtained the dispersion relation. Because for a given wave frequency this dispersion relation yields complex wave numbers, the model predicts wave attenuation directly. Later, De Carolis and Desiderio [22] developed a two-layer viscous fluid model by assuming water part as a viscous fluid. However, both Keller's model and the two layer model cannot predict the roll-over phenomenon observed in field data. Liu and Mollo-Christensen [41] assumed the ice layer as a thin elastic plate and water as a viscous fluid. The viscosity in water is assumed to be the eddy viscosity. The model is able to predict the roll-over phenomenon. The roll-over in spatial attenuation predicted from the model comes from the group velocity. The temporal decay rate from this eddy viscosity mechanism is in fact monotonically dependent on wave frequency.

2.3.4 Viscoelastic model

All three classic models discussed above do reflect the properties of some ice covers, but in practice ice covers are continuously changing in space and time. At any given location a mixture of different ice type may be present. It is therefore desirable to

have a unified theory that can smoothly change between ice types by varying some phenomenological parameters. With this motivation, Wang and Shen [23] developed a viscoelastic model to generalize all three models. The viscoelastic model is similar to viscous layer model, but the effective viscosity contains the elasticity part as the following,

$$\nu_e = \nu + iG/\rho_{ice}\omega\,. \tag{2.14}$$

Here, G is the shear modulus of ice layer, and ν is the viscosity of ice layer. The dispersion relation for wave propagation under a viscoelastic ice cover has been developed in Wang and Shen [23]. The resulting equation that relates the complex wave number to the wave frequency is obtained from setting the determinant of the following matrix to zero:

$$\begin{bmatrix} 0 & 2ik^2 & \alpha^2+k^2 & 0 \\ -2ik^2Sk & 2ik^2Ck & (\alpha^2+k^2)C\alpha & -(\alpha^2+k^2)S\alpha \\ N'\omega & -kg & ikg & L \\ -MSk+N'\omega Ck & MCk-N'\omega Sk & -iMC\alpha-LS\alpha & iMS\alpha+LC\alpha \end{bmatrix}. \tag{2.15}$$

In the above, $Sk=\sinh kh$, $Ck=\cosh kh$, $S\alpha=\sinh\alpha h$, $C\alpha=\cosh\alpha h$, $N'=\omega+2i\nu_e k^2$, $\alpha^2=k^2-i\omega/\nu_e$, and $M=\left(\frac{\rho_{water}}{\rho_{ice}}-1\right)kg-\frac{\rho_{water}}{\rho_{ice}}\frac{\omega}{\tanh(H-h)}$, and $L=2\nu_e\omega k\alpha$.

This determinant is

$$Det=\left(\omega^2-Q_c gk\tanh kH\right)\frac{\omega^2}{\nu_e^2}\frac{\rho_{water}}{\rho_{ice}}\frac{4k^3\alpha\nu_e^2SkC\alpha+N'^2S\alpha Ck-gkSkS\alpha}{\tanh kH}=0\,, \tag{2.16}$$

where

$$Q_c=1+\frac{\rho_{ice}}{\rho_{water}}\frac{g^2k^2SkS\alpha-(N'^4+16k^6\alpha^2\nu_e^4)SkS\alpha-8k^3\alpha\nu_e^2N'^2(C\alpha Ck-1)}{gk(4k^3\alpha\nu_e^2SkC\alpha+N'^2S\alpha Ck-gkSkS\alpha)}\,. \tag{2.17}$$

In Wang and Shen [2010] the above determinant was abbreviated to

$$\omega^2 = Q_c gk \tanh kH \,, \tag{2.18}$$

in order to directly compare with the open water, mass loading, thin elastic plate theories. In this dispersion relation, if we let shear modulus equal to zero, the viscoelastic model becomes Keller's viscous layer model.

Although the viscoelastic model provides a unified model for wave propagation under an ice cover, to apply the model is still a challenge. The problem is that the inputs of viscoelastic model are effective viscosity and effective shear modulus, which are the physical quantities of the sea ice region and cannot be measured directly. So far researchers have only used the inverse method to determine the model parameters for both viscous layer model and the thin elastic plate model [50-52]. Therefore, for the application of viscoelastic model, we need to establish a model to bridge the morphology of the ice cover to its effective viscosity and shear modulus through an inverse method. By directly measuring wave attenuation and wave speed change in an ice cover, through field or laboratory experiment, we solve for the viscoelastic parameters that can predict the observed wave property. In this way, we may establish the effective material properties of a given type of ice cover.

2.4 Wave attenuation

As discussed in subsection 2.1.4, to implement wave ice interaction model in an ocean wave model wave attenuation is a critical factor. Two wave attenuation mechanisms have been considered by researshers so far.

2.4.1 Viscous attenuation

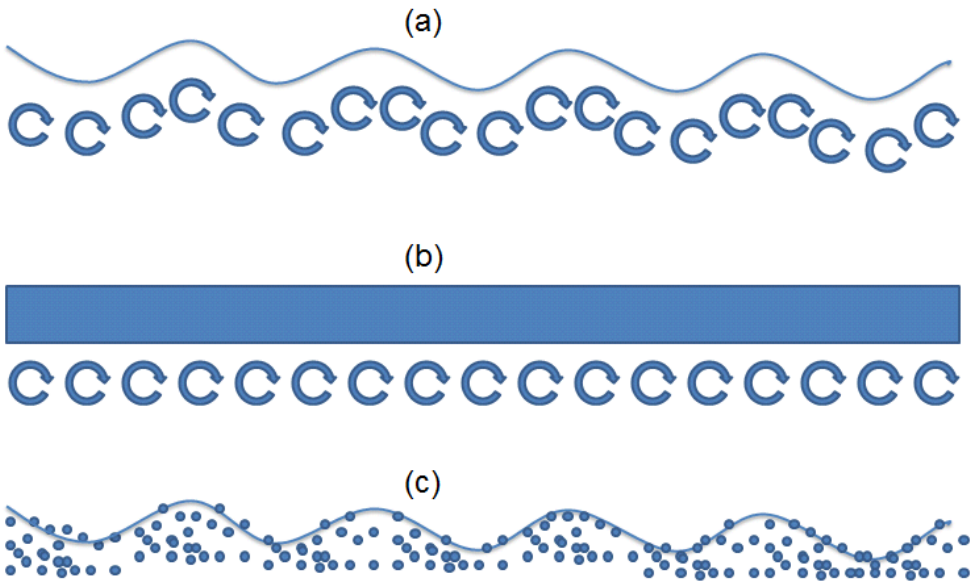

Fig. 2-2 Three mechanisms for viscous attenuation: (a) turbulence in the upper layer of the ocean; (b) boundary layer flows under ice cover; (c) interactions of ice particles.

As shown in Fig. 2-2, there are three main mechanisms for viscous wave attenuation: turbulence in the upper layer of ocean; boundary layer flows under ice cover; and collisions of ice particles.

The first mechanism is not related to ice cover. For the open water case, wave breaking and the subsequent generation of turbulence is the main cause of wave damping. This effect has been included in previous ocean wave models in the dissipation term. For partially ice covered region, due to the limited fetch, turbulence generation may be different from open water conditions.

The second mechanism is the boundary layer created beneath the rough ice cover. The third mechanism is the various interactions between ice particles or ice floes. The second mechanism is present for small ice particles as well when we consider the drag effect. The third mechanism is present for both large ice floes and small ice particles.

Whenever there is relative motion between neighboring ice particles or floes from wind, wave, current, or the drifting of the ice cover, interactions between neighboring floes may occur. These interactions transfer the mechanical energy of ice and water into incoherent motion of ice floes. The wave energy is thus attenuated. For grease ice, the size of ice particle is small, and the ice concentration is high. Therefore, the ice particle interaction frequency is high. This situation is analogous to the origin of viscosity in ordinary fluids, hence viscous layer model is a highly plausible model for grease ice.

Liu and Mollo-Christensen [41] suggested combine all attenuation mechanisms together into a phenomenological eddy viscosity and attributed all damping to the water body. However, a better approximation may be a thin turbulent boundary layer under the elastic or viscoelastic ice cover.

2.4.2 Scattering attenuation

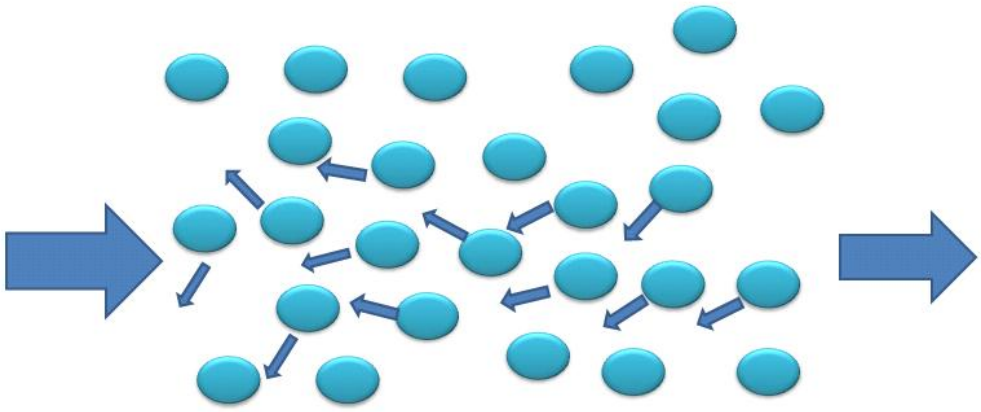

Fig. 2-3 Sketch of the scattering mechanism: large left arrow represents incident wave; large right arrow represents transmission wave; small arrows represent reflected waves; particles represent ice floes.

Wave scattering itself only redirects energy propagation. The total energy is still conserved. The measured attenuation in the wave propagation direction is always

influenced by wave scattering. Fig. 2-3 shows an example of wave scattering through an ice covered region. The ice floes reflect or scatter a part of wave energy from the incident wave, thus the transmitted wave energy is less than the incident wave. The reflected or scattered waves interact with each other. These incoherent interactions of multiple reflections from many floes are likely damped by the viscous effect. With this consideration, a viscous type of wave ice interaction model may also be suitable for the scattering attenuation by using a simple attenuation coefficient [17, 53, 54]. The viscosity for such a model may be very large (even larger than turbulent eddy viscosity), because the wave energy loss in the direction of the incident wave can be much large than direct viscous damping. This idea still needs further research. One can also keep the scattering term as the conservative term in the ice source term as discussed in section 2.4 and use the viscoelastic model to calculate the non-conservative term. In section 2.7, we will introduce some details about how to calculate wave scattering formally.

2.4.3 Wave attenuation formulations

Based on the above discussions, we have three methods to calculate the wave attenuation. The most direct method is to calculate the imaginary part of the root for viscous layer model or viscoelastic model. The imaginary part is the spatial viscous damping coefficient, i.e. the wave attenuation coefficient. The second method is from the thin elastic plate model. The wave attenuation from the viscous layer model and viscoelastic model comes from the effective viscosity. In the thin elastic plate model the sea ice part is pure elastic and water part is inviscid, there is no true wave attenuation. However, using wave scattering, Bennetts and Squire [53, 54] adopted a statistical method to calculate the change of forward propagating wave energy through a region of

ice floes. As mentioned earlier, the scattered wave energy is assumed to be attenuated rapidly from incoherent wave-wave interactions. The attenuation rate for scattering theory is calculated based on the remaining transmitted wave in the original wave direction. The third way to calculate wave attenuation also comes from thin elastic plate sea ice model, but for this method Liu and Mollo-Christensen [41] consider that the water part is viscous. Further, the effective viscosity is assumed to relate to the turbulence near the sea ice sheet.

2.5 Wave reflection and transmission

Wave reflection and transmission are physical processes that occur at any material interfaces. At floe scale, when the floe size is comparable with wavelength, the wave energy is split into transmitted part and reflected part at the open water and ice interface. This phenomenon is the basis of the wave scattering. There is another motivation for studying wave reflection and transmission: to mathematically model the wave propagation over a large expanse with varying physical conditions, a numerical method is required. All numerical methods discretize the computational domain into finite size "cells". The ice cover is connected at the cell boundary, and the change in properties is abrupt. Within each cell, average properties of variables are considered. A continuously varying ice cover is thus discretized into cells of different thickness and material properties. Wave damping mechanisms contribute to the sink term within each cell. At the boundary between neighboring cells wave flux contributes to the energy transport. Both damping and flux terms are required for any numerical wave models. Transmission and reflection at cell boundaries are in fact part of the cumulative results of this process that take place at the floe scale, where all discontinuities contribute to this process. The

types of floe scale discontinuities and their scattering properties are considered in scattering attenuation. Part of the cumulative results is accounted for in the wave attenuation due to the average properties of the ice within the cell. The part due to the gradient of the ice properties within the cell is accounted for at the cell boundary. These two processes are the sink term has been modeled as part of the dispersion relation in wave ice interaction models, and the flux term is the focus of the present section.

There are several methods to calculate the ocean wave reflection and transmission at the interface between two connected regions of open water or of different ice cover properties. In Squire and his colleagues' papers, they used the Green function method [55], matched eigenfunction expansion method [56, 57] and the variational method [18-20]. A more complete review of these methods can be found in Squire [11], which covers problems with the interfaces like: free ice edge, cracks, pressure ridges, refrozen leads, and abrupt change of ice thickness or the material moduli, all under the thin elastic plate assumption. Wang and Shen [58] employed an approximate solution method for open water connecting with a viscoelastic layer. The viscoelastic layer was finite with its own momentum equation. This method was extended to two connecting viscoelastic layer with different properties [59].

2.5.1 Exact solution method

The Green function method is a general method for solving non-homogeneous linear boundary value problems exactly. Sarpkaya and Issacson [60] provided details of this method and its applications in solving wave and marine structure interactions. This method is used in Meylan and Squire [55, 61] to determine the exact solution of a two-dimensional case with wave propagating under a finite size plate and a three-dimensional

case of a circular disk. In both cases the ice floe was assumed to be infinitely thin, where the boundary integral representation of the ice covered part was simple to treat.

The eigenfunction expansion method was developed by Fox and Squire [18, 19] for a free end condition case using the thin elastic plate model. The method was extended by Kohout [56] to calculate simple, springed, and hinged connections among ice plates. This method first expands the velocity potential of the wave motion into eigenfunctions. One selects a series of orthogonal basis functions. Candidates of the basis functions are trigonometric functions. They integrate the boundary condition equation with the basis function to obtain a linear system for transmission and reflection coefficients.

2.5.2 Approximate solution method

In [58], Wang and Shen truncated the infinite series of eigenmodes to include only two closest to the open wave mode. The evanescent modes and all other roots of the dispersion relation were dropped. They obtained the reflection and transmission coefficients assuming only these two modes carry the entire wave energy. They studied the ocean wave propagation from open sea water to a semi-infinite ice-covered ocean based on a viscoelastic model. They first expanded the general solutions with eigenfunctions, they then matched the mean values of the boundary conditions at the interface to form a homogenous linear system. With the singular value decomposition method, the transmission and reflection coefficients were obtained. They showed that by using the same physical parameters, this approximate method provided good agreement with previous more rigorous solution methods. Also, a mode switching phenomenon was found for the viscoelasitic model. With the increasing of shear modulus, the energy partitions between the first mode and second mode switch. For small shear modulus, the

first mode dominates, and for large shear modulus, the second mode dominates. Later, this approximate solution method is extended by Zhao and Shen [59] to calculate wave reflection and transmission at the interface of two connecting ice covered regions of different properties. This work is a part of the present thesis.

2.5.3 Variational method

The variational method is developed by Fox and Squire [18] to calculate wave reflection and transmission from open water to a semi-infinite elastic ice cover. The method is further extended by Barrett and Squire [20] to compute the case for two connecting ice covers. The key step for the variational method is to define the error function from the boundary condition equations. By minimizing the error function one may obtain the linear equations to solve for the reflection and transmission coefficients.

Zhao and Shen [62] also employed the variational formulations to calculate wave reflection and transmission with a viscoelastic model. This work is presented in chapter 5.

2.6 Wave scattering and floe breaking

Waves propagating into a sea ice field with sufficient amplitude can fracture a continuous ice sheet or a large floe into small ice floes, thereby reshape the ice cover morphology. Simultaneously, since floe size affects wave scattering and dissipation, the fracturing process also influences the wave propagation. As waves lose energy when propagating into an ice cover by various damping mechanisms, fracture is prevented in the interior ice. Hence floe size increases from the open ocean inward, usually with an abrupt change to a continuous sheet some hundreds of kilometers from the open ocean.

An extensive catalogue of theoretical literature exists in modeling the scattering process. According to different scattering scales, the mathematical models can be generally divided into small and large scale models.

For the former one, the focus is on solving both the hydrodynamics for the water part and the deformation field of the floe under a specified monochromatic incident wave. One standard short scale model is based on the assumption that an ice floe behaves as a single thin-elastic plate of negligible submergence. Meylan [63] proposed a solution by combining the boundary element method and finite element method for the scattering response of an ice floe with arbitrary shape. Small scale models of multiple ice floes are reported by Kohout and Meylan [64] and Kohout et al. [57]. The small scale models provide the scatting kernel which becomes the core part of the large scale models. An example of such theoretical results is shown in Fig. 2-4, using the analysis described in Meylan and Squire [61].

In ice covered ocean the waves have multiple periods and wavelengths. The scattering process for problems in this scale is described by large scale models. Under the linear wave theory, superposition of effects from each wave component is assumed. Masson and LeBlond [13] used the single floe scattering as the kernel to integrate over a field of ice floes, each acted as a scatterer to calculate for the wave energy transport. Another model is proposed by Meylan et al. [42] using wave transport equation as well. These two methods have shown to be almost identical by Meylan and Masson [43].

The same analysis developed in the small scale hydroelastic problems shown in Meylan and Squire [61] also provides the strain field inside the flexible ice floe. Such

information has been used in floe breaking models and integrated in large scale wave-ice interaction models [65-67].

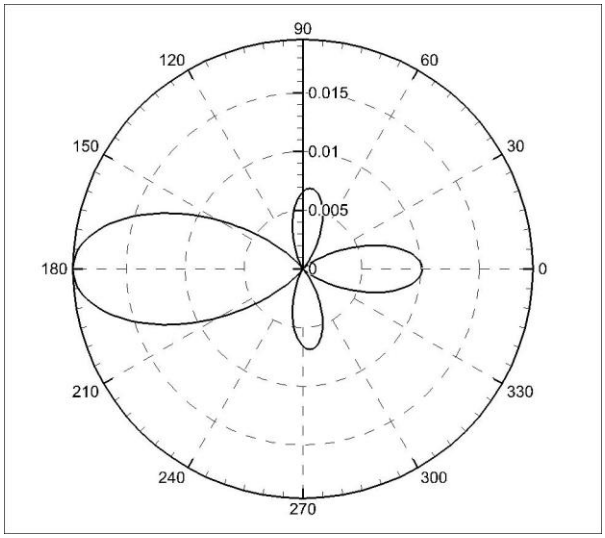

Fig. 2-4 The scattered wave energy plotted in polar coordinate for 100m waves scattered by a circlar ice floe. The ice thickness is 1m. The floe diameter is 50m, and its Young's modulus is 6GPa. (Reproduced by Sukun Cheng following Meylan.)

Based on the above discussion, the operational ocean wave model needs to measure geometrical properties of sea ice, such as size distribution, thickness distribution, and shape properties for the input of ice related terms in an ocean wave model. Field and remote sensing technology are now capable of providing data for such quantities [68]. Once determined as the initial condition, floe breaking models integrated with wave propagation models can then predict the future evolution of the ice cover together with the wave climate. That is, if further freezing and other ice floe growth mechanisms are negligible. There currently is no research done in modeling or measuring floe size growth due to either thermal or mechanical processes.

All of the floe breaking models are so far based on elastic plate theory, for applications that adopt the viscoelastic model, we also need to determine viscosity and

shear modulus from the geometrical properties, and then construct a breaking model for this type of material.

2.7 Laboratory experiment

All theoretical studies need to be validated with data, hence experiments, either laboratory or field, are needed to complete any theoretical development before application. Laboratories provide a controlled environment under which mechanistic studies may be performed. There are a number of such studies that have been conducted around the world. Here we discuss some examples related to wave-ice interactions. These studies were carried out in refrigerated or outdoor facilities where real ice was created, or with artificial floating materials in wave tanks under room temperatures.

Wave induced drift of an isolated floe was conducted by Harms [69] using polyethylene in a long wave tank. The motivations were to estimate the time-of-arrival of isolated objects in the ocean such as abandoned barges and ice floes; the dispersal of floating objects of different sizes; and impact energy of such objects with fixed or floating structures in the ocean. Similar experiments were conducted by Huang et al. [70, 71] to determine the mean drift velocity in relation to the wavelength and amplitude. These experiments showed that floe size to wavelength and its aspect ratio, and the wave steepness affected the drift velocity, which exceeded the Stokes drift. Using PVC materials, Montiel et al. [72, 73] conducted a wave scattering experiment using a circular disk floating in a wide wave tank. The disk was constraint from drifting via a fixed vertical rod that penetrated the center of the disk. They compared the results with the thin elastic plate theory to find reasonable agreement under small amplitude waves.

Single floe drifting over water surface does not affect the wave field except in the vicinity of the floe. In geophysical scale, interactions between ice covers and a wave field result from a large collection of individual ice floes. Sakai and Hanai [50] used polyethylene plate the width of a wave tank to study the effective rigidity behavior of a fragmented ice cover. They cut the plate into successively smaller sizes, in each case they kept the total solid coverage and solid concentration constant. They then measured the wave speed in each of these cases to determine that the effective rigidity of the cover reduced rapidly as the floe size reduced. Dai et al. [6] used plastic materials cut into small squares floating in a monochromatic wave field. The floes were free to move until they come to a comb-shape rack that blocked the floe but let the wave propagate with little impedance. In this study they addressed the issue of ice cover thickening due to wave rafting, a phenomenon that was believed to help early ice cover stabilization against diurnal heating. The wave pressure balanced the resistance of the ice pile quickly form an equilibrium thickness. The dimensionless thickness (h/L) was found to be proportional to the square of the dimensionless wave amplitude (A/L) and the square of the dimensionless floe size (l_i/L). For a typical storm condition in the Sea of Okhotsk [74], the amount of thickening agreed with this experiment.

Cold room and outdoor facilities were both used for wave-ice studies. Newyear and Martin [51, 52] conducted such experiments using a cold room facility to determine the viscosity of grease ice. An outdoor pond at the US Army Cold Regions Research and Engineering Laboratory (CRREL) provided early observations of wave-ice interactions. In January-February clear and cold nights supplied natural cooling to rapidly form an ice cover from the open water condition. Overnight tests were made in several studies to

determine the feasibility of forming pancake ice found in nature as described by Lange et al. [48]. The wave paddle in this facility was much smaller than the width of the pond. Hence a complex two-dimensional wave from multiple wall reflections was produced. To better control the wave field, indoor experiments using a long wave flume was later conducted both at CRREL and at the Hamburgische Schiffbau-Versuchsanstalt GmbH (HSVA) in Germany. These wave flumes were in cold rooms where air temperature could be controlled. Ice covers were formed from open water conditions while maintaining a constant wave input. This type of experiments were made to determine the limiting pancake ice size [75], ice production rate under wave conditions [76], and the attenuation and wavelength change under different types of ice covers [77, 78].

2.8 Field measurement

Field experiments are essential to developing theories of wave-ice interactions. They provide direct observations that guide and then validate theories, which inevitably are based on assumptions. Early observations of waves in sea ice were made by seafarers and explorers. The most famous of such observations is recorded in Endurance: Shackleton's Incredible Voyage [79]. Organized scientific observations were made sporadically from the late 1970s, using ships, helicopters, and ice floes as platforms. Some were visual with still or video cameras, others were made with instruments installed in drifting buoys or packages that must be manually deployed, maintained, and retrieved from the ice covers. Because of the harsh conditions in the field, conducting such experiments is difficult. In recent years remote sensing from satellite has gradually increased its capability to get high resolution field data as well. Here we describe a number of field experiments that show some examples of data obtained concerning wave-ice interactions.

Squire and Moore [80] performed a wave attenuation study over a field of diffused broken ice floes in the Bering Sea. They used an accelerometer package sitting on top of ice floes to detect the heave motion at seven locations along a track perpendicular to the ice edge. Due to logistic reasons they had to make seven sequential measurements over an eight hour span. A wave rider buoy at the ice edge however was used during this period to ensure that the incoming wave energy was stationary. With this data set they verified that the ice fields attenuated wave approximately exponentially, with the attenuation coefficient increase with increasing wave frequency.

Wadhams et al. [81, 82] summarized a large set of field studies conducted between 1978 and 1983 in the east Greenland Sea, the Bering Sea, and the Fram Strait region. In all cases the field was a diffused broken ice cover with increasing ice concentration and floe size inward from the ice edge. The same accelerometer package as in Squire and Moore [80] was used in the earlier studies, but in later ones they were able to use directional buoys that could measure the full directional wave spectra. Using these data, they found two very important phenomena. One was that exponential attenuation of wave energy in an ice cover appeared to be true in call cases, but the attenuation rate was not monotonically increasing with increasing frequency. There was a peak attenuation, beyond which increasing frequency resulted in decreasing attenuation – what they called the "roll-over" effect. The other was that significant wave scattering was found that resulted in isotropic wave spectra a short distance into the ice cover. To this date, their work represents the most comprehensive field data set concerning wave attenuation and scattering in a broken ice field. Similar studies were also done by others. Frankenstein et al. [83] conducted a study in the Barents Sea. They used a six-degree-of-freedom

tiltmeter/accelerometer package deployed over ice floes embedded in a dense brash ice matrix. In addition to confirming similar wave attenuation as previously found, they also found that the total kinetic energy of a floe was nearly equally partitioned among each degree of freedom. Since for an isolated floe, the response in a planar wave field should be dominated by the heave motion, this observation suggested that floe-floe interactions contributed to the dynamics of the floes, which agreed with the visual observations. A long distance and long duration experiment was recently conducted by Kohout et al. [8]. In this study they used five buoys deployed on ice floes in the Southern Ocean. These buoys were then allowed to drift with these floes for several weeks. These buoys were equipped with three accelerometers coupled with a tri-axis Inertial Measurement Unit (IMU) and located using GPS. The vertical motion of the buoy was obtained from these sensors and then transmitted to the recording station via satellite. They then used the vertical displacement to analyze the wave attenuation characteristics. It was found that mild waves attenuated approximately exponentially with distance, as many theories suggested, but intense waves under storm conditions appeared to attenuate linearly with distance, indicating much longer energy penetration into the ice cover.

Focusing on small scale mechanisms, Mckenna and Crocker [84] conducted a study in the Labrador Sea using similar tiltmeter/accelerometer package. Since floe collisions represent an energy sink to the wave field, they were interested in the frequency of floe-floe collisions in a wave field. The ice cover was a collection of fragmented floes. Contrary to expectation, they did not find any conclusive evidence that increasing collision activities were associated with increasing wave amplitude. Similar study was also done by Rottier [85] in Barents Sea and the Fram Strait. He conducted direct

measurement of floe-floe collision rate in a wave field using a buoy equipped with a tri-axial accelerometer package and two perpendicular tiltmeters. This buoy was deployed many times inside the ice cover near the ice edge. The vertical acceleration was used to obtain the wave spectrum and tiltmeters gave the wave direction. The horizontal accelerations indicated the floe-floe collisions. Using this data set, the frequency of collisions was compared with the wave energy and the floe concentration. It was found that the collision frequency was closely correlated with the ratio of wave amplitude and the spacing between neighboring floes.

Land-based field observations are comparatively easier to make. In a recent study Campbell et al. [86] reported a stereo imaging method using video cameras fixed on the coast of Lake Mendota, Wisconsin. They were able to map out the entire wave field over various types of ice covers with high spatial and temporal resolution. They found that frazil/pancake ice covers affected waves differently from the brash ice cover. The former damped out high frequency waves and the latter appeared to transfer low frequency energy into high frequency bands.

Remote sensing is another important source of field data for sea ice. With satellite altimetry and imagery and synthetic aperture radar data, one can obtain the sea ice information, such as, ice type [87], ice thickness [88], ice concentration [89], ice kinematics [90], and wave data [44].

2.9 Numerical simulation

Because laboratory experiments and field measurements are time consuming, expensive, and often limited by the available facility size and other physical constraints, numerical simulations become an alternative to study the detailed mechanisms on wave

and ice interactions. The discrete element method is a popular method for this purpose [91]. The simplest approach is to model the ice floes as disk elements floating on the water surface. As the wave propagates through the ice cover, each of these floes experience drag and added mass effect from the water. They also collide and consume energy through their interactions. The ice floe moves like a rigid body, but the interactions between floes are viscoelastic. So the wave damping effect can be measured from the collisions between floes [46]. Recently, this method is extended to simulate interaction among wave, ice and engineering structures [92]. All of the existing modeling studies have not included the feedback effect from the ice motion to the hydrodynamics part. For smaller ice floes over a large area, it is hard to use such method, because the number of ice floes is huge. Therefore, representing such discrete aggregates as continua becomes useful. Recently, Zhao and Shen [93] apply finite difference method and the level set method to simulate waves propagating under a floating viscoelastic material over water. This work is expected to simulate the two layers model for grease or pancake ice. In this simulation, the equations of motion for the three fluid regions: air, ice, and water, are integrated by the finite difference method, and the interfaces are captured using the level set method. Similar methods can also be employed to simulate elastic ice covered ocean. To numerically simulate wave ice interactions is a still a very new area. There is a lot more work required to mature this technique. There is high potential for this method to provide more detailed information on the validity of analytical models for wave attenuation and wave scattering.

CHAPTER 3 THREE LAYER VISCOELASTIC MODEL

A three-layer model is presented to simulate free surface gravity wave propagation in an ice covered sea. Damping from a viscoelastic ice cover and turbulence in the boundary layer of the water body are considered. This model is shown to converge to three previous models: viscoelastic ice over inviscid water; thin elastic plate over viscous water; and viscous ice over viscous water. The non-monotonic attenuation behavior with respect to wave period shown previously in the thin elastic plate over viscous water appears in the present model as well, suggesting such phenomenon has a source from the water viscosity.

3.1 Introduction

Currently, WW3 ocean wave model provides two separate choices: the eddy viscosity model and the viscoelastic model. They simulate two different mechanisms of wave attenuation in the MIZ, each reflects some reality. De Carolis and Desiderio [22] provided another model which included viscous damping in the ice cover as well as that in the water body. The ice cover was assumed to be pure viscous hence this model may not be applicable to all ice types encountered in the MIZ.

The aim of this chapter is to generalize the three existing wave-in-ice models mentioned above, i.e. the viscoelastic, eddy-viscosity, and viscous-ice-over-viscous-water, in order to include both energy dissipation effects from the water body and the ice cover. The ice cover may have viscous and elastic characteristics. Different from previous models, the present model divides the ice covered ocean into three-layers: viscoelastic ice; upper ocean part with an eddy viscosity; and lower ocean part as an inviscid fluid. This

model recognizes the main phenomena from both the ice region and the water region. In the ice region, the elasticity comes from the intact ice floes or ice sheets and viscosity comes from a variety of mechanisms, e.g. bending and fracturing of ice sheets, deformation of the ice slurry, and collision between ice floes. In the water region, it is known that under an ice cover there is in general a thin surface boundary layer and a substantial outer boundary layer. The eddy viscosity inside the surface boundary layer increases from zero at the water-ice interface to a finite value which equals to the nearly constant eddy viscosity in the outer boundary layer [94]. In our formulation we will ignore the thin surface boundary layer and consider the eddy viscosity is constant within the entire boundary layer. The rest of the water body is assumed inviscid. In addition to its application in wave modeling in the Arctic, this study also addresses a fundamental problem that involves complicated fluid/solid interactions.

3.2 Formulation

3.2.1 Governing equations

We consider a two-dimensional three-layer system in which a homogeneous viscoelastic ice layer of finite thickness h overlays the water of finite depth H with a turbulent boundary layer of thickness b under the ice cover as shown in Fig. 3-1. Gravity wave propagating through this material with a small amplitude linear wave assumption is considered. For the ice cover, we use a Voigt viscoelastic continuum model shown below,

$$\tau_{mn} = -p\delta_{mn} + 2GS_{mn} + 2\rho_{ice}\nu_{ice}\dot{S}_{mn}. \tag{3.1}$$

where ρ_{ice} is the density of the ice layer; σ_{mn}, S_{mn} and $\dot{S}_{mn}$ represent the stress tensor, the strain tensor and the strain rate tensor, respectively; m and n represent x or z; G

and ν_{ice} are the shear modulus and the kinematic viscosity of the ice layer, respectively; p is the pressure and δ_{mn} the Kronecker delta. The linearized equations of motion for the three-layers are

$$\frac{\partial \mathbf{U}_n}{\partial t} = -\frac{1}{\rho_n}\nabla p_n + \nu_n \nabla^2 \mathbf{U}_n + \mathbf{g}, \tag{3.2}$$

where n =1, 2, 3, $\mathbf{U}_n$ is the velocity vector, p_n it the pressure, $\mathbf{g}$ the gravitational acceleration, and ν_n is the effective viscosity. In the ice layer,

$$\nu_1 = \nu_{ice} + iG/\rho_{ice}\omega, \ \rho_1 = \rho_{ice} \tag{3.3}$$

where σ is the angular wave frequency. In the upper part of the water, i.e. the turbulent boundary layer under the ice cover,

$$\nu_2 = \nu_t, \ \rho_2 = \rho_{water}, \tag{3.4}$$

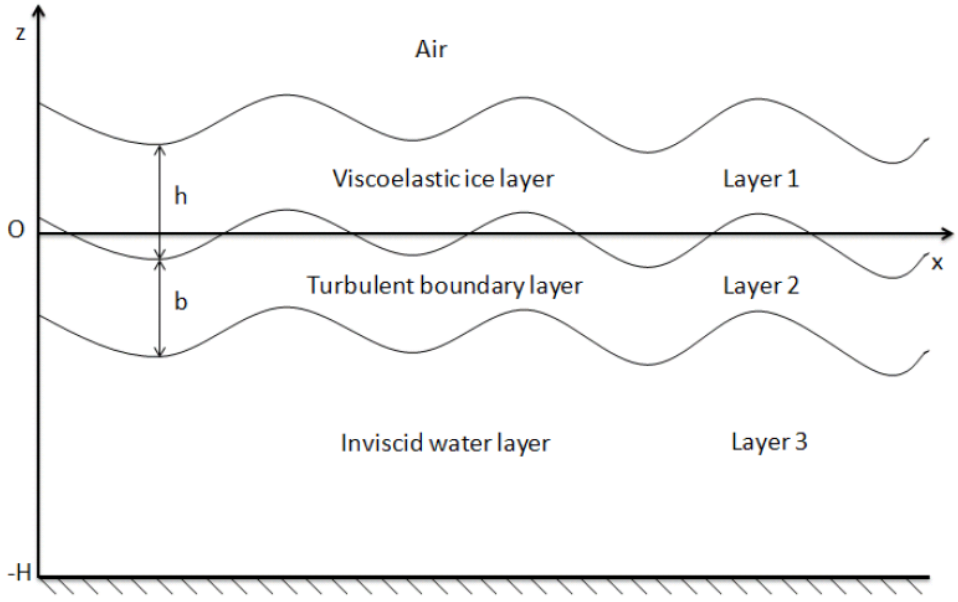

Fig. 3-1 The sketch of the three-layer viscoelastic model.

where ν_t is the kinematic eddy viscosity, and ρ_{water} is the density of water. In the lower part of the water,

$$\nu_3 = 0,\ \rho_3 = \rho_{water}. \tag{3.5}$$

Using the decomposition with potential function ϕ_n, and stream function ψ_n for the velocity [95],

$$\mathbf{U}_n = -\nabla\phi_n + \nabla\times(0,\psi_n,0), \tag{3.6}$$

we obtain

$$\nabla^2\phi_n = 0, \tag{3.7}$$

$$\frac{\partial\psi_n}{\partial t} = \nu_n\nabla^2\psi_n, \tag{3.8}$$

$$\frac{\partial\phi_n}{\partial t} = \frac{p_n}{\rho_n} + \Phi, \tag{3.9}$$

Here, $\Phi = gz$ is the gravitational potential. In the lower part of water, the stream function $\psi_3 \equiv 0$. In the two-dimensional system, the velocity has following expressions,

$$\mathbf{U}_n = (u_n,0,w_n). \tag{3.10}$$

$$u_n = -\frac{\partial\phi_n}{\partial x} - \frac{\partial\psi_n}{\partial z},\ w_n = -\frac{\partial\phi_n}{\partial z} + \frac{\partial\psi_n}{\partial x}. \tag{3.11}$$

3.2.2 Boundary conditions

At the air-ice free surface, the dynamic boundary conditions are as the following,

$$\tau_{xz}^1 = \tau_{zz}^1 = 0, z = h. \tag{3.12}$$

The linearized kinematic boundary condition is

$$w_1 = \frac{\partial\eta_1}{\partial t}, z = h. \tag{3.13}$$

At the ice-water interface, the dynamic boundary conditions are as the following,

$$\tau_{xz}^{1} = \tau_{xz}^{2}, \tau_{zz}^{1} = \tau_{zz}^{2}, z = 0. \tag{3.14}$$

The kinematic boundary condition is

$$w_1 = w_2 = \frac{\partial \eta_2}{\partial t},\ u_1 = u_2, z = 0. \tag{3.15}$$

At the water-water interface, the dynamic boundary conditions are as the following,

$$\tau_{xz}^{2} = \tau_{xz}^{3}, \tau_{zz}^{2} = \tau_{zz}^{3}, z = -b. \tag{3.16}$$

The kinematic boundary condition is

$$w_2 = w_3 = \frac{\partial \eta_3}{\partial t},\ z = 0. \tag{3.17}$$

For the rigid bottom boundary, the vertical velocity vanishes,

$$w_3 = 0, z = -H. \tag{3.18}$$

In above, the stresses in terms of pressure and velocity are

$$\tau_{xz}^{n} = \rho_n \nu_n \left(\frac{\partial u_n}{\partial z} + \frac{\partial w_n}{\partial x} \right), \tag{3.19}$$

$$\tau_{zz}^{n} = -p_n + 2\rho_n \nu_n \frac{\partial w_n}{\partial z}. \tag{3.20}$$

3.2.3 Dispersion relation

Decompose the wave elevations at the interfaces into simple harmonics,

$$\eta_n = a_n e^{i(kx-\omega t)},\ n = 1, 2, 3. \tag{3.21}$$

The general solutions for (3.7) and (3.8) can be taken as

$$\phi_n = \left(A_n \cosh kz + B_n \sinh kz\right) e^{i(kx-\omega t)}, \tag{3.22}$$

$$\psi_n = \left(C_n \cosh \alpha z + D_n \sinh \alpha z\right) e^{i(kx-\omega t)}, \tag{3.23}$$

Here, $\alpha^2 = k^2 - i\omega/\nu_n$, n=1, 2. For the lower part of water, with (3.18) and (3.5) we obtain

$$\phi_3 = E_3 \cosh k(z+H) e^{i(kx-\omega t)}. \tag{3.24}$$

Substitute (3.9) into the normal stress (3.20) to eliminate pressure, and with (3.13), (3.15) and (3.17) we eliminate the elevations by taking time derivative of the normal stress boundary conditions. By noting that

$$\frac{\partial^2 \phi_3}{\partial t^2} = \frac{i\omega}{k \tanh k(z+H)} \frac{\partial w_2}{\partial t}, z = -b, \tag{3.25}$$

we obtain eight equations for ϕ_n, and ψ_n (n=1,2) as shown in Appendix A. Using the general solutions (3.22) and (3.23) in the obtained eight equations, we get a homogeneous 8×8 linear system for coefficients A_n, B_n, C_n, and D_n (n=1,2). The dispersion relation for ω and k is obtained by imposing that the determinant of the coefficients matrix vanishes. Solution of this dispersion relation for a given wave frequency ω is in general a complex number, $k = \kappa + iq$, where the real part is the propagating wave number and the imaginary part is the attenuation coefficient.

3.3 Results

Convergence to the viscoelastic model - We now discuss the effect of viscous boundary layer on wave number and wave attenuation. Figure 3-2 shows the results of the current model for boundary layer thickness, b, varying from 10^{-6}m to 10m, and the eddy viscosity varying from 10^{-6}m^2/s to 10^{-2}m^2/s. The wave number κ is found to be insensitive to the eddy viscosity and the boundary layer thickness for the range of parameters tested. The attenuation coefficient, q, increases significantly with boundary

layer thickness and the eddy viscosity. It is interesting to note that for long wave periods, the gradient of wave decay is milder than the intermediate wave periods. There is also a slight "bump" in the attenuation trend when T is between 5sec and 10sec. The location and the size of this bump depend on the shear modulus as will be discussed later. The current results converge to those from the viscoelastic ice over inviscid water when the eddy viscosity and the boundary layer thickness decrease, as expected.

Convergence to the eddy viscosity model - By letting the boundary layer thickness approach the water depth, and the viscosity of the ice cover vanish, the current model conceptually approaches the eddy viscosity model of Liu and Mollo-Christensen, where a uniform viscous water body under a thin elastic plate is assumed. Figure 3-3 gives the results of cases where the ice rigidity is fixed at 10^9Pa with no viscosity, and the eddy viscosity is fixed at ν_t=0.001m^2/s. The boundary layer thickness varies from 0.01m to 100m, with water depth at 100m. The wave number calculated from the present model is again insensitive to b. The attenuation, which is sensitive to the boundary layer, indeed converges to that from the eddy-viscosity model when b approaches the total water depth. This approach is quite rapid. For b>1m, which is in fact much smaller than most of the boundary layer thickness in the field, the results become insensitive to b. Because of the exponential decay of wave induced velocity field, the velocity gradient and thus the viscous energy loss in the water body drops very quickly.

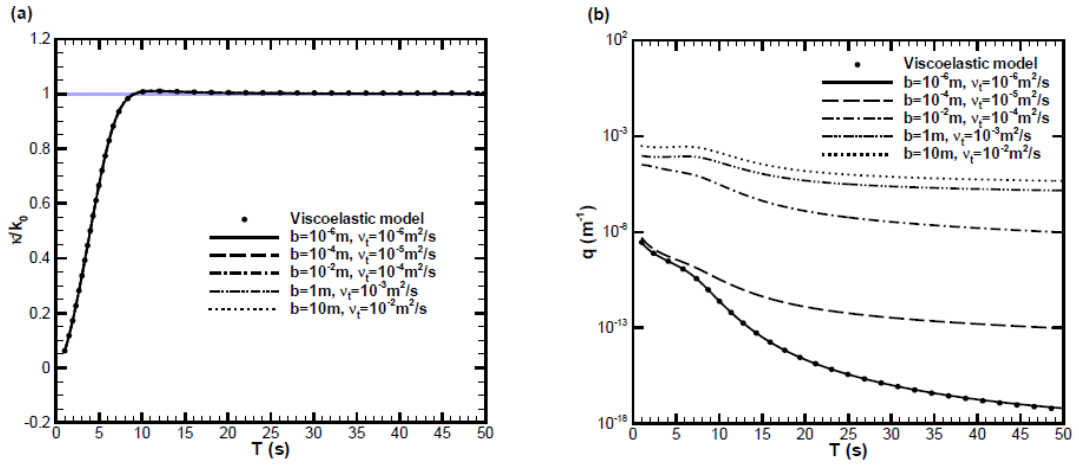

Fig. 3-2 Normalized wave numbers, κ / k_0, and wave attenuation, q, plotted against wave period T for $h = 0.5$m, $H = 100$m, $G = 10^9$Pa, $\nu_{ice} = 0.01$m^2/s, $\rho_{ice} = 917$kg/m^3, and $\rho_{water} = 1000$kg/m^3. Here, k_0 is the wave number for open water case.

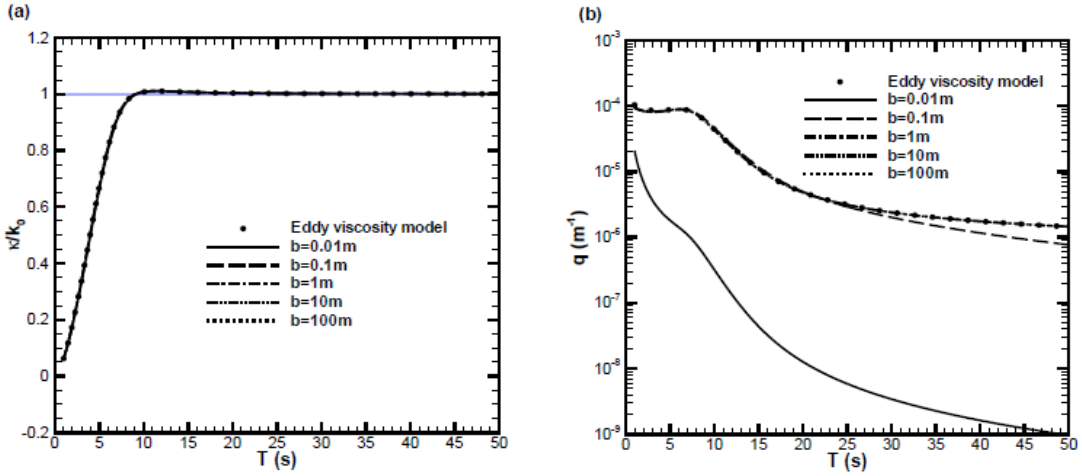

Fig. 3-3 Normalized wave numbers, κ / k_0, and wave attenuation, q, plotted against wave period T for $h = 0.5$m, $H = 100$m, $G = 10^9$Pa, $\nu_{ice} = 0$m^2/s, $\nu_t = 0.001$m^2/s, $\rho_{ice} = 917$kg/m^3, and $\rho_{water} = 1000$kg/m^3. Here, k_0 is the wave number for open water case.

Convergence to the viscous-ice-over-viscous-water model - Now, we show the convergence from the three-layer model to the two layer viscous model. There are two main differences between the three-layer model and the two layer viscous model: the

non-slip bottom boundary condition for velocities in the viscous-ice-over-viscous-water model; the shear modulus effect in the ice layer of the three-layer model. To avoid the singularity at the bottom, when boundary layer thickness exactly equals to water depth, we employ non-slip boundary conditions at the sea floor. With this addition, we compare the results with the viscous-ice-over-viscous-water model and then study the effect of shear modulus in the three-layer model. In figure 3-4 we present the results when ice thickness is 0.5m, boundary layer thickness equals to that of the water depth 100m and the viscosities of the ice layer and the eddy viscosity are ν_{ice}=0.01m^2/s, ν_t=0.001m^2/s. Over the entire range of wave period, the present model converges to that of the viscous-ice-over-viscouswater case when the shear modulus approaches 0. As the shear modulus increases, an interesting phenomenon occurs. The bump mentioned earlier becomes prominent. In particular for the case G =10^{6}Pa. This bump is seen both in the wavenumber curve and the wave attenuation curve, at approximately the same wave period. For different G values, the location of the bump differs. This phenomenon, named "roll-over" has been observed both in theory and in the field [44]. The wave attenuation is not a monotonic function of the wave period, but has a maximum at some T. So far, among all the existing theories that consider some kind of damping mechanism, only the eddy-viscosity theory that has ever demonstrated roll-over. The present model, which includes the eddy viscosity, unsurprisingly is also able to show this effect.

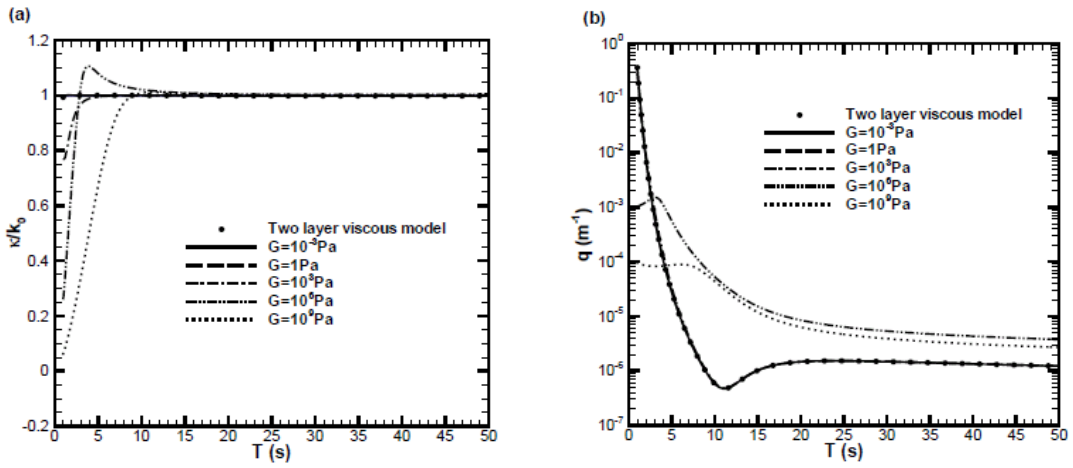

Fig. 3-4 Normalized wave numbers, κ / k_0, and wave attenuation, q, plotted against wave period T for h=0.5m, b=100m, H=100m, ν_{ice}=0m^2/s, ν_t=0.001m^2/s, ρ_{ice} = 917kg/m^3, and ρ_{water}=1000kg/m^3. Here, k_0 is the wave number for open water case.

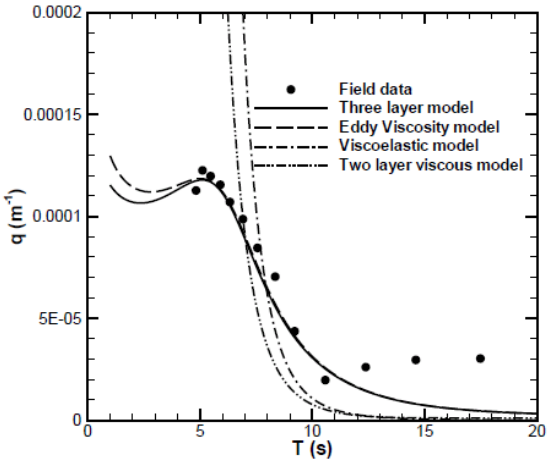

Fig. 3-5 Wave attenuation, q, plotted against wave period T : for all curves h=0.5m, H=100m, ν_t=0.00045m^2/s, ρ_{ice}=917kg/m^3, and ρ_{water}=1000kg/m^3. For the two layer viscous model, ν_{ice}=1m^2/s. For the viscoelastic model, ν_{ice}=1m^2/s, and G=10^{4}Pa. For the eddy viscosity model, Young's modulus E = 8.4×10^{8}Pa. For the three-layer model, ν_{ice} =0.01m^2/s, G=2×10^{8}Pa, and b=10m.

Origin of the "roll-over" on wave attenuation - Next we test how the present model performs when compared directly with field data. Figure 3-5 shows a comparison with wave attenuation obtained in the Bering Sea in 1979 [80, 82]. The ice layer thickness was 0.5m consisting of a variety of floe sizes and concentration. The wave spectra were measured at 8 locations over 65.1km distance. The data provided attenuation for a range of wave periods. We use an optimization procedure to determine the best-fit parameters of each model. The field water depth was not reported. We have found that beyond 100m water depth does not affect the results, hence it is fixed at 100m for the comparison. As can be seen, only the eddy viscosity and the three-layer model can reproduce the observed roll-over, which strongly suggests that water body viscosity is the source of this phenomenon. The three-layer model is slightly better than the eddy viscosity model for the data fitting. The disagreement at long wave periods cannot be explained by the current theories.

3.4 Conclusions

We provided a theoretical solution for wave-in-ice models. This theory is based on mechanisms from both the ice cover and the water body. In the ice cover there are processes which contribute to wave speed change and wave attenuation. These include viscous interaction of small ice crystals, ice floe collisions, ice sheet bending and fracturing. In the water body there is turbulence generated in the boundary layer which is parameterized by an eddy viscosity. We model this situation by dividing the ice covered ocean into three-layers: the ice, the boundary layer, and the rest of the water body. In which, the ice layer is viscoelastic, the boundary layer is viscous, and the rest of the water body is inviscid. We show that this general model reproduces results of all existing

models that considered these mechanisms separately, and under more simplified conditions. This general model alleviates the need of wave modelers to choose between eddy viscosity and viscoelastic ice models for their simulations. In fact both are present in nature. With future experiments, both in the field and in laboratories, we expect direct measurement of eddy viscosity and boundary layer thickness will be systematically obtained in ice covered seas. The viscoelastic parameters for ice covers need to be determined by field and experimental data and an inverse method. Though the task of determining the parameter values is challenging, we at least have a theoretical framework to guide experiments and integrate measured data into a coherent model. Finally, for application purpose, it is necessary to have an efficient way to take any input set: the water depth, ice thickness, ice properties, boundary layer thickness and its eddy viscosity, to determine the resulting wave number and attenuation coefficient. The analytical solution given in Appendix A is in the form of a matrix. Its determinant cannot be simplified into a short closed-form expression. An efficient numerical procedure was used in all the results shown here.

CHAPTER 4 APPROXIMATE METHOD

An approximate solution for wave transmission and reflection between open water and a viscoelastic ice cover was developed earlier, in which both the water and the ice cover were treated as a continuum. The interface conditions included matching velocity and stresses between the two continua. The analysis provided a first step towards modeling the wave-in-ice climate on a geophysical scale, where properties of the ice cover change with time and location. In this chapter, we derive the wave transmission and reflection from one viscoelastic material to another. Only two modes of the dispersion relation are considered and the horizontal boundary conditions are approximated by matching the mean values.

4.1 Introduction

In this chapter, we extend the previous work to investigate wave propagation from one viscoelastic cover into another. The motivation for this study is evident: to mathematically model the wave propagation over a large expanse with varying physical conditions, a numerical method is required. All numerical methods discretize the computational domain into finite size "cells". The ice cover is connected at the cell boundary, and the change in properties is abrupt. Within each cell, average properties of variables are considered. A continuously varying ice cover is thus discretized into cells of different thickness and material properties. Wave damping mechanisms contribute to the sink term within each cell. At the boundary between neighboring cells wave flux contributes to the energy transport. Both damping and flux terms are required for any numerical wave models. Transmission and reflection at cell boundaries are in fact part of

the cumulative results of this process that take place at the floe scale, where all discontinuities contribute to this process. The types of floe scale discontinuities and their scattering properties are shown in Bennetts and Squire [53, 54]. Part of the cumulative results is accounted for in the wave attenuation due to the average properties of the ice within the cell. The part due to the gradient of the ice properties within the cell is accounted for at the cell boundary. These two processes are shown schematically in Fig. 4-1, where the sink term has been studied as part of the dispersion relation in Wang and Shen [23]. The flux term is the focus of the present study.

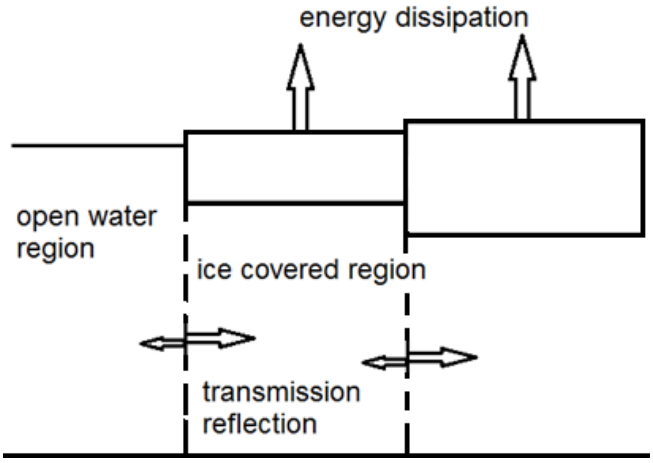

Fig. 4-1 Schematic of a discretized field of wave propagation into a continuous heterogeneous ice cover.

The study in this chapter also helps to expand floe scale investigations. Wave scattering theory developed by Wadhams [96, 97] and later extensively studied by Squire and colleagues [11, 53, 54] considered ice floes dispersed in open water. The present work may expand these theories to situations of ice floes imbedded in a grease or brash ice field. These two different types of ice covers are shown in Fig.4-2.

Fig. 4-2 (Left) A photo of a broken up ice cover interspersed in open water. The narrow range of size distribution suggests a wave induced breakage. (Credit: Vernon Squire). (Right) A photo of ice floes interspersed with pancake ice. (Credit: Don Perovich).

To determine the flux between two adjacent ice covers with different viscoelastic properties, in this study we will use the same approximate approach as given in Wang and Shen [58]. We will consider two leading modes only to determine the partition of energy of each mode for a linear monochromatic gravity wave. Our treatment of the horizontal boundary conditions will also follow the same approximation method. A linear wave regime is assumed in this study.

4.2 Theoretical formulation

4.2.1 Definition of the domain

The problem to be analyzed is two dimensional. The two ice covers are assumed to be fully submerged. This assumption is based on the results from Williams and Porter [98], where it is shown that the draft of a floating ice cover affects the wave transmission and reflection. The small amount of ice cover exposed in air is ignored in this study. The

coordinate system used in this study is shown in Fig.4-3. The x direction is aligned with the incoming wave direction, and the z direction is opposite to gravity. The origin is set at the top of the ice cover right between the two ice regions. As shown in Fig.4-3, there are four regions: ice region 1 and 3; water region 2 and 4. A monochromatic wave propagates from left to right. The ice thickness for region 1 and 3 are h_1 and h_3, respectively. The total depth of the domain is H.

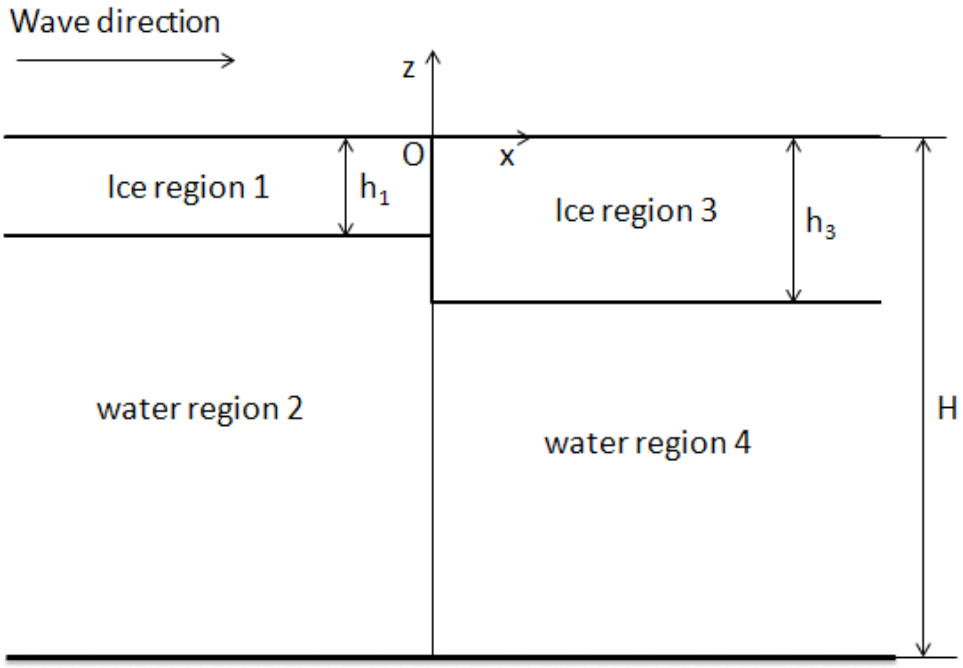

Fig. 4-3 Schematic of the coordinate frame of the problem.

4.2.2 Governing equations

For the ice cover, we use a Voigt viscoelastic continuum model shown below [23, 58]:

$$\tau_{mn} = -p\delta_{mn} + 2GS_{mn} + 2\rho_{ice}\nu\dot{S}_{mn}, \tag{4.1}$$

where ρ_{ice} is the density of the ice layer; σ_{mn}, S_{mn} and $\dot{S}_{mn}$ represent the stress tensor, the strain tensor and the strain rate tensor, respectively; m and n represent x or z; G and ν are the effective shear modulus and the effective kinematic viscosity of the ice layer, respectively; p is the pressure and δ_{mn} the Kronecker delta. The equation of motion is

$$\frac{\partial \mathbf{U}_i}{\partial t} = -\frac{1}{\rho_{ice}} \nabla p_i + \nu_{ei} \nabla^2 \mathbf{U}_i + \mathbf{g} \qquad \text{i=1,3} \tag{4.2}$$

where $\mathbf{U}_i$ is the velocity vector, $\mathbf{g}$ the gravitational acceleration, and ν_{ei} the viscoelastic parameter:

$$\nu_{ei} = \nu_i + iG_i / \rho_{ice}\omega \qquad \text{i=1,3} \tag{4.3}$$

In which, ν_i and G_i are the effective parameters in each respective region i, and ω is the angular frequency of the incoming wave. Using the decomposition with potential function φ_i and stream function ψ_i for the velocity [95],

$$\mathbf{U}_i = -\nabla \varphi_i + \nabla \times (0, \psi_i, 0) \qquad \text{i=1,3} \tag{4.4}$$

we obtain

$$\nabla^2 \varphi_i = 0 \tag{4.5}$$

$$\frac{\partial \psi_i}{\partial t} - \nu_{ei} \nabla^2 \psi_i = 0 \tag{4.6}$$

$$\frac{\partial \varphi_i}{\partial t} - \frac{p_i}{\rho_{ice}} - \Phi = 0 \qquad \text{i=1,3} \tag{4.7}$$

Here, $\Phi = gz$ is the gravitational potential.

For water regions 2 and 4, we assume an inviscid fluid. The governing equations are

$$\frac{\partial \mathbf{U}_i}{\partial t} = -\frac{1}{\rho_{water}} \nabla p_i + \mathbf{g} \tag{4.8}$$

$$\nabla^2 \varphi_i = 0 \tag{4.9}$$

$$\frac{\partial \varphi_i}{\partial t} - \frac{p_i}{\rho_{water}} - \Phi = 0 \qquad \text{i=2,4} \tag{4.10}$$

The water velocity is related to the velocity potential only:

$$\mathbf{U}_i = -\nabla \varphi_i \qquad \text{i=2,4} \tag{4.11}$$

In terms of the Fourier modes, the solution for a sinusoidal wave with two modes can be written as [58]

$$\varphi_i(x,z,t) = \sum_{n=1}^{2} (A_i(n)\cosh k_i(n)z + B_i(n)\sinh k_i(n)z) e^{ik_i(n)x} e^{-i\omega t} \; ; \tag{4.12}$$

$$\psi_i(x,z,t) = \sum_{n=1}^{2} (C_i(n)\cosh \alpha_i(n)z + D_i(n)\sinh \alpha_i(n)z) e^{ik_i(n)x} e^{-i\omega t} \; ; \tag{4.13}$$

for the ice region $i = 1,3$ and $-h_i \le z \le 0$, and

$$\varphi_i(x,z,t) = \sum_{n=1}^{2} E_i(n)\cosh k_i(n)(z+H) e^{ik_i(n)x} e^{-i\omega t} \tag{4.14}$$

for the water region $i = 2,4$ and $-H \le z \le -h_i$. The coefficients $A_i(n)$, $B_i(n)$, $C_i(n)$, $D_i(n)$, and $E_i(n)$ are complex constants. As shown in Appendix C the solution of these constants can be obtained by using the vertical boundary conditions described in subsection 6.2.3. In the above, $\alpha_i^2(n) = k_i^2(n) - i\omega/\nu_{ei}$ for $i = 1,3$ and $n = 1,2$ from Eq. (6). Here $k_i(n)$ is the wave number for each ice-covered region.

4.2.3 Boundary conditions

We now proceed to determine the horizontal boundary conditions between two different viscoelastic regions. In the horizontal direction between the two ice regions and the two water regions, we need to match the displacements, velocities, and stresses.

(a) Water-Water interface

The boundary condition between water region 2 and 4 includes continuity of the potential and the horizontal velocity

$$\varphi_2(0,z) = \varphi_4(0,z), \quad -H < z < -h_3 \tag{4.20}$$

$$\frac{\partial \varphi_2(0,z)}{\partial x} = \frac{\partial \varphi_4(0,z)}{\partial x}, \; -H < z < -h_3 \tag{4.21}$$

(b) Water-Ice interface

For the time being we assume $h_1 < h_3$, the same analysis may be applied to other cases. Between water region 2 and ice region 3, the kinematic condition is

$$u_2(0,z) = u_3(0,z), \; -h_3 < z < -h_1, \tag{4.22}$$

Likewise, the dynamical boundary condition is

$$\tau_{xx2}(0,z) = \tau_{xx3}(0,z), -h_3 < z < -h_1 \tag{4.23}$$

These two conditions are the same as in Wang and Shen [58] for wave propagating from open water to an ice covered region. Additionally, we also include the continuity condition of shear stress at the interface:

$$\tau_{xz3}(0,z) = 0, \; -h_3 < z < -h_1 \tag{4.24}$$

(c) Ice-Ice interface

Between ice region 1 and ice region 3, we use the continuity conditions of horizontal and vertical velocities, and normal and shear stresses:

$$u_1(0,z) = u_3(0,z), \; -h_1 < z < 0 \tag{4.25}$$

$$w_1(0,z) = w_3(0,z)\,,\ -h_1 < z < 0 \tag{4.26}$$

$$\tau_{xx1}(0,z) = \tau_{xx3}(0,z)\,,\ -h_1 < z < 0 \tag{4.27}$$

$$\tau_{xz1}(0,z) = \tau_{xz3}(0,z)\,,\ -h_1 < z < 0 \tag{4.28}$$

(d) Summary of boundary conditions

The above nine equations, Eqs. (4.20-4.28), will be used to determine the transmission and reflection coefficients for a given wave. If freeboard is modeled instead of the current full submergence assumption, we will also need to include the stress free conditions over the exposed air-ice interface at $x = 0$.

$$\tau_{xx}(0,z) = \tau_{xz}(0,z) = 0\,,\ 0 < z < h_{\text{freeboard}} \tag{4.29}$$

These conditions are ignored at present.

In a previous study of wave propagation from one ice cover to another, Barrett and Squire [26] represented both ice covers as thin elastic plates each with its own properties. Their boundary conditions between the two ice covers are the continuity of the vertical displacement, slope, bending moment and shear force. The integral of normal stress distribution is the bending moment and the integral of shear stress distribution is the shear force, hence the boundary conditions used in Barrett and Squire [26] for a thin plate correspond one to one with our continuum boundary conditions.

Equations (4.20-4.28) represent nine sets of infinite equations which cannot be solved exactly. Instead, a least-square method based on the variational method is commonly used to minimize the error function [18, 19]:

$$\varepsilon = \sum_{n=1}^{9} \lambda_n \int_{l_n}^{u_n} \left| F_b^n - F_a^n \right|^2 dz \tag{4.30}$$

where λ_n are the Lagrange multipliers, l_n and u_n are the bounds of the domain where the matching conditions are applied, F_a^n, F_b^n are the corresponding functions that must be matched at two sides, a and b, of each boundary. However, in this study we use a simpler but less accurate approach. We adopt the same approximation as in Wang and Shen [58], in keeping with the fact that we only include two of the multiple modes in the dispersion relation Eq. (2.19). The boundary conditions are approximated by setting the integrals of the required conditions to zero. In this way, we do not minimize the error but require the mean values of both sides of the respective functions be the same. By comparing with the limiting case of pure elastic ice covers, we will get a sense of how well this approximation works.

To summarize, the following equations are the approximated nine horizontal boundary conditions in terms of the potential and stream functions. The derivation of the normal and shear stresses in terms of the potential and stream functions is given in Appendix B.

$$\int_{-H}^{-h_3} \varphi_2(0,z)dz = \int_{-H}^{-h_3} \varphi_4(0,z)dz \tag{4.31}$$

$$\int_{-H}^{-h_3} \frac{\partial \varphi_2(0,z)}{\partial x} dz = \int_{-H}^{-h_3} \frac{\partial \varphi_4(0,z)}{\partial x} dz \tag{4.32}$$

$$\int_{-h_1}^{0} \left(-\frac{\partial \varphi_1(0,z)}{\partial x} - \frac{\partial \psi_1(0,z)}{\partial z} \right) dz = \int_{-h_1}^{0} \left(-\frac{\partial \varphi_3(0,z)}{\partial x} - \frac{\partial \psi_3(0,z)}{\partial z} \right) dz \text{ ; } \tag{4.33}$$

$$\int_{-h_1}^{0} \left(-\frac{\partial \varphi_1(0,z)}{\partial z} + \frac{\partial \psi_1(0,z)}{\partial x} \right) dz = \int_{-h_1}^{0} \left(-\frac{\partial \varphi_3(0,z)}{\partial z} + \frac{\partial \psi_3(0,z)}{\partial x} \right) dz \text{ ; } \tag{4.34}$$

$$\int_{-h_1}^{0}\left[i\omega\rho_{ice}\varphi_1(0,z)+2\rho_{ice}\nu_{e1}\left(-\frac{\partial^2\varphi_1(0,z)}{\partial x^2}-\frac{\partial^2\psi_1(0,z)}{\partial x\partial z}\right)\right]dz$$
$$=\int_{-h_1}^{0}\left[i\omega\rho_{ice}\varphi_3(0,z)+2\rho_{ice}\nu_{e3}\left(-\frac{\partial^2\varphi_3(0,z)}{\partial x^2}-\frac{\partial^2\psi_3(0,z)}{\partial x\partial z}\right)\right]dz \quad ; \quad (4.35)$$

$$\int_{-h_3}^{-h_1}\left(-\frac{\partial\varphi_1(0,z)}{\partial x}\right)dz=\int_{-h_3}^{-h_1}\left(-\frac{\partial\varphi_3(0,z)}{\partial x}-\frac{\partial\psi_3(0,z)}{\partial z}\right)dz \; ; \quad (4.36)$$

$$\int_{-h_3}^{-h_1}i\omega\rho_{water}\varphi_2(0,z)dz=\int_{-h_3}^{-h_1}\left[i\omega\rho_{ice}\varphi_3(0,z)+2\rho_{ice}\nu_{e3}\left(-\frac{\partial^2\varphi_3(0,z)}{\partial x^2}-\frac{\partial^2\psi_3(0,z)}{\partial x\partial z}\right)\right]dz \; ;$$

(4.37)

$$\int_{-h_3}^{-h_1}\rho_{ice}\nu_{e3}\left(-2\frac{\partial^2\varphi_3(0,z)}{\partial x\partial z}-\frac{\partial^2\psi_3(0,z)}{\partial z^2}+\frac{\partial^2\psi_3(0,z)}{\partial x^2}\right)dz=0 \; ; \quad (4.38)$$

$$\int_{-h_1}^{0}\rho_{ice}\nu_{e1}\left(-2\frac{\partial^2\varphi_1(0,z)}{\partial x\partial z}-\frac{\partial^2\psi_1(0,z)}{\partial z^2}+\frac{\partial^2\psi_1(0,z)}{\partial x^2}\right)dz$$
$$=\int_{-h_1}^{0}\rho_{ice}\nu_{e3}\left(-2\frac{\partial^2\varphi_3(0,z)}{\partial x\partial z}-\frac{\partial^2\psi_3(0,z)}{\partial z^2}+\frac{\partial^2\psi_3(0,z)}{\partial x^2}\right)dz \quad ; \quad (4.39)$$

4.3 Solutions

In general, the full solution of the wave propagation through a viscoelastic cover consists of an infinite series of modes, each with a different wave number, all of them roots of the dispersion relation shown in Eq. (4.19). Truncation of this infinite series provides approximate solutions. Following Wang and Shen [58], from solutions of Eq. (4.19) the two wave numbers closest to the open water case are chosen to form the approximate solution. Each of these two modes on the left side of the domain shown in Fig.4-3 is represented by an incoming magnitude I. When entering the right side with a different viscoelastic property, the wave reflects in part represented by $\mathcal{R}$, and transmits

the rest represented by $\mathcal{T}$. Thus the total potential function and the stream function may be written in terms of these two modes as follows, where the individual modes denoted by $n = 1,2$ are given in Eqs. (4.12-4.14).

$$\begin{aligned}\varphi_1(x,z,t) &= \sum_{n=1}^{2} I(n)(A_1(n)\cosh k_1(n)z + B_1(n)\sinh k_1(n)z)e^{ik_1(n)x}e^{-i\omega t} \\ &+ \sum_{n=1}^{2} \mathcal{R}(n)(A_1(n)\cosh k_1(n)z + B_1(n)\sinh k_1(n)z)e^{-ik_1(n)x}e^{-i\omega t}\end{aligned} \quad ; \qquad (4.40)$$

$$\begin{aligned}\psi_1(x,z,t) &= \sum_{n=1}^{2} I(n)(C_1(n)\cosh \alpha_1(n)z + D_1(n)\sinh \alpha_1(n)z)e^{ik_1(n)x}e^{-i\omega t} \\ &+ \sum_{n=1}^{2} \mathcal{R}(n)(C_1(n)\cosh \alpha_1(n)z + D_1(n)\sinh \alpha_1(n)z)e^{-ik_1(n)x}e^{-i\omega t}\end{aligned} \quad ; \qquad (4.41)$$

$$\begin{aligned}\varphi_2(x,z,t) &= \sum_{n=1}^{2} I(n)E_1(n)\cosh k_1(n)(z+H)e^{ik_1(n)x}e^{-i\omega t} \\ &+ \sum_{n=1}^{2} \mathcal{R}(n)E_1(n)\cosh k_1(n)(z+H)e^{-ik_1(n)x}e^{-i\omega t}\end{aligned} \quad ; \qquad (4.42)$$

$$\varphi_3(x,z,t) = \sum_{n=1}^{2} \mathcal{T}(n)(A_3(n)\cosh k_3(n)z + B_3(n)\sinh k_3(n)z)e^{ik_3(n)x}e^{-i\omega t} \; ; \qquad (4.43)$$

$$\psi_3(x,z,t) = \sum_{n=1}^{2} \mathcal{T}(n)(C_3(n)\cosh \alpha_3(n)z + D_3(n)\sinh \alpha_3(n)z)e^{ik_3(n)x}e^{-i\omega t} \; ; \qquad (4.44)$$

$$\varphi_4(x,z,t) = \sum_{n=1}^{2} \mathcal{T}(n)E_3(n)\cosh k_3(n)(z+H)e^{ik_3(n)x}e^{-i\omega t} \; ; \qquad (4.45)$$

In the above,

$$\alpha_i^2(n) = k_i^2(n) - i\omega/\nu_{ei}\,,\ i = 1,3 \text{ and } n = 1,2 \qquad (4.46)$$

The solution matrix for $A_i(n)$, $B_i(n)$, $C_i(n)$, $D_i(n)$ and the equation for solving $E_i(n)$ can be found in Appendix C. After which we can substitute the solutions of $A_i(n)$, $B_i(n)$, $C_i(n)$, $D_i(n)$, $E_i(n)$ into the horizontal boundary conditions to form nine linear

equations for $I(1)$, $\mathcal{R}(1)$, $\mathcal{R}(2)$, $\mathcal{T}(1)$, and $\mathcal{T}(2)$ as in Appendix D. Since a linear wave regime is assumed, we may focus on the incoming wave one mode at a time.The procedure for solving $I(2)$ is identical. Following the above steps, substituting equations (4.40-4.45) into equations (4.31-4.39) gives an under-determined system of nine equations involving only five unknowns $I(1)$, $\mathcal{R}(1)$, $\mathcal{R}(2)$, $\mathcal{T}(1)$, and $\mathcal{T}(2)$. We solve this using singular value decomposition method based on the least-square error method to find the pseudo-inverse.

With the continuity condition of the vertical displacement at the interface, we can derive the transmission and reflection coefficients for the surface profile as in Appendix E.

$$R(1) = \frac{\left|\mathcal{R}(1)\right\| k_1(1)B_1(1) + ik_1(1)C_1(1)\right|}{\left|I(1)\right\| k_1(1)B_1(1) - ik_1(1)C_1(1)\right|}; \tag{4.47}$$

$$R(2) = \frac{\left|\mathcal{R}(2)\right\| k_1(2)B_1(2) + ik_1(2)C_1(2)\right|}{\left|I(1)\right\| k_1(1)B_1(1) - ik_1(1)C_1(1)\right|}; \tag{4.48}$$

$$T(1) = \frac{\left|\mathcal{T}(1)\right\| k_3(1)B_3(1) - ik_3(1)C_3(1)\right|}{\left|I(1)\right\| k_1(1)B_1(1) - ik_1(1)C_1(1)\right|}; \tag{4.49}$$

$$T(2) = \frac{\left|\mathcal{T}(2)\right\| k_3(2)B_3(2) - ik_3(2)C_3(2)\right|}{\left|I(1)\right\| k_1(1)B_1(1) - ik_1(1)C_1(1)\right|}. \tag{4.50}$$

In the next section we will investigate several special cases for which previous results may be used for comparison.

4.4 Wave transmission and reflection – pure elastic covers

In this section we study the behavior of wave propagation involving pure elastic ice covers. The results are compared with existing theories. For all cases shown in this

study, $\rho_{ice} = 917 kg/m^3$, $\rho_{water} = 1000 kg/m^3$, $H = 100m$. Because $R(2)$ is very small for large shear modulus, it is dropped from the discussion in this section. $R(1)$ is denoted as R in the results shown below.

4.4.1 Between open water and elastic ice

We first consider the case of wave propagation from open water to an elastic ice cover. We use the formulation described in Section 4.2, where no limitations of the ice thickness is imposed. The transmission and reflection coefficients are defined in Eqs. (4.47-4.50). Figure 4-4 shows the reflected and transmitted coefficients with respect to the wave period for $\nu = 0 m^2/s$, G_1 =0.001Pa, G_3 =5GPa, h_1 =0.001m, and h_3 =0.5m. Because of the extremely small values of G_1 and h_1, our solution should converge to that of the open water connecting to an elastic cover given in Wang and Shen [58], as indeed shown in Fig. 4-4. In this figure, the more accurate solutions using the Eigenfunction Expansion Matching Method by Kohout et al. [57] are also shown for comparison.

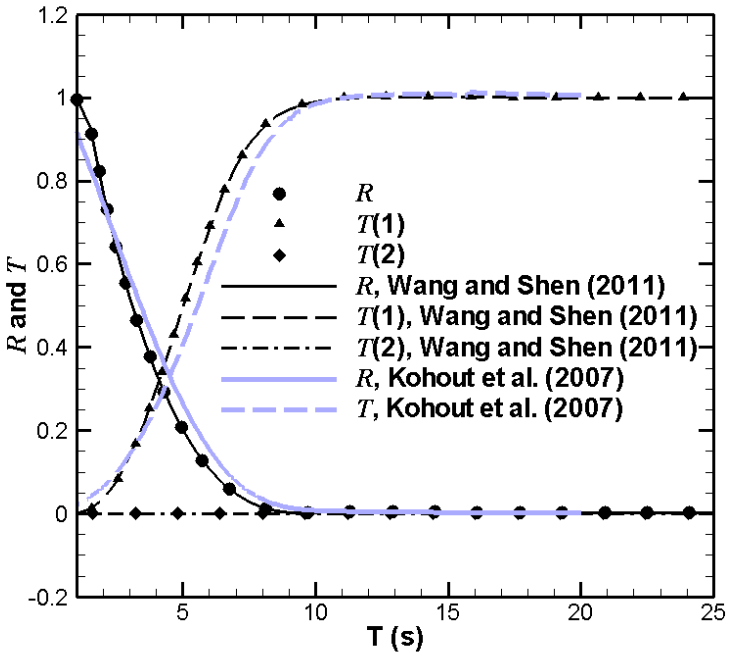

Fig. 4-4 Comparison between previous and the present studies of the reflection and transmission coefficients from open water to an elastic cover with respect to wave period. Here ν=0m^2/s for both regions, G_1 =0.001Pa, G_3 =1GPa, h_1=0.001m, and h_3=0.5m. In this and the rest of the figures, $\rho_{ice} = 917 kg/m^3$, $\rho_{water} = 1000 kg/m^3$, $H = 100 m$. (The dark solid line coincides with the circles. The dark dash line coincides with the triangles. The dark dash-dot line coincides with the diamonds.)

4.4.2 Between thin and thick elastic ice

Next we consider a case with a vanishing h_1 and a finite h_3 but keeping the same shear modulus in both ice regions. This case represents the wave propagation from an elastic membrane into an ice cover. The resulting reflection and transmission coefficients are plotted in Figs. 4-5 and 4-6. From Fig. 4-5, it is clear that when h_1 decreases wave transmission converges to that of the case from open water to an ice cover. However, the

reflection coefficient is different. Convergence is still observed when h_1 decreases, but the results differ from the open water case except for long waves. The constitutive behavior of the membrane affects the reflection even though its thickness is negligible. This effect diminishes when the shear modulus of the membrane approaches zero, as observed earlier in Fig. 4-4.

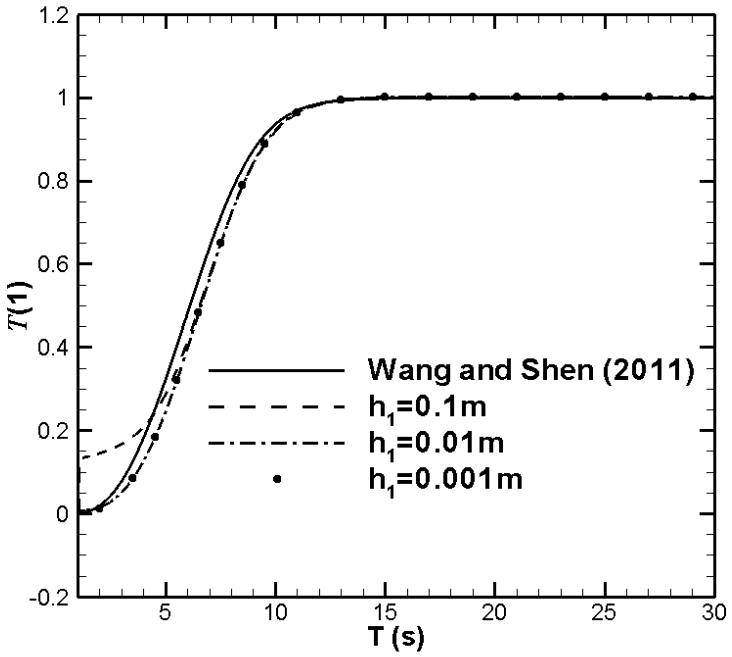

Fig. 4-5 Transmission coefficient with respect to wave period between a thin elastic cover and finite thickness elastic cover. Here ν =0m^2/s for both regions, $G_1 = G_3$ =5GPa, h_3 =0.5m. (The dash-dot line coincides with the circles.)

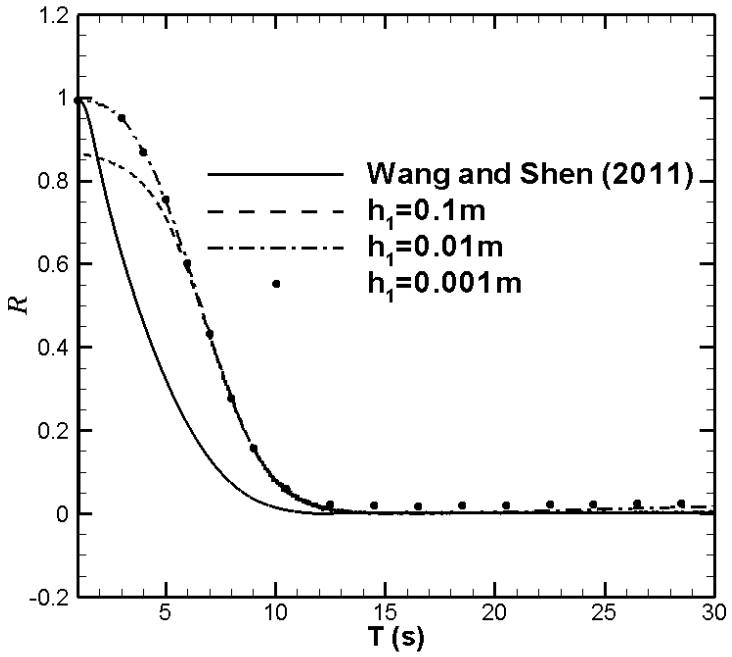

Fig. 4-6 Reflection coefficient with respect to wave period between a thin elastic cover and finite thickness elastic cover. Here ν=0m^2/s for both regions, $G_1 = G_3$ =5GPa, h_3=0.5m. (The dash-dot line coincides with the circles.)

4.4.3 Between arbitrary elastic ice covers

We now consider two linear elastic ice covers with different properties. This case has been studied by Barrett and Squire [20] using the thin elastic plate theory. First we present the case where the shear modulus differs between the two ice regions, all other parameters are identical. The results are shown in Fig. 4-7. We have also tested the case where two ice regions are identical. The results show $T = 1$ and $R = 0$ for all wave periods, as expected. Next we examine the case when the ice thickness is different between the two regions, the rest of the parameters are identical. The results are shown in Fig. 4-8.

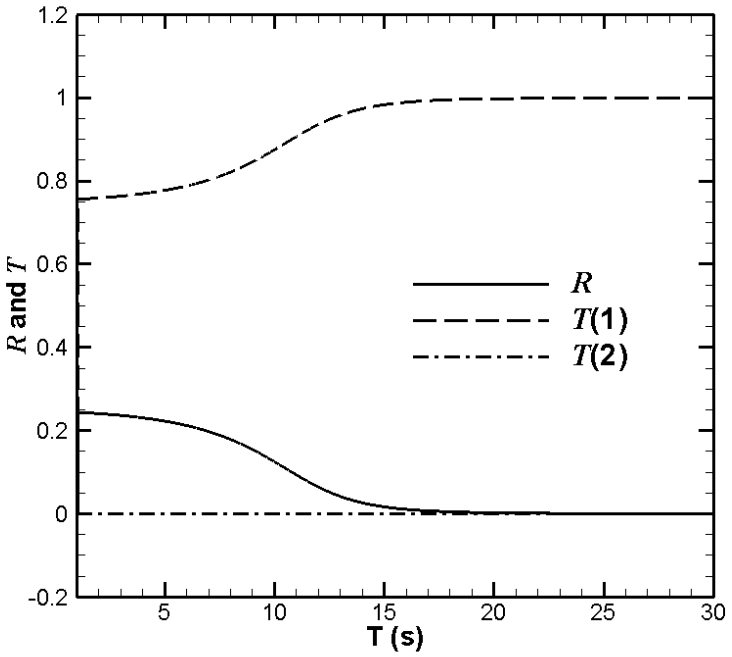

Fig. 4-7 Reflection and transmission coefficients with respect to wave period between two elastic ice regions with ν=0m2/s in both regions, G_1 =2.5GPa, G_3 =5GPa, and $h_1 = h_3$=1m.

The above reflection and transmission coefficients are qualitatively the same as in Barrett and Squire [20] if their smoothly joined sheet boundary conditions are used. The quantitative difference is substantial at low wave periods but diminishes at high periods. The difference is particularly noticeable for the reflection coefficient. For example, for a 1 sec wave, the reflection coefficient for the case shown in Fig. 4-7 is about 0.05 from Barrett and Squire [20] but from the present calculation it is about 0.25. The difference in transmission is less. For a 1 sec wave, it is about 0.9 from Barrett and Squire [20] and 0.7 from the present calculation. The differences in both reflection and transmission become negligible for long wave periods. This difference may be a combination of our approximation in treating the boundary conditions, in ignoring the evanescent modes, as

well as the continuum considerations used in the ice regions (instead of the thin elastic plate assumption). Further investigation to identify the source of these differences awaits a more complete mathematical study currently underway.

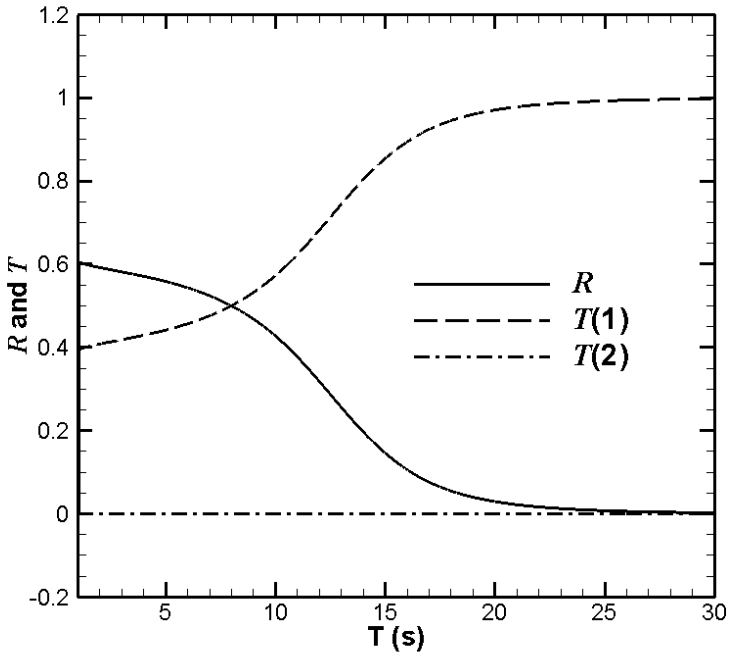

Fig. 4-8 Reflection and transmission coefficients with respect to wave period between two elastic ice regions with ν =0m^2/s in both regions, $G_1 = G_3$ =5GPa, and h_1 =1m, h_3=2m.

4.5 Viscoelastic cases

We next study the full viscoelastic case. Each ice region is now considered as a viscoelastic material with different properties. In this section, both $R(1)$ and $R(2)$ are included.

4.5.1 Between viscoelastic ice

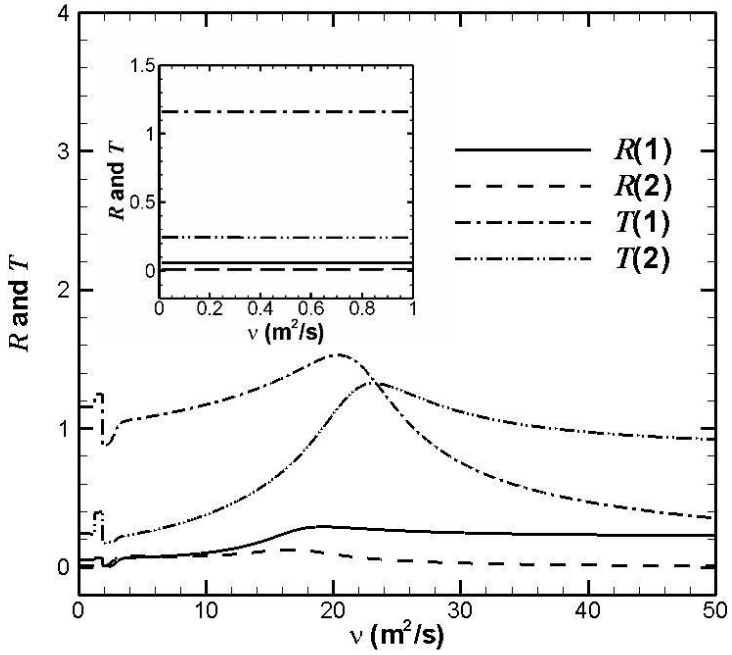

Fig. 4-9 Reflection and transmission coefficients with respect to viscosity between two thin elastic ice covers with T =6s, G =10^4Pa, and h_1 =1m, h_3 =2m.

First we examine regions of two different thicknesses. This case corresponds to an ice cover of the same physical composition but varying thickness. In each case, we let h_1 =1m , h_3 =2m. Properties in these two regions are otherwise identical. We study the influence of viscosity for three different shear moduli: low, intermediate, and high. These results are shown in Figs. 4-9, 4-10, and 4-11, respectively. As shown in Fig. 4-9, for low shear modulus, over a very large range, viscosity has strong effect on the transmission and reflection coefficients. Such dependence on viscosity appears to vanish as shear modulus increases for all three cases. However, looking close at the smaller range of viscosity, as shown in the insets of each figure, a different picture is found. The viscosity effect for $0<\nu<1\text{m}^2/\text{s}$ is most pronounced for the case with highest shear modulus. In fact,

upon close examination, viscosity does change the behavior of the transmission and reflection, but its influence is pushed down towards lower values of viscosity as the shear modulus grows.

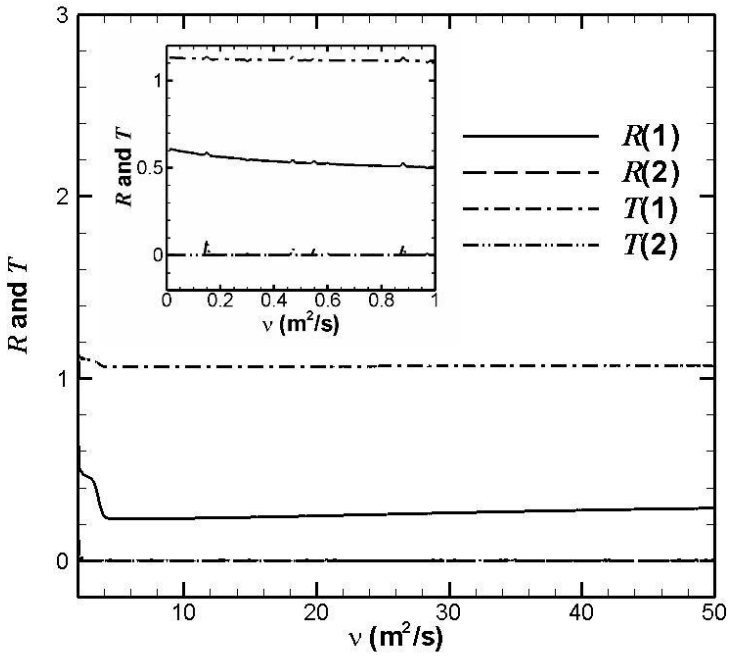

Fig. 4-10 The same as in Fig. 4-9, except that $G = 10^5$Pa . ($R(2)$ and $T(2)$ are both very close to zero)

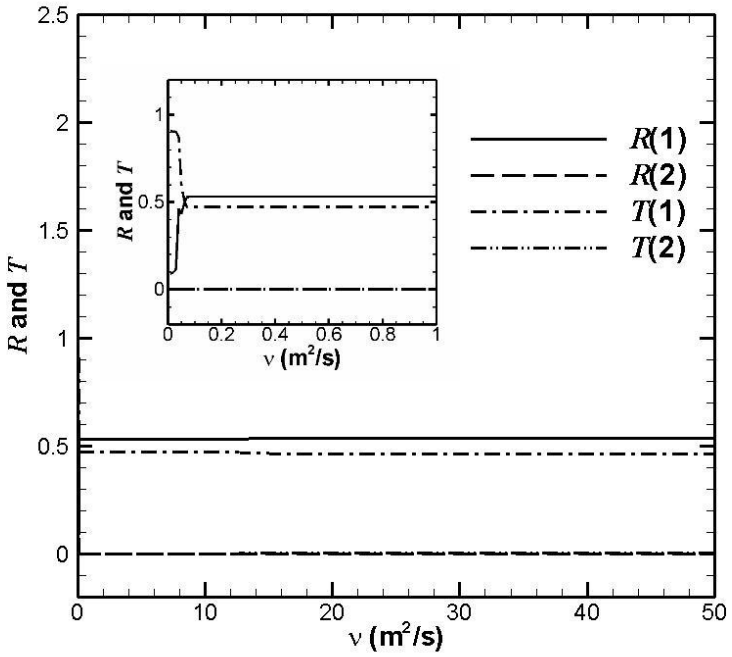

Fig. 4-11 The same as in Fig. 9, except that G =1GPa. ($R(2)$ and $T(2)$ are both very close to zero.)

4.5.2 Effect of shear modulus

In studying wave propagation from open water to a viscoelastic cover, a mode switching phenomenon was observed between the two modes included in the approximate solution [58]. One of the two modes having most of the transmitted energy was called the dominant mode. It was found that between open water and an elastic cover, as the shear modulus increased, the dominant mode changed from one to the other. In this section, we investigate the energy partition between these two modes between viscoelastic covers. The transmission and reflection coefficients are shown in Figs. 4-12 and 4-13 for the two modes over a range of the shear modulus. Just like in the previous case between open water and an elastic cover, the mode with a greater transmission

switched from one to the other in the range of $G = 10^4$-10^5Pa. The viscosity can influence the presence of mode switching. Between ν=0 and 5m^2/s, there is little difference as shown in Fig. 4-12. Increasing the viscosity to 50m^2/s, the mode switching stops as shown in Fig. 4-13. Having such a large viscosity is unlikely for the ice cover. However, when considering the ice cover together with the boundary layer underneath, the full dissipation mechanism of this upper layer in the wave field may result in a large effective viscosity. Whether what found in the current model is physically observable remains to be seen.

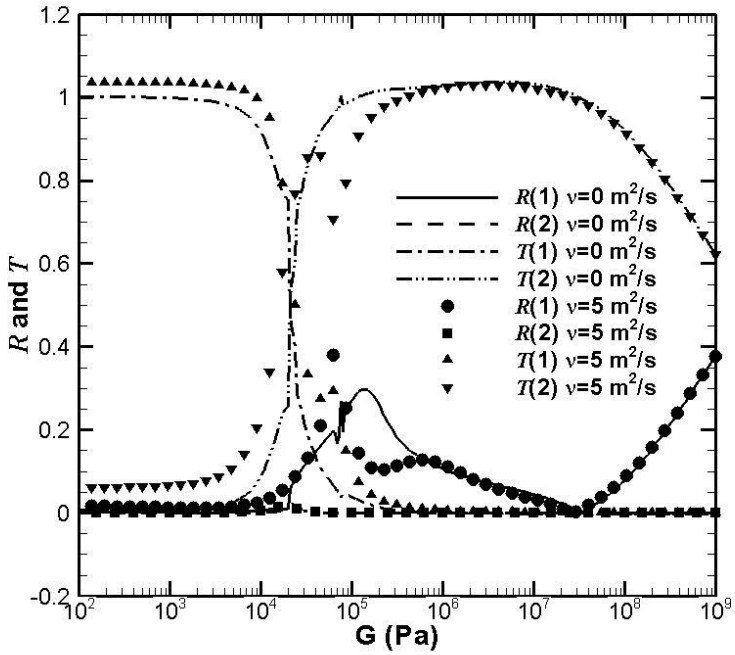

Fig. 4-12 Reflection and transmission coefficients between two viscoelastic ice covers with ν=0m2/s or 5m^2/s , T =6s, and h_1=0.1m, h_3=0.5m. (Two $R(2)$ are both very close to zero.)

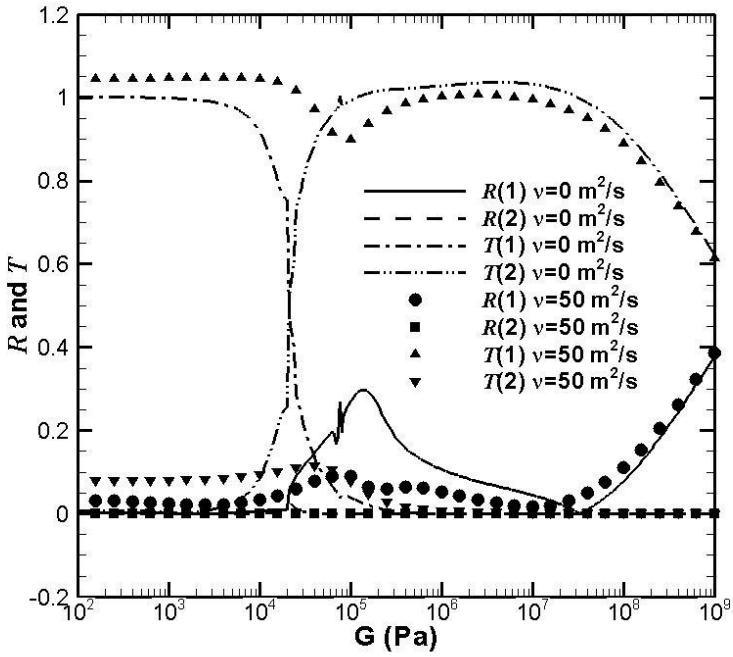

Fig. 4-13 The same as in Fig.6-12 except that ν =0m2/s or 50m^2/s . (Two $R(2)$ are both very close to zero.)

We also tested the case when water depth is 1000m. There is no discernible difference from the H =100m case. The insensitivity to water depth may be an artifact of the approximation, since we keep only two modes in the solution.

4.5.3 Grease ice and elastic ice

As mentioned in the introduction, although this study is intended for a geophysical scale model, the same analysis is also applicable to floe scale process. We thus study a relevant case here. Figures 4-14 and 4-15 show results of a wave propagating from a pure viscous layer to a pure elastic cover. This situation corresponds to an ice floe surrounded by grease ice. We test a pure viscous case ν_1=0.01m^2/s in region 1 and let

regions 3 be pure elastic. This viscosity is chosen based on the experimental study of grease ice covers [52]. The results are compared to the wave propagation from open water (with ν=0m2/s and G_1=0Pa) to the same elastic cover in region 3. We choose two cases for the elastic region: an intermediate shear modulus (G_3=0.05GPa) and a high shear modulus (G_3=5GPa). As shown in Figs. 4-14 and 4-15, $R(2)$ is non-zero for small period, but the transmission and reflection coefficients for the dominant mode are unaffected whether it is from open water or from a grease ice layer.

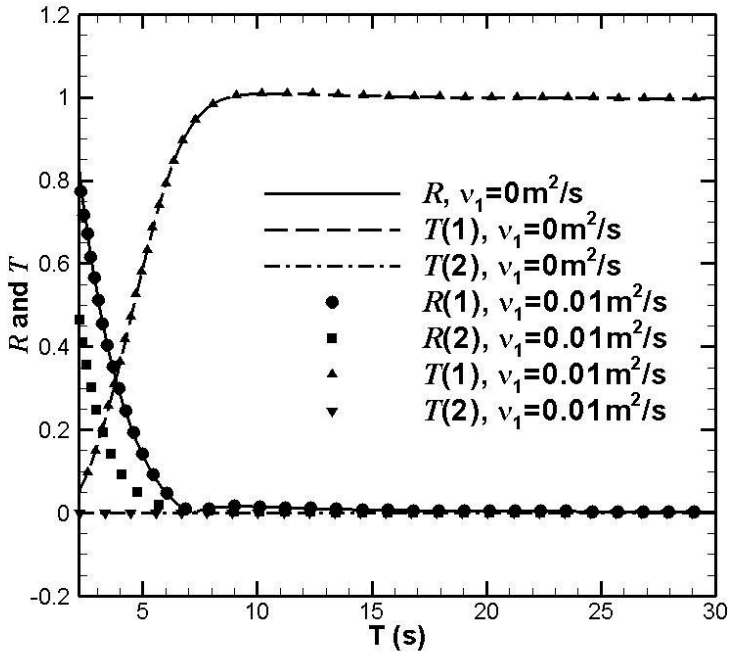

Fig. 4-14 Reflection and transmission coefficients with respect to wave period from open water or a pure viscous ice to a pure elastic ice with G_1=0Pa, ν_1=0m^2/s or 0.01m^2/s , G_3=0.05GPa, ν_3=0m2/s , and h_1=1m, h_3=1m.

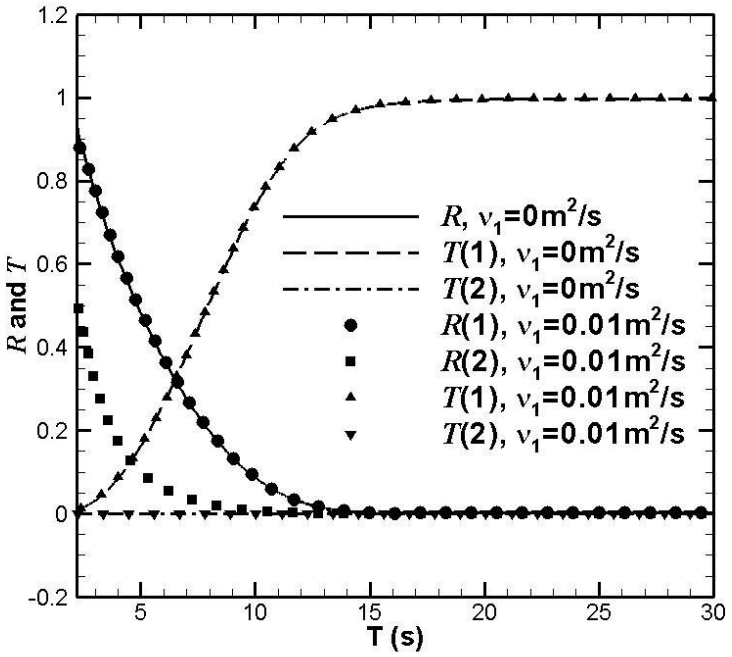

Fig. 4-15 The same as in Fig.4-14, except that G_3 =5GPa.

4.6 Summary

In the present study, the approximate mode decomposition method for solving ocean wave propagating from open water to an ice-covered region is extended to two connected ice-covered regions. In each region the ice cover is modeled as a viscoelastic continuum.

4.6.1 Boundary conditions

The boundary conditions in the vertical direction are the same as in Wang and Shen [58]. These conditions have been used to obtain the dispersion relation. In which, the attenuation coefficient and the wavelength have been obtained. The boundary conditions in the horizontal direction included more constraints from the previous study

of Wang and Shen [58]. In addition to requiring the continuity conditions of horizontal velocity and normal stress, we also consider the continuity conditions of shear stress and vertical velocity. Equivalent conditions were included by Barrett and Squire [26] for thin elastic plate models. For ice-ice interface, we also include the vertical velocity continuity condition to achieve the non-slip boundary condition. In Wang and Shen [58], continuity of shear stress was first included in the solution procedure. The solutions showed no influence of including this condition in the case of open water connecting to a viscoelastic cover. Hence this condition was dropped later in that study. For the present case we have kept this condition. However, because the magnitude of shear stress is proportional to the shear modulus, with its large value this constraint makes the convergence to the solution extremely difficult. To avoid the divergence of the results when solving for the reflection and transmission coefficients, we use a weighting factor of $0.1/G$ for the shear stress boundary condition when applying the singular value decomposition procedure. With this weighting factor, the solutions converge easily.

Instead of requiring a minimum overall error throughout the boundaries as in Fox and Squire [18, 19], we only require the mean values on both sides of the interface be the same. This approximation as adopted in Wang and Shen [58] makes the solution procedure much simpler. Because of the approximation, results for shorter waves presented here are less accurate.

To investigate the amount of error introduce by this approximation, Fig. 4-16 shows the contribution of error from each of the boundary conditions in Eqs. (4.20-4.28). For the selected example, the parameters are $G_1 = G_3$ =5GPa, $\nu_1 = \nu_3$ =0m^2/s, h_1 =1m, h_3 =2m and H =100m. In this figure, we plot the integrals in Eq. (4.30) one term at a time.

The behaviors of the errors can be separated into four distinct groups. The first group is the errors from Eqs. (4.20) and (4.21) for water-water interface. This group shows a fast decay with increasing period, hence they are the main error sources for low period waves. The second group is Eqs. (4.22), (4.25) and (4.26). These equations represent the velocity boundary conditions. This group is flat with a small magnitude, hence does not contribute significantly to error. The third group contains the normal stress terms, Eqs. (4.23) and (4.27), and the shear stress term, Eq. (4.28). Similar to the second group, the third group is also flat with very small magnitude. The fourth group is from the shear stress boundary condition, Eq. (4.24). This error increases with increasing period, thus becomes the main error source for large periods. Of the nine boundary conditions, Eq. (4.24) is the most challenging. It represents the matching of shear stress between the vertical interface of water and ice. Referring to Fig. 4-3, this interface is below water. On the left side the shear stress must be uniformly zero due to the inviscid water. Thus the shear stress must also vanish on the ice side where it meets water. However, above the water-ice interface, still at $x = 0$, is the ice-ice interface where the shear stress is not zero. The normal stress at the same interface does not suffer this jump condition, because the continuity of normal stress between regions 1 and 2 and regions 1 and 3 helps to smoothly connect the normal stress between regions 2 and 3. Nevertheless, the increase of error from Eq. (4.24) with wave period is mild. Its magnitude is small even for long period waves thus should not influence the solution significantly as is evident from Fig. 4-4. We also study the errors for other parameters, and we found the distributions of the errors for other cases are very similar as Fig. 4-16.

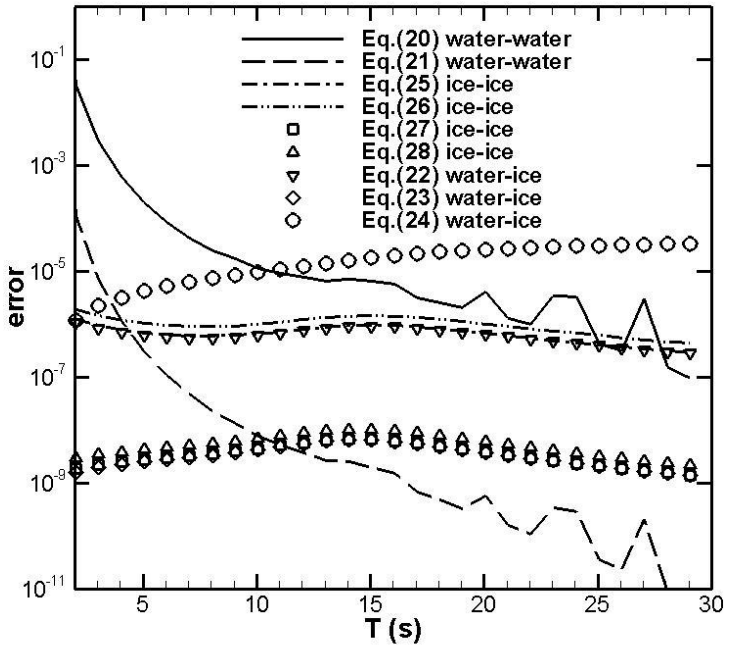

Fig. 4-16 Error terms from different boundary conditions: $G_1 = G_3$ =5GPa, $\nu_1 = \nu_3$ =0m^2/s, h_1 =1m, h_3 =2m and H =100m.

Improvement of the solution using the variational method to solve the boundary conditions together with including more modes from the dispersion relation is underway and will be presented in the future. The errors discussed above are expected to reduce with the improved solution procedure. Partial submergence is also desired in order to more closely describe floating ice covers.

4.6.2 Wave transmission and reflection between two elastic covers

To compare with previously established wave transmission and reflection, we investigate the case between two elastic covers and compare the present results with the thin elastic plate model. The cases for changes on ice thickness and shear modulus

between the two ice-covered regions are studied as shown in Figs. 4-7 and 4-8. We find that present results are qualitatively the same as in Barrett and Squire [20] under their smoothly joined sheet boundary conditions. The quantitative difference may come from our ignoring the evanescent modes, keeping only two modes, and possibly our inclusion of the constitutive relation and the resulting boundary conditions between the ice regions. When we set the thickness and shear modulus of the upstream side of the ice region to zero, the results converge to open water connecting to an elastic cover as shown in Figs. 4-4, 4-5, 4-6.

4.6.3 Effect of viscosity

After validating the current formulation and solution procedure by comparing the results with previously published work, we calculate the viscoelastic case. Several interesting phenomena are found. First, the mode switching that occurs as shear modulus increases stops at very high viscosity (see Fig. 4-13). Interest in such phenomena is at present only academic, because no evidence of such high effective viscosity is physically possible. Second, the transmission from a pure viscous cover to an elastic cover is the same as that from open water to an elastic cover, Figs. 4-14, 4-15. The reflection of the dominant mode is also unaffected whether it is from open water or from a viscous layer. The non-zero $R(2)$ is more pronounced for shorter waves. Solutions of the transmission and reflection are influenced by evanescent modes more for shorter waves. Hence the magnitude of $R(2)$ may change when these modes are included. When the propagation direction is reversed, i.e. from the elastic cover to open water or a viscous cover, we need to determine if the same insensitivity to open water or grease ice still holds. If so, then results from wave scattering in a dispersed floe field should apply to cases of floes

dispersed in a slurry. Although not intended in this study, this result is relevant for floe scale models.

Finally, viscosity does have an effect on wave transmission and reflection when the ice cover is not pure viscous. As shown in Figs. 4-9, 4-10, 4-11, the influence of viscosity in a viscoelastic cover is evident.

4.6.4 Application of viscoelastic model in the numerical wave model

Assuming water depth is constant, based on Eq.(2.1) the evolution equation of the wave spectra is

$$\frac{DN(f,\theta,\vec{x},t)}{Dt} = S(f,\theta,\vec{x},t) \tag{4.51}$$

where N is the wave action density and S is the source-sink term. At present, the effect of ice is considered via an artificial blocking of energy flux between computational cells. Specifically, the advection of energy $\vec{c}_g N$ between computational cells is modified by a "transparency" coefficient which depends on the ice concentration. In the above, $\vec{c}_g$ is the group velocity. A process-based wave-ice interaction model will improve the parameterization of the existing wave models. The viscoelastic model presented here has the ability to include the elastic characteristics of a solid ice cover and the viscous characteristics of a fragmented ice field. It also has the ability to include other damping mechanisms such as the scattering, floe-floe interactions and flexing hysteresis. The dispersion relation given in Wang and Shen [58] provides a way to calculate $\vec{c}_g$ and S. The transmission and reflection developed in the present study provides a way to calculate the "transparency" coefficient. Instead of using ice concentration as the single parameter, the wave model will use the shear modulus and viscosity as new parameters.

The advantage is that frequency-dependent damping and transmission of energy may be more realistically modeled. The challenge will be to determine the effective shear modulus and viscosity for a given ice field subject to a given wave frequency.

4.7 Conclusions

In this chapter a solution procedure is developed for the transmission and reflection between two dissimilar ice covers. The ice covers are conceptually represented by two parameters: shear modulus and viscosity. For extreme cases such as grease ice, the shear modulus vanishes and the ice cover behaves as a viscous material; for a consolidated ice cover the shear modulus approaches that of the solid ice and the cover behaves as an elastic material. The infinite series of all admissible modes of the dispersion relation is truncated to two closest to the open water mode. For very large or small shear modulus, only one of these modes is significant. The other has extremely low wave number associated with near zero transmission. But for intermediate shear modulus, there is a transition phenomenon between the two modes. These phenomena have been discovered in the earlier work for wave propagation from open water into a viscoelastic ice region [58]. In the present study, it is found that at large viscosity the mode switching phenomenon disappears. It also disappears for long period waves. The work presented here is a natural extension to the previous study of Wang and Shen [58]. The method shown may be used to prepare a numerical scheme for wave modeling under a heterogeneous ice cover. The results shown also provides evidence that at floe scale, wave scattering from elastic ice floes dispersed in a grease/brash ice field is nearly the same as those dispersed in open water. Due to the nature of the approximation, for short

period waves the solutions are less accurate. Improvements may be made by including more modes and better treating the boundary conditions, the subject of the next chapter.

CHAPTER 5 VARIATIONAL METHOD

Modeling ice covers as viscoelastic continua, in chapter 4 we apply an approximate method to determine the transmission and reflection between two different ice covers. This approximate solution considered only two modes of the dispersion relation, and the horizontal boundary conditions were satisfied by matching mean values over the interfaces. In this chapter, we employ a more rigorous variational method [18] to calculate the wave transmission and reflection from two connecting viscoelastic ice covers of different properties. The variational approach minimizes the overall error function at the interface of two ice covers. The effect of additional travelling and evanescent modes are also investigated. We compare results from different matching methods, as well as the effects of including additional modes. From the study of this chapter, we find that additional modes do not always improve the results. For all cases tested, two modes appear to be sufficient. These two modes represent the open-water-like and the elastic pressure wave behavior. The approximate method and the variational method have similar results except at very short wave periods.

5.1 Intorduction

The approximate method in chapter 4 has the obvious advantage of being simpler and computationally faster. However, its accuracy is uncertain until we compare the results with a better mathematical procedure that includes more admissible modes and treats the boundary conditions more rigorously. In this chapter, we examine the effect of including more modes that exist in the dispersion relation, including both propagating and evanescent modes. We also improve the matching criterion by using a variational

method as in Fox and Squire [18]. We compare these new results with the approximate method, and previous studies that assumed ice covers as pure elastic materials. A linear wave regime is assumed in this study.

5.2 Theoretical formulation

The problem to be analyzed is two dimensional as shown in chapter 4. The two ice covers are assumed to be fully submerged. The x direction is aligned with the incoming wave direction, and the z direction is opposite to gravity. The origin is set at the top of the ice cover right between the two ice regions. As shown in Fig. 4-1, there are four regions: ice region 1 and 3; water region 2 and 4. A monochromatic wave propagates from left to right. The ice thicknesses for regions 1 and 3 are h_1 and h_3, respectively. The total depth of the domain is H. The special case corresponding to open water wave propagating into an ice cover is represented by setting $h_1 = 0$. The governing equations and boundary conditions are the same as in the chapter 4.

5.3 Solutions

The variational method is developed to solve transmission and reflection from open water to a thin elastic plate [18]. Using this method, Fox and Squire were able to examine the importance of matching boundary condition through the water depth instead of just at the free surface, as well as the inclusion of the two damped traveling modes and evanescent modes. Here, we extend the method to the viscoelastic model. This method is more rigorous than the approximate method used in Wang and Shen [58]. In the approximate method, we satisfy all horizontal boundary condition by forcing the average values across the interface to be equal. In the variational method we minimize the

differences across the entire interface. As in Fox and Squire [18], we define the error function based on the horizontal boundary conditions as follows

$$\begin{aligned}\varepsilon &= \lambda_1\int_{-H}^{-h_3}\left(\varphi_2(0,z)-\varphi_4(0,z)\right)^2dz+\lambda_2\int_{-H}^{-h_3}\left(u_2(0,z)-u_4(0,z)\right)^2dz\\&+\lambda_3\int_{-h_1}^{0}\left(u_1(0,z)-u_3(0,z)\right)^2dz+\lambda_4\int_{-h_1}^{0}\left(w_1(0,z)-w_3(0,z)\right)^2dz\\&+\lambda_5\int_{-h_1}^{0}\left(\tau_{xx1}(0,z)-\tau_{xx3}(0,z)\right)^2dz+\lambda_6\int_{-h_1}^{0}\left(\tau_{xz1}(0,z)-\tau_{xz3}(0,z)\right)^2dz\\&+\lambda_7\int_{-h_3}^{-h_1}\left(u_2(0,z)-u_3(0,z)\right)^2dz+\lambda_8\int_{-h_3}^{-h_1}\left(\tau_{xx2}(0,z)-\tau_{xx3}(0,z)\right)^2dz\\&+\lambda_9\int_{-h_3}^{-h_1}\tau_{xz3}^2(0,z)dz,\end{aligned}\qquad(5.1)$$

where $\{\lambda_n\}_{n=1}^{9}$ are the Lagrange multipliers which are chosen to optimize the convergence. The key difference of the approximate method and the variational method is this error function. Let F_{iL}, F_{iR} be any property F_i at the left and right side of an interface, respectively. In the approximate method the error is defined as $\sum_i\int(F_{iL}-F_{iR})dz$ and in the variational method as $\sum_i\lambda_i\int\left(F_{iL}-F_{iR}\right)^2dz$ where the integral is taken over the interface along z. Obviously the error requirement defined in Eq. (5.1) is more stringent. In addition, we will include more propagating modes than the two closest to the open water case as well as N' evanescent modes to form the general solution. In the approximate method [58, 59], we included only two propagating modes and none of the evanescent modes. Thus, for the present study, the total potential function and the stream function may be written in terms of these $M+N'$ modes as follows, where the individual modes are denoted by $n=1,2,\cdots,M+N'$.

$$\begin{aligned}\varphi_1(x,z,t) &= I(1)(A_1(1)\cosh k_1(1)z+B_1(1)\sinh k_1(1)z)e^{ik_1(1)x}e^{-i\omega t}\\&+\sum_{n=1}^{M+N'}\mathcal{R}(n)(A_1(n)\cosh k_1(n)z+B_1(n)\sinh k_1(n)z)e^{-ik_1(n)x}e^{-i\omega t}\quad;\end{aligned}\qquad(5.2)$$

$$\psi_1(x,z,t) = I(1)(C_1(1)\cosh\alpha_1(1)z + D_1(1)\sinh\alpha_1(1)z)e^{ik_1(1)x}e^{-i\omega t} + \sum_{n=1}^{M+N'}\mathcal{R}(n)(C_1(n)\cosh\alpha_1(n)z + D_1(n)\sinh\alpha_1(n)z)e^{-ik_1(n)x}e^{-i\omega t} \quad ; \tag{5.3}$$

$$\varphi_2(x,z,t) = I(1)E_1(1)\cosh k_1(1)(z+H)e^{ik_1(1)x}e^{-i\omega t} + \sum_{n=1}^{M+N'}\mathcal{R}(n)E_1(n)\cosh k_1(n)(z+H)e^{-ik_1(n)x}e^{-i\omega t} \quad ; \tag{5.4}$$

$$\varphi_3(x,z,t) = \sum_{n=1}^{M+N'}\mathcal{T}(n)(A_3(n)\cosh k_3(n)z + B_3(n)\sinh k_3(n)z)e^{ik_3(n)x}e^{-i\omega t} \; ; \tag{5.5}$$

$$\psi_3(x,z,t) = \sum_{n=1}^{M+N'}\mathcal{T}(n)(C_3(n)\cosh\alpha_3(n)z + D_3(n)\sinh\alpha_3(n)z)e^{ik_3(n)x}e^{-i\omega t} \; ; \tag{5.6}$$

$$\varphi_4(x,z,t) = \sum_{n=1}^{M+N'}\mathcal{T}(n)E_3(n)\cosh k_3(n)(z+H)e^{ik_3(n)x}e^{-i\omega t} \; ; \tag{5.7}$$

The coefficients $A_i(n)$, $B_i(n)$, $C_i(n)$, $D_i(n)$, $E_i(n)$ are solved with the singular value decomposition method. We then substitute them into the horizontal boundary conditions to form error function in terms of $I(1)$, $\mathcal{R}(n)$, and $\mathcal{T}(n)$. The error function contains $2(M+N')+1$ unknowns $I(1)$, $\{\mathcal{R}(n)\}_{n=1}^{M+N'}$, and $\{\mathcal{T}(n)\}_{n=1}^{M+N'}$. In vector form these unknowns are

$$\mathbf{u} = \left(I(1),\mathcal{R}(1),\mathcal{R}(2),\cdots\mathcal{R}(M+N'),\mathcal{T}(1),\mathcal{T}(2),\cdots,\mathcal{T}(M+N')\right)^T. \tag{5.8}$$

The error function can be rewritten as follows

$$\varepsilon = \mathbf{u}^T\left(\lambda_1\mathbf{Q}_1 + \lambda_2\mathbf{Q}_2 + \lambda_3\mathbf{Q}_3 + \lambda_4\mathbf{Q}_4 + \lambda_5\mathbf{Q}_5 + \lambda_6\mathbf{Q}_6 + \lambda_7\mathbf{Q}_7 + \lambda_8\mathbf{Q}_8 + \lambda_9\mathbf{Q}_9\right)\mathbf{u}. \tag{5.9}$$

The matrix $\mathbf{Q}_n$ is calculated analytically as in Appendix F. To set the constraint of $I(1)=1$, we introduce a square matrix $\mathbf{K}$, which projects the coefficients vector $\mathbf{u}$ onto the incident wave coefficient vector $\mathbf{v}$:

$$\mathbf{K}\mathbf{u} = \mathbf{v}. \tag{5.10}$$

The vector $\mathbf{v}$ contains coefficients corresponding to $I(1)=1$ and all others being zero. In all, these constraints can be written as follows:

$$\mathbf{u}^{\mathrm{T}}\mathbf{K}\mathbf{u}-2\mathbf{v}^{\mathrm{T}}\mathbf{u}+\mathbf{v}^{T}\mathbf{v}=0. \tag{5.11}$$

Minimizing ε subject to the constraints (5.11) is performed by minimizing

$$\mathbf{u}^{T}\left(\lambda_1\mathbf{Q}_1+\lambda_2\mathbf{Q}_2+\lambda_3\mathbf{Q}_3+\lambda_4\mathbf{Q}_4+\lambda_5\mathbf{Q}_5+\lambda_6\mathbf{Q}_6+\lambda_7\mathbf{Q}_7+\lambda_8\mathbf{Q}_8+\lambda_9\mathbf{Q}_9+\eta'\mathbf{K}\right)\mathbf{u}-2\eta'\mathbf{v}^{T}\mathbf{u}. \tag{5.12}$$

Here η' is the Lagrange multiplier corresponding to the $I(1)=1$ constraint. Minimizing Eq. (5.12) is equivalent to solving the following:

$$\mathbf{Q}\mathbf{u}=\eta'\mathbf{v}, \tag{5.13}$$

where

$$\mathbf{Q}=\lambda_1\mathbf{Q}_1+\lambda_2\mathbf{Q}_2+\lambda_3\mathbf{Q}_3+\lambda_4\mathbf{Q}_4+\lambda_5\mathbf{Q}_5+\lambda_6\mathbf{Q}_6+\lambda_7\mathbf{Q}_7+\lambda_8\mathbf{Q}_8+\lambda_9\mathbf{Q}_9+\eta'\mathbf{K}. \tag{5.14}$$

With the continuity condition of the vertical displacement at the interface, we can derive the transmission and reflection coefficients for the surface profile.

$$R(n)=\frac{\left|\mathcal{R}(n)\right\|k_1(n)B_1(n)+ik_1(n)C_1(n)\right|}{\left|I(1)\right\|k_1(1)B_1(1)-ik_1(1)C_1(1)\right|}; \tag{5.15}$$

$$T(n)=\frac{\left|\mathcal{T}(n)\right\|k_3(n)B_3(n)-ik_3(n)C_3(n)\right|}{\left|I(1)\right\|k_1(1)B_1(1)-ik_1(1)C_1(1)\right|}; \tag{5.16}$$

where $n=1,2,..M$.

5.4 Results of wave transmission and reflection - pure elastic case

In this section we use the above solution procedure to study the behavior of wave propagation involving pure elastic ice covers. The results are compared with existing theories. For all cases shown, $\rho_{ice}=917\,\mathrm{kg/m^3}$, $\rho_{water}=1000\,\mathrm{kg/m^3}$, $H=100\,\mathrm{m}$. Based

on the estimation of the magnitude for each error term, we choose the Lagrange multipliers as $\lambda_1 = 0.01$, $\lambda_2 = \lambda_3 = \lambda_4 = \lambda_7 = 1$, $\lambda_5 = \lambda_6 = \lambda_8 = \lambda_9 = 1/G_3^2$, and $\eta' = 1000$.

5.4.1 Between open water and elastic ice

We first consider the case of wave propagation from open water to an elastic ice cover. At this point we let $M = 2$ and $N' = 0$, i.e. include only two propagating modes closest to the open water case as in chapter 4. The only improvement is that we adopt the new error function shown in Eq. (5.1). We thus focus on the effect of the more rigorous boundary matching criterion. Fig. 5-1 shows the reflected and transmitted coefficients defined in Eqs. (5.49, 5.50) with respect to the wave period for $\nu_{1,3} = 0\,\mathrm{m}^2/\mathrm{s}$, $G_1 = 0\mathrm{Pa}$, $G_3 = 1\mathrm{GPa}$, $h_1 = 0\mathrm{m}$, and $h_3 = 0.5\mathrm{m}$. The results compare the approximate method, the variational method, and a different model based on the thin elastic plate theory where the matched eigenfunction expansion method was used [57]. In their study 20 eigenmodes were included. However, due to the thin elastic plate assumption, they reduced the shear and bending boundary conditions at the interface to a point. Treatment of such boundary condition is closer to matching the mean values at the interface as done in Wang and Shen [58]. Consequently Wang and Shen agreed better with Kohout et al. than the current results. Comparing Figs. 5-1a and 5-1b, all three cases converge to each other when h_3 reduces.

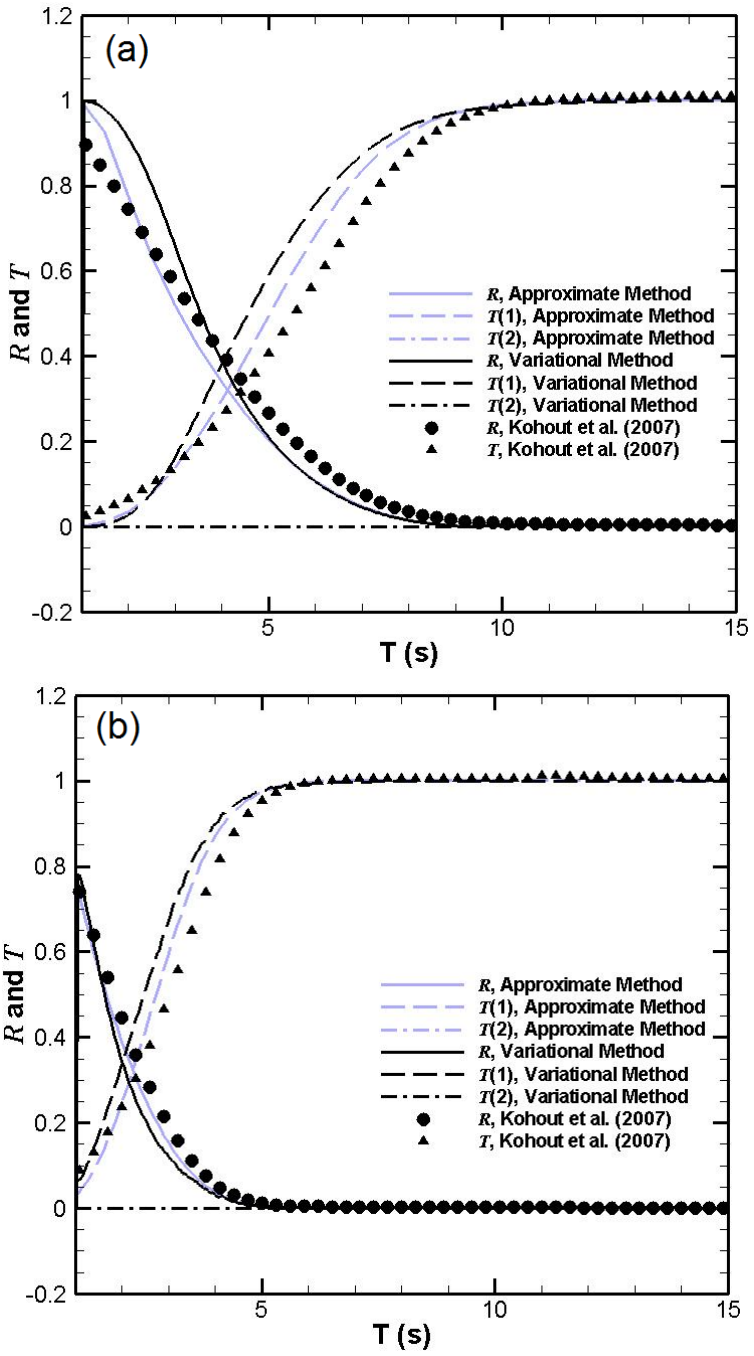

Fig. 5-1 Comparison between previous and the present studies of the reflection and transmission coefficients from open water to an elastic cover with respect to wave period. Here $\nu = 0\text{m}^2/\text{s}$ for both regions, $h_1 = 0\text{m}$, $G_3 = 1\text{GPa}$, and (a) $h_3 = 0.5\text{m}$; (b) $h_3 = 0.1\text{m}$. In this and the rest of the figures, $\rho_{ice} = 917 kg/m^3$, $\rho_{water} = 1000 kg/m^3$. (The dark and grey dash-dot lines coincide.)

We next examine what happens if we include more modes. First we locate these modes in the complex k-space. Fig. 5-2 shows the map of contours of the residual function $abs(Det)$ defined by the full dispersion relation as shown in Eq. (2.16). The parameters used in Fig. 5-2 are the same as in Fig. 5-1 The "islands" of these contours are either poles or zeros of $abs(Det)$. The zeros are admissible modes of the dispersion relation. Unlike the thin elastic theory where only one real root exists, there are three roots on the real axis. These three roots approach the single one shown in the thin elastic plate theory if either the elasticity increases or the ice thickness decreases. In the approximate solution we included only two of these modes. We now expand this to include five modes: three on the real axis and one pair of symmetric damped travelling waves, Fig. 5-2(a,b). We also examine the effect of evanescent modes, i.e. modes near the imaginary axis. We include 0, 10, and 100 of these modes. Fig. 5-3 shows the result of these different solutions. It is seen that the effect of additional modes is small. In fact, including a large number of additional modes seems to introduce fluctuations in the solution. From Fox and Squire [18], the evanescent modes are critical to obtain high accuracy solutions for thin elastic plate models. We will return to this issue in section 5.6. Since additional modes do not seem to change the accuracy of the transmission/reflection calculations, in the following discussions we keep only two modes and focus on comparing the approximate and variational methods.

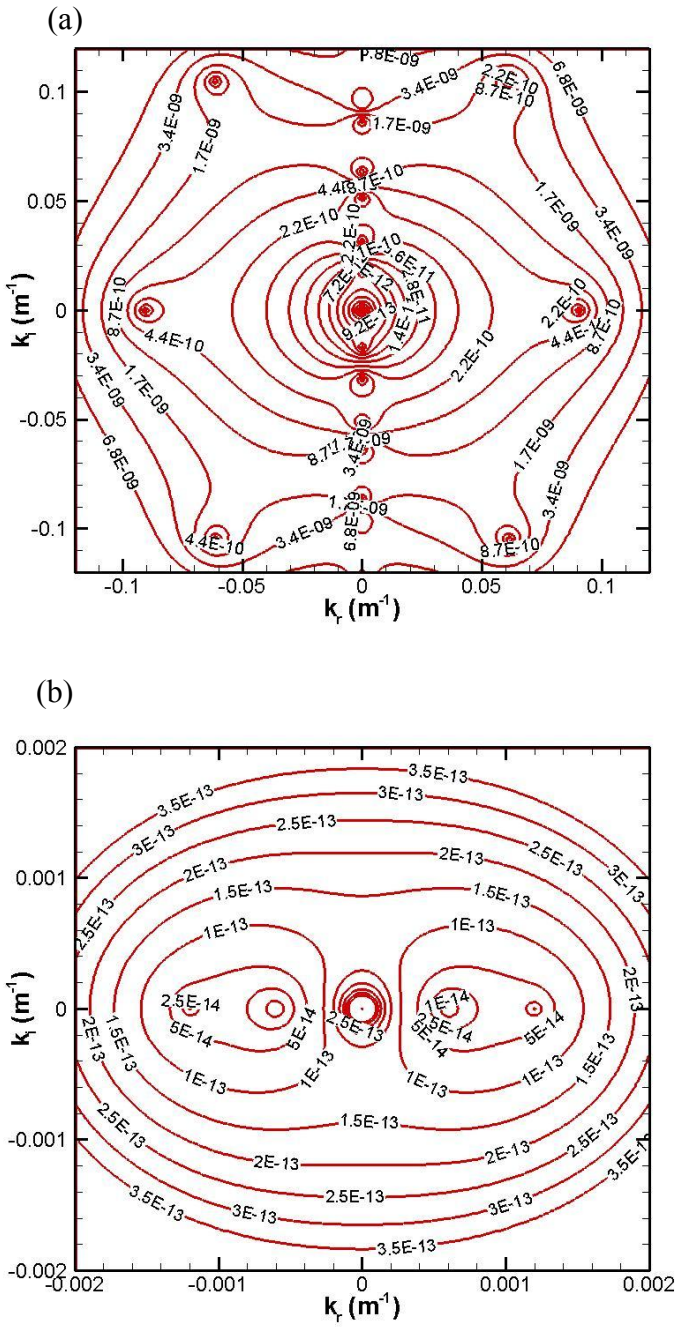

Fig. 5-2 Contour lines of the residual function $abs(Det)$. Here $\nu = 0\text{m}^2/\text{s}$, $G =$ 1GPa, and $h = 0.5\text{m}$. (a) Wide-angle view where evanescent modes, two damped traveling modes, and the third mode on the real axis is seen near $k_r = 0.1\text{m}^{-1}$; (b) Close-up view where the two modes on the real axis are seen.

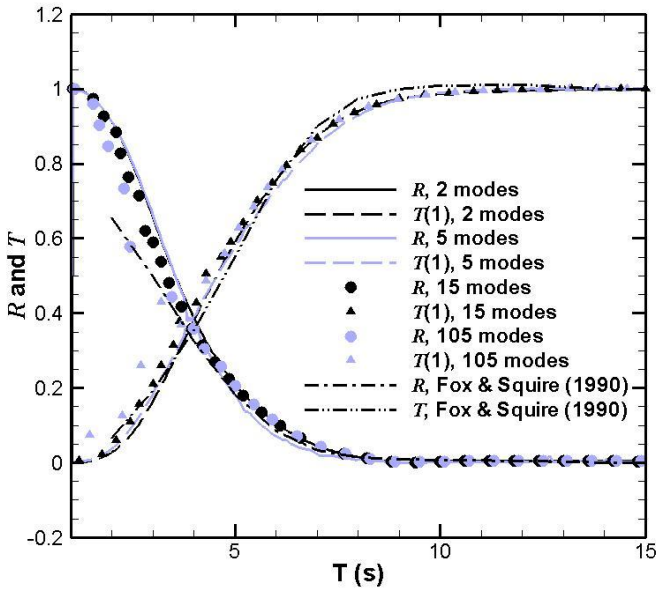

Fig. 5-3 Effect of including additional modes on transmission/reflection from open water to an elastic sheet with the same parameters as in Fig.7-1 (2 modes: include 2 propagating modes; 5 modes: add 1 additional propagating mode and 2 symmetrical damped propagating modes; 15 modes: add 10 evanescent modes to the 5 modes case. 105 modes: add 100 evanescent modes to the 5 modes case. Fox and Squire's results used 100 evanescent modes. Sukun Cheng reproduced Fox and Squire's results.)

5.4.2 Between arbitrary elastic ice covers

We now consider two linear elastic ice covers with different properties. This case has been studied by Barrett and Squire [20] using the thin elastic plate theory and the variational method. First we present the case where the shear modulus differs between the two ice regions, all other parameters are identical. The results are shown in Fig. 5-4a. Next we examine the case when the ice thickness is different between the two regions, the rest of the parameters are identical. The results are shown in Fig. 5-4b. In each case, the reflection and transmission coefficients are qualitatively the same as in Barrett and

Squire [20] if their smoothly joined plate boundary conditions are used. The quantitative difference is substantial at short wave periods but diminishes at long periods. The difference is particularly noticeable for the reflection coefficient. This difference is caused by the continuum considerations used in the ice regions instead of the thin elastic plate assumption in Barrett and Squire [20]. Using the variational method to more strictly match the boundary condition does not consistently bring the two models closer to each other.

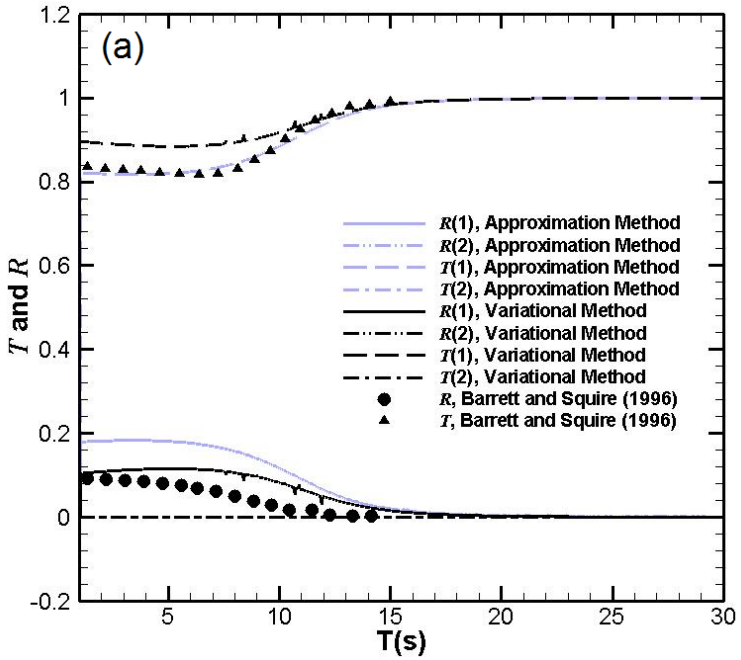

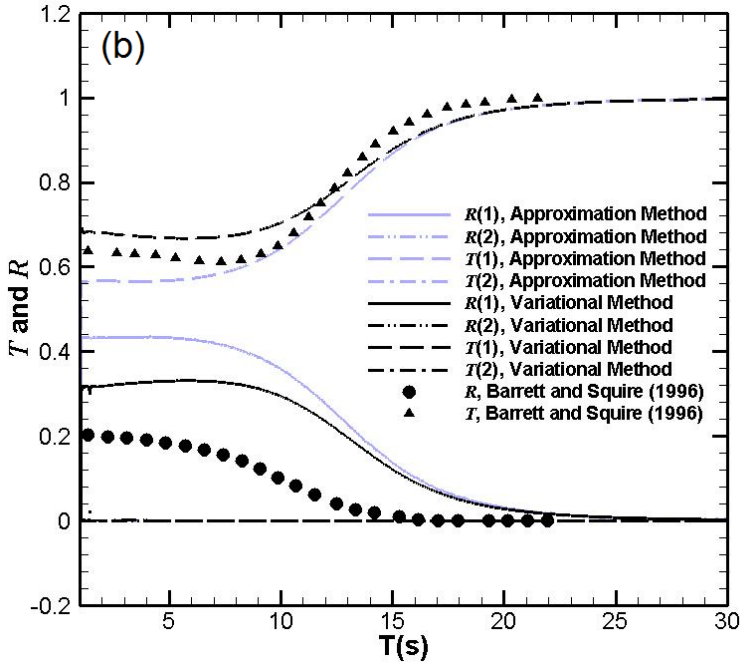

Fig.5-4 Reflection and transmission coefficients with respect to wave period between two elastic ice regions with $\nu = 0\text{m}^2/\text{s}$ in both regions. (a) $G_1 = 2\text{GPa}$, $G_3 = 5\text{GPa}$, and $h_1 = h_3 = 1\text{m}$; (b) $G_1 = G_3 = 5\text{GPa}$, $h_1 = 1\text{m}$, $h_3 = 2\text{m}$. (In both cases, $R(2)$ and $T(2)$ are zero for both approximate method and variational method.)

5.5 Energy partitions among modes in elastic ice and viscous ice

We now consider the energy partitions among three main modes and the "mode-switching" phenomenon as shown in Wang and Shen [23, 58]. Consider the case of wave propagating from open water to a pure elastic or pure viscous ice plate. In Fig. 5-5 we present the open water to pure elastic ice case by letting $h_1 = 0\,\text{m}$, $h_3 = 0.5\,\text{m}$, $\nu_3 = 0\text{m}^2/\text{s}$, $G_3 = 10^2 - 10^9\,\text{Pa}$, $\text{T} = 6\,\text{s}$. In this case there are three real roots from the dispersion relation Eq. (5.22). These are the main modes of the propagating waves. At low G one mode contains the majority of the transmitted energy. At high G the other does. The third mode which is included in the variational method but not the approximate method

has negligible energy. Between the variational and approximate methods there is little difference of the resulting energy partition between the other two modes. The two dominant modes switch their energy partitions in the range from 10^4Pa to10^5Pa. Although the 3rd mode does contain some energy, it does not change the partition between the other two modes appreciably. In Fig. 5-6 we present the open water to pure viscous ice case by letting $h_1 = 0\,\text{m},\ h_3 = 0.5\,\text{m},\ \nu_3 = 0 - 50\,\text{m}^2/\text{s},\ G_3 = 0\,\text{Pa},\ \text{T} = 6\,\text{s}$. Because of the similarity, we present only those results from the variational method. Unlike the pure elastic ice case, increasing viscosity does not create a mode switch in energy partitions. With the increasing of viscosity, the reflected wave slightly increases its energy, while the transmitted waves decrease their energies. The mode closest to the open water solution always dominates the transmitted energy, and the second mode also has certain amount of energy. The third mode is negligible.

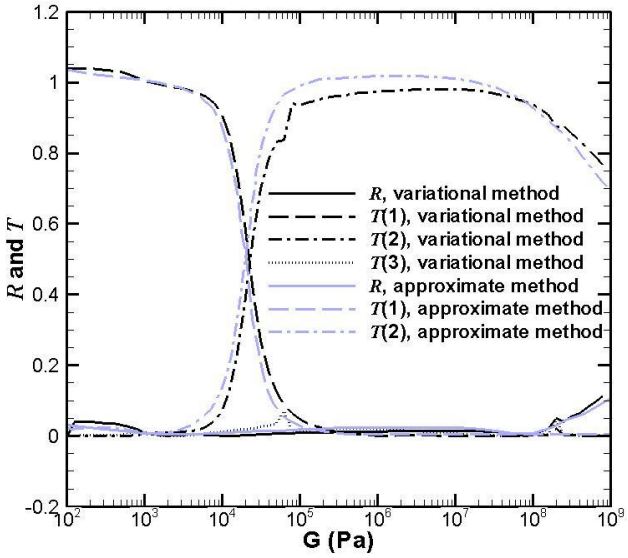

Fig. 5-5 Reflection and transmission coefficients with respect to shear modulus between open water and elastic ice with $h_1 = 0\text{m},\ h_3 = 0.5\text{m},\ \nu_3 = 0\text{m}^2/\text{s}$, and $\text{T} = 6\text{s}$.

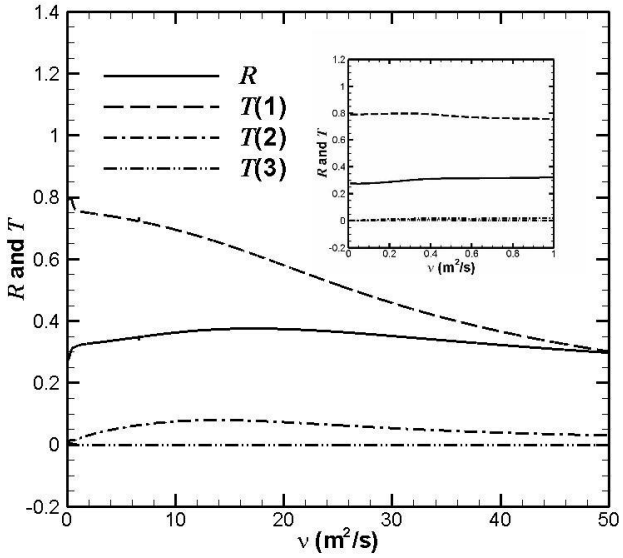

Fig. 5-6 Reflection and transmission coefficients with respect to viscosity between open water and viscous ice with $h_1 = 0$m, $h_3 = 0.5$m, $G_3 = 0$Pa, and $\mathrm{T} = 6$s.

To further understand these modes, we examine them as a function of the shear modulus G. As an example, we solve the full dispersion relation for the case $\mathrm{T} = 6\,\mathrm{s}$, $\nu = 0\,\mathrm{m}^2/\mathrm{s}$ and obtain the three real roots in the contour map for each G. In Fig. 8 the behavior of the three modes are shown. Let them be ordered such that $k_{r1} \le k_{r2} \le k_{r3}$. As G increases from 0, in the beginning the first transmitted mode appears to follow that of the open water solution. The second mode has much greater wave number to begin with, but approaches that of the open water as G increases. At around $G = 3\times10^4\,\mathrm{Pa}$ for this case, both modes are close to each other. Further increasing G makes the first mode turn downward sharply to follow the trend of the second mode while the second mode turns to approach the open water case. Eventually as G becomes very large the second mode begins to drop and coincide with the thin elastic plate theory. All this time, the third mode

constantly decreases. The third mode in this log-log plot is a straight line. Using these data we solve for its equation in the form of $k_r = aG^b$. It is found that $k_r = \omega\sqrt{\rho_{ice}/G}$ which is the elastic shear wave solution. The tangent to the asymptotes of the first and second mode is also well fitted by a straight line. Its best fit $k_r = aG^b$ yields $k_r = 16.2/\sqrt{G} \approx \omega\sqrt{\rho_{ice}/3G}$. Since we assumed that the ice cover is incompressible, its Poisson's ratio is 0.5 and the Young's modulus is $3G$, indicating that the nature of this branch of mode 1 or mode 2 is the elastic pressure wave. The above results are from a pure elastic case. This conclusion should hold for viscoelastic cases at lease when the viscosity is not too large.

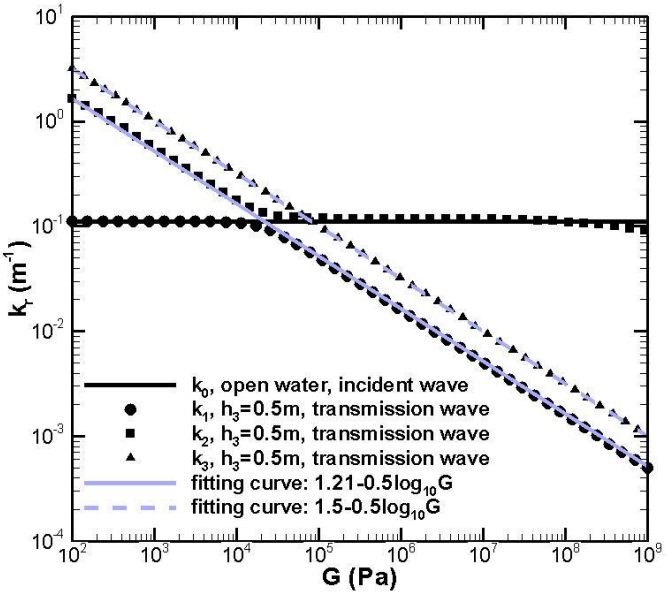

Fig. 5-7 Wave number of pure elastic ice with ν_3=0m^2/s, T=6s and h_3=0.5m, $H = 100m$.

5.6 Summary

We discuss the main findings of the present study which is based on assuming that ice covers are a viscoelastic continuum.

5.6.1 Comparison between different methods

Without changing the qualitative behavior, different methods do change the quantitative transmission/reflection between ice covers. This difference increases with the ice thickness (Fig. 5-1) due to the matching conditions at the interface: one uses the mean and the other minimizes the square differences. Between the thin elastic plate and the current solutions the differences come from a combination of boundary condition matching and the assumption of the constitutive behavior of the ice cover. This difference is less when the approximate method is used, because the boundary matching methods are very close to each other.

5.6.2 Effect of damped travelling and evanescent modes

The viscoelastic dispersion relation has many modes. Upon examining the effect of including two damped travelling and different numbers of evanescent modes on the transmission/reflection coefficients, we find the additional effect is small (Fig. 5-3). In fact, including more evanescent modes for viscoelastic model introduces an accumulate error from root finding procedure, which causes fluctuations in the results, in particular the reflection coefficient. This situation is different from what was found from the thin elastic theory, where if we require error $< 0.1\%$, we need to include many evanescent modes [18]. In Fox and Squire, the free-end boundary conditions at the ice edge are matched at a point, while in the present study they are matched over the entire interface.

This finding suggests that more modes are required to approximate the abrupt change of material properties from open water to elastic plate when one point is used then over a finite surface. This situation is analogous to the Gibbs phenomenon, i.e. for a box function to be approximated by Fourier series, the shorter the span the longer the series is required for the same accuracy.

5.6.3 Energy partitions in three modes

As discussed in Wang and Shen [58] and chapter 4 and Fig. 5-5 of the present study, there is a mode switching phenomenon associated with increasing G. That is, at low G one of the three modes for the dispersion relation dominates, as G increases the other mode becomes dominant. This switching occurs when the third mode approaches the other two. In close examination of the nature of these three modes as shown in Fig. 5-2, the two dominant modes are from the simplified dispersion relation Eq. (2.18) and the third is from the remaining terms of Eq. (2.16). Fig. 5-5 and Fig. 5-6 show the partition of energy among these three roots. The third root contains little energy and thus can be dropped from further analysis.

5.6.4 A remark on the difference between pure viscous and pure elastic ice

An interesting and unexpected result is shown in Fig. 5-6. Even for viscous ice with small viscosity the reflection can be significant. For elastic ice, the rigidity has to be relatively high to have the same effect. Hence when we model wave propagation from open water to an ice zone, we need to carefully consider the reflection from viscous ice like grease or brash ice at the edge.

5.7 Conclusions

In conclusion, for practical applications of the viscoelastic model in wave propagation through an ice cover, one can ignore the evanescent modes to save considerable computational time. Of the many other propagating modes, the two from the simplified dispersion relation are sufficient for representing the wave transmission/ reflection. Between the approximate method and the variational method, there is no difference in the computational cost, hence the variational method is preferred to more accurately match the boundary conditions. Finally, we emphasize that further study of the dominant modes in the viscoelastic dispersion is needed. So far, we have found that for pure elastic plates the two modes from the simplified dispersion relation always switch their dominance as G increases. For pure viscous covers this mode switching depends on the water depth. In case of a full viscoelastic material, whether there is mode switching between these two modes depends on the viscosity, the elasticity, and the water depth.

CHAPTER 6 EXPERIMENTAL STUDY

To obtain the viscoelastic parameters from an inverse method, we need to have experimental or field data. The results from previous experiments for grease/pancake ice field show that the grease ice cover followed that of a viscous layer model, but under a pancake ice field it did not. New experimental data are now available for three different types of ice covers: frazil/pancake ice, pancake ice, and fragmented ice. The wave number and attenuation are obtained for several monochromatic waves over a range of frequencies. Using an optimization procedure to inversely determine the model parameters, we obtain the equivalent viscoelastic properties of these ice covers. We show that different ice covers require different parameterization to reflect the observed dispersion. The present results provide information to establish a direct relation between ice morphology and its mechanical parameters.

6.1 Introduction

To parameterize and validate models for the new Arctic Ocean, laboratory experiment provides a much more controlled and less expensive supplement to field studies. The experiment at HSVA in 2008 [99] measured wave propagation through a grease/pancake ice field. The results were compared with a model that assumed ice covers as a pure viscous material. Though this model agreed well with laboratory data taken with a soft grease ice cover under warm temperature [52], it did not agree with the grease/pancake ice cover under cold temperature [100].

In 2013, an experiment was conducted at HSVA again. As part of a larger two-week study entitled “Oil Detection Under Sea Ice” led by Jeremy Wilkinson of the

British Antarctic Survey, tests were performed to measure wave-ice interactions for three different ice covers: frazil/pancake ice, pancake ice, and fragmented ice floes. The experimental data were collected by Chris Callinan and detailed in Callinan et al. [77]. In this chapter, these data are used to illustrate the data processing and the inverse method used to determine the rigidity and viscosity parameters from the measured dispersion data.

6.2 Experiment

In the 2013 HSVA experiment, there were two wave tanks as shown in Fig. 6-1. The majority of the data reported here is from tank 3. Tank 2 was dedicated to other purposes unrelated to the present study. There were occasional cases where waves were propagated in tank 2. These occasional data are also included. Before the experiment, the voltage signals from the pressure sensors in Fig. 6-2 are calibrated with the water elevation. In the following sections the 'raw data' refers to the calibrated water elevation. The water depth in the tank was 0.94m and 0.93m with the nominal depth of all sensors at 0.24m and 0.23m on December 12 and 13, respectively. Three types of ice covers were formed during the experiment: frazil/pancake ice, pancake ice, and fragmented ice, as shown in Fig. 6-3. Detailed information of the facility, the formation of ice and collection of experimental data can be found in an experimental report [77, 101]. Ice thickness and floe size were sampled with a mesh-scoop. This tool was used in all our previously reported experiments [75, 100]. Water was drained from the mesh bottom of the square scoop shown in Fig. 6-4 after inserting the tool sideways through the thickness of the ice cover and gently lifting it off the surface. The thickness of the whole ice cover, which consisted of a slushy bottom layer and one or more pancakes on top (if pancakes were formed), and the diameter of the pancake ice were estimated using the scale on the tool.

Another sampling of the in-situ ice thickness as reported by Smedsrud and Skogseth [102] was also used in the frazil ice stage. This method involved using an open cylinder to puncture through the ice cover vertically, then plugging the submerged end and lifting the cylinder off the wave tank. The ice thickness floating on top of water in the cylinder was then estimated using the scale on the cylinder wall. After pancakes formed the in-situ measurement was stopped due to its difficulty of puncturing the relatively rigid ice cover. Using the 2008 data from both methods, we determine that the drained thickness using the mesh-scoop was about 2/3 that of the un-drained values using the cylinder.

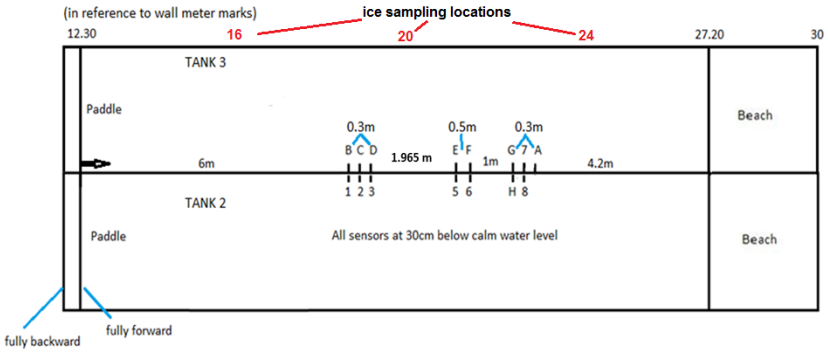

Fig. 6-1 Basin configuration and pressure transducer locations.

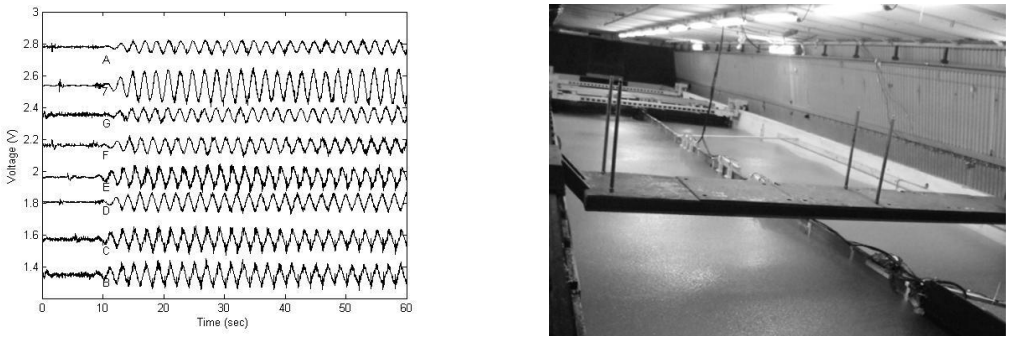

Fig. 6-2 (Left) Sample time series in voltage. All data are displaced to aid visualization. (Right) the first frazil/pancake ice cover tested. Wave in tank 3 is visible.

The three types of ice covers shown in Fig. 6-3 are named: test 1 for the frazil/pancake ice, test 2 the pancake ice, and test 3 the fragmented ice. Within each test, the frequencies used were roughly from 0.5 to 1.1 Hz. At each frequency we repeat the test run at least once. Under some ice conditions, high frequency waves were damped significantly before they reached the sensors hence no measurements were obtained. We used a stop-go procedure to avoid the reflected wave from the beach. Only the first part of the time series shortly after the arrival of the waves at the sensor locations was utilized. The sampling frequency was 100Hz, and each wave run was 60s, starting from the quiescent condition. Each run was followed by a 2min resting period. A longer rest period was impractical and unnecessary. The sensors registered mainly noise after this period.

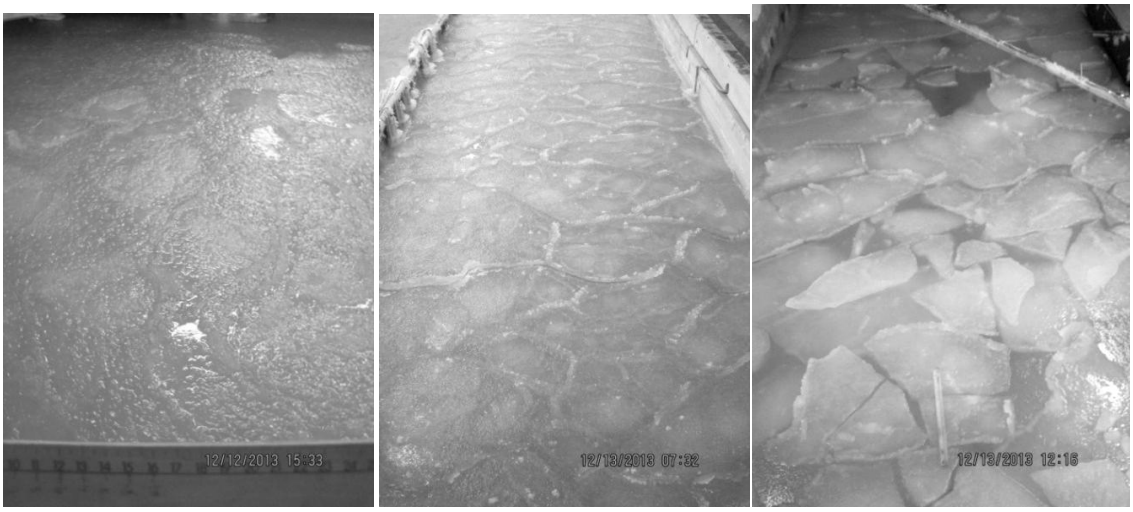

Fig. 6-3 (Left) Frazil/pancake ice mixture with a meter stick shown at the bottom of the photo. (Center) Pancake ice. (Right) Fragmented ice floe.

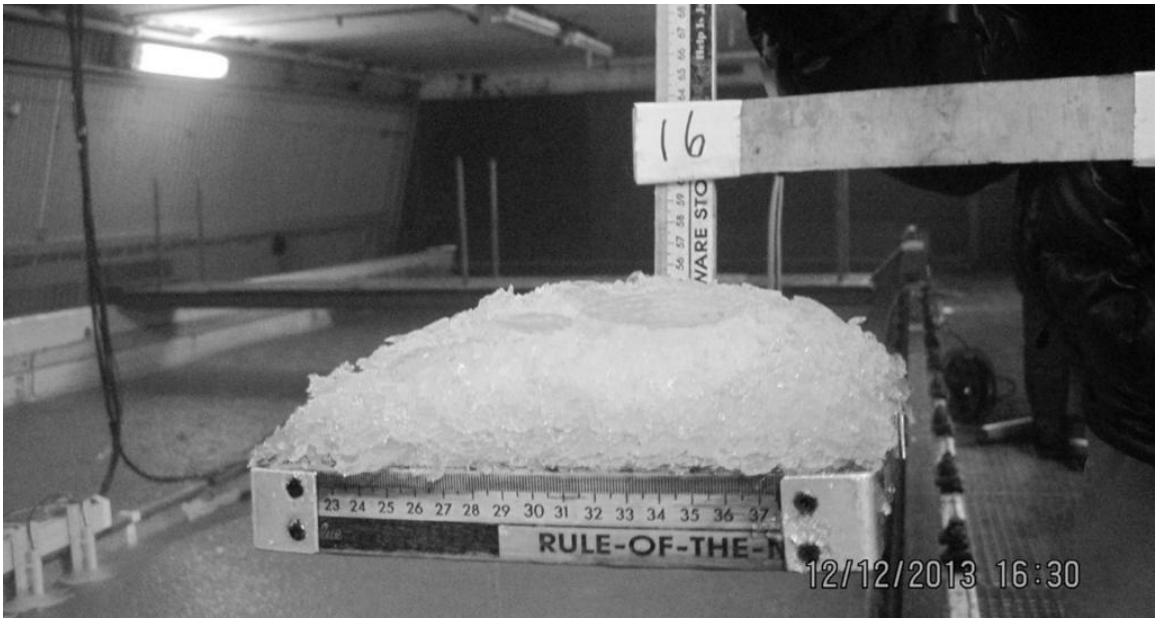

Fig. 6-4 Mesh-scoop ice sampling. One pancake is shown lying on top of the slushy ice accumulation. The stick label shows the sample is picked up at the 16m mark location along the tank.

6.3 Data processing

We first apply an eleven point running average filter to the raw data. To avoid phase-shift, the average is centered at each point. The filter width is 0.1s, corresponding to a low pass filter of 10Hz cutoff. Hence it removes noise from equipment and the environment, but preserves all wave signals. We will use one run corresponding to a 0.5Hz wave from the second test to illustrate the procedure used to determine the wave characteristics.

6.3.1 Wave Frequency

Since beach reflection does not change the wave frequency, any portion of the time series after the arrival of a wave at any sensor could be used to determine frequency.

As shown in Fig. 6-5, a 5s range is selected to start from the beginning of the wave signal at each sensor. In Wang and Shen [100], they employed four estimators to determine the wave frequency and found the differences among the methods were negligible. We use one of the four: the discrete Fourier transform (DFT) to convert the time series $s(n)$ to its Fourier components $S(f)$.

$$S(f) = \frac{1}{L}\sum_{n=1}^{M} s(n)\exp(-2\pi i f t_n)\frac{L}{M} = \frac{1}{M}\sum_{n=1}^{M} s(n)\exp\left(-2\pi i f n L/M\right), t_n = \frac{nL}{M} \tag{6.1}$$

Here, L and M are the length and total number of the selected time series, f is frequency. The energy spectrum is

$$E(f) = S(f)S^*(f) \tag{6.2}$$

The peak of the energy spectrum corresponds to the wave frequency. Figure 6 shows that the frequency for this data set is at 0.502 ± 0.0024Hz from all sensors.

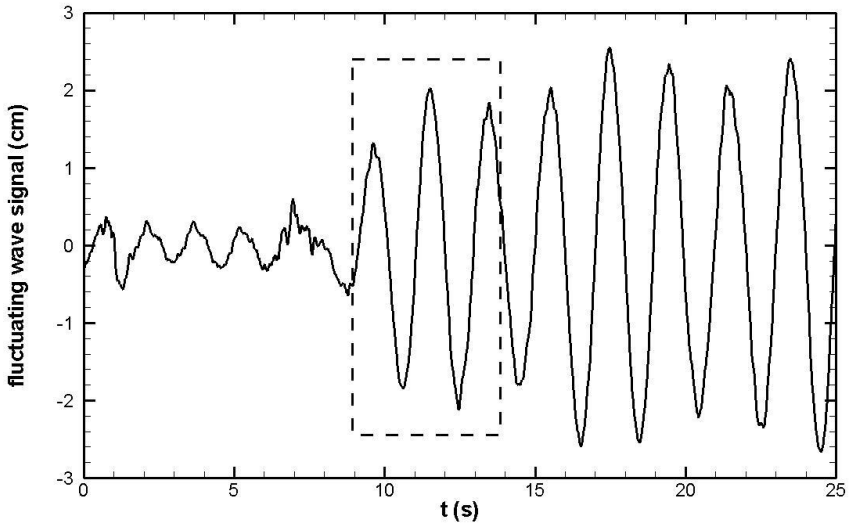

Fig. 6-5 Selected range of the wave signal at sensor B for analysis.

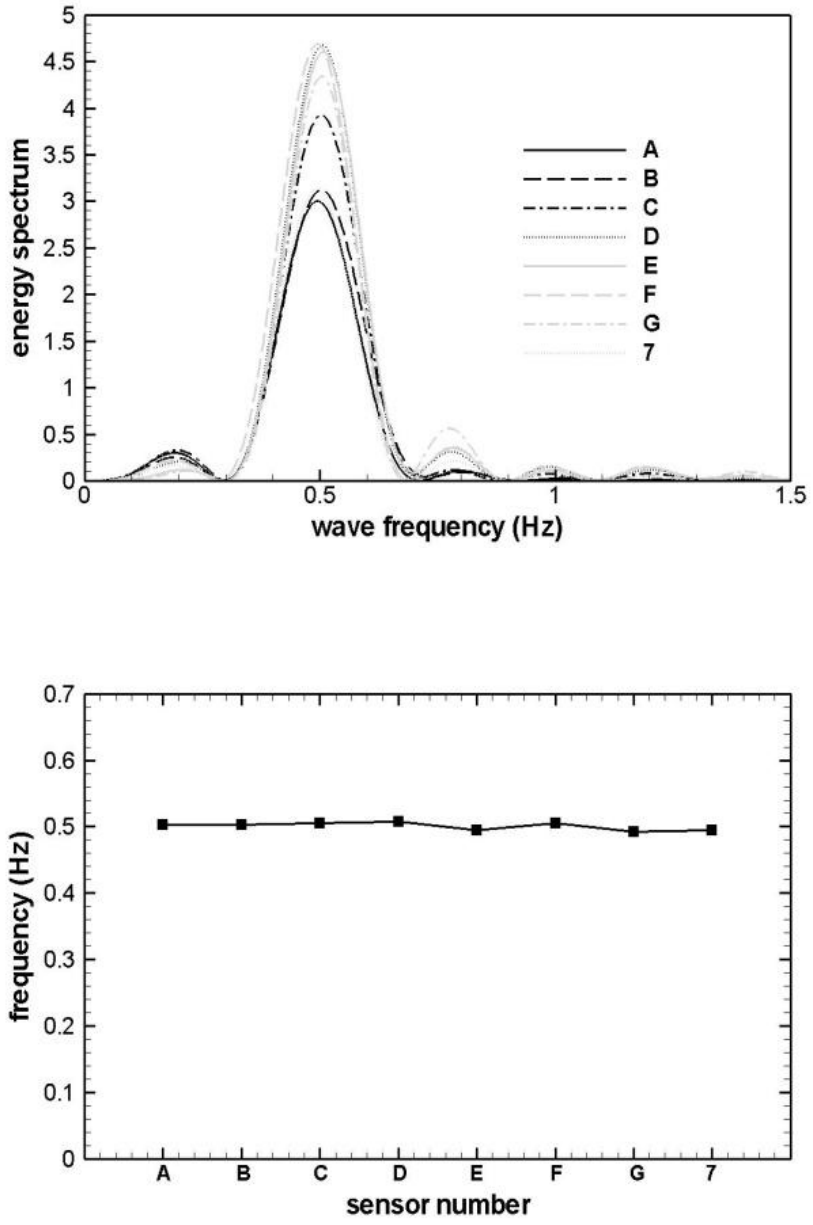

Fig. 6-6 (a) The energy spectrum and (b) the frequency of the wave signal.

6.3.2 Wave Number

The wave number k_r is determined from measuring the celerity c and relating it to the angular frequency $\omega = 2\pi f$ as follows:

$$c = \frac{\Delta l}{\Delta t},\ k_r = \frac{\omega}{c} \tag{6.3}$$

Here, Δl is the distance between a chosen pair of sensors and Δt is the time lag of the signal between this pair of sensors. The distances between sensors are given in Fig. 6-1. To obtain the time lag, we maximize the time correlation between two time series obtained at sensors m, n:

$$C(\Delta t) = \int_0^L s_m(t) s_n(t + \Delta t) dt \tag{6.4}$$

Here $L = 5s$, and the starting point for sensor m is at the first trough after the arrival of the wave. Figure 6-7(a) shows $C(\Delta t)$ between three pairs of sensors. The resulting celerity between different pairs of sensors is given in Fig. 6-7(b). The mean and standard deviation of the celerity for this run is 2.63 ± 0.22m/s. From Eq. (3), the resulting wave number is 1.20 ± 0.10m-1. The first pair for sensor B and C is expected to be the most accurate due to the strength of the signals. Celerity from this pair is used for the subsequent calculations.

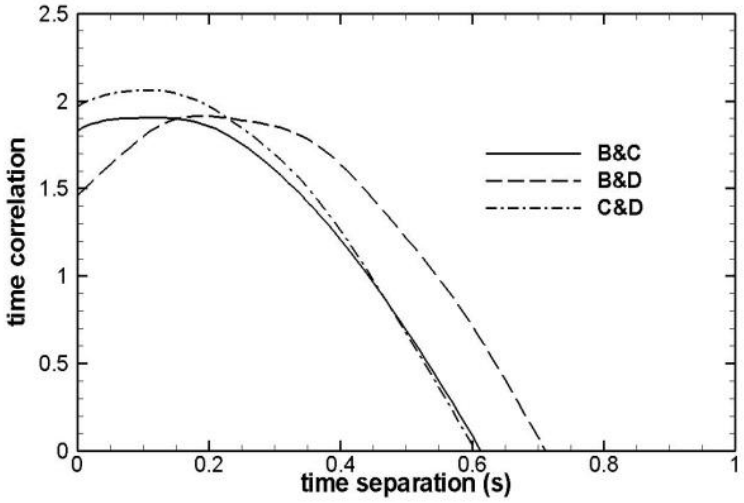

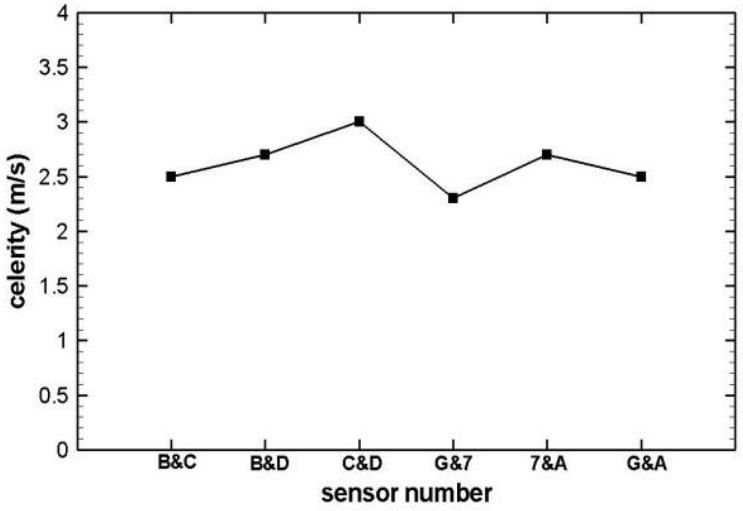

Fig. 6-7 (a) The time correlation and (b) the celerity between two sensors.

6.3.3 Wave Amplitude

To calculate the wave amplitude at each location, in the present study we use the DFT method again. As before, we select a 5s portion after the arrival of the wave to calculate the amplitude for each sensor. The starting point of this 5s period for the leading sensor, B, is set at the first trough after the arrival of the wave. For each subsequent sensor it is based on the group velocity estimated using the open water condition. This is a conservative estimate since the true group velocity is in fact larger, as shown in the measured c. The amplitude of the wave is

$$a' = \sqrt{E(f_p)df} \ . \tag{6.5}$$

We tested the sensitivity of the amplitude results with respect to different processing method by using the Butterworth and Spectrum functions in Matlab. We applied a 3rd order filter with [0.02, 1.25] Hz window to the raw data as adopted in Wang and Shen [100]. The estimated wave amplitudes are very close to each other. For example at B for

this run the Matlab spectrum function with the more aggressive filter yields 1.89cm and the DFT method yields 1.95cm.

6.3.4 Wave Attenuation

For the wave attenuation calculation we assume that the wave has an exponential decay along the propagation direction. In Wang and Shen [100], three pairs of sensors were used to calculate the attenuation coefficient. In this study, during calibration we found that sensor A was not reliable, hence deleted from the data analysis. The attenuation is thus estimated as

$$k_i = \frac{\ln\left(\frac{a_G a_7}{a_B a_C}\right)}{2l}, \tag{6.6}$$

where $a's$ represent amplitudes at the respective sensor locations and l is the distance between the center of sensor group G, 7 and B, C. We calculate the wave attenuation to be 0.0373m^{-1} for this run.

6.3.5 Inverse Method for Estimation on Viscosity and Shear Modulus

Substituting Eq. (2.17) into (2.18), the viscoelastic sea ice model we will try to parameterize using the present experimental data is shown below.

$$\omega^2 = \left(1 + \frac{\rho_{ice}}{\rho_{water}} \frac{g^2 k^2 S_k S_\alpha - (N'^4 + 16k^6\alpha^2\nu_e^4) S_k S_\alpha - 8k^3\alpha\nu_e^2 N'^2 (C_\alpha C_k - 1)}{gk(4k^3\alpha\nu_e^2 S_k C_\alpha + N'^2 S_\alpha C_k - gk S_k S_\alpha)}\right) gk \tanh kH \tag{6.7}$$

$$\nu_e = \nu + iG/\rho_{ice}\omega,\ \alpha^2 = k^2 - i\omega/\nu_e$$

where $S_k = \sinh kh$, $S_\alpha = \sinh \alpha h$, $C_k = \cosh kh$, $C_\alpha = \cosh \alpha h$, $N' = \omega + 2ik^2\nu_e$, h is the ice thickness, and H is the water depth. The complex wave number is $k = k_r + ik_i$ where k_r is related to the wave phase speed and k_i is the attenuation coefficient. The equivalent mechanical properties of the ice cover are: ν the effective viscosity, and G the effective shear modulus. To determine ν and G for this example case where the measured complex wave number is $k = k_r + ik_i = 1.20 + i0.0373\text{m}^{-1}$, we substitute the laboratory data $h = 0.02\text{m}$, $H = 0.94\text{m}$, $\omega = 3.14\text{Hz}$, $\rho_{ice} = 917\text{kg/m}^3$, and $\rho_{water} = 1032\text{kg/m}^3$ into Eq. (6.7) and plot the contours of the residual defined as the difference between the left and right side of Eq. (6.7). There are three roots for the estimated ν and G which correspond to the measured wave number k_r and the attenuation k_i. Mathematically, all roots are acceptable since they produce the same observed wave characteristics. However, only the second root is physically consistent with ice properties: the first test should have the lowest and the third the highest shear modulus. Hence in all inverse solutions this root was chosen for all cases.

6.4 Results

6.4.1 Wave Number and Attenuation

The wave number k_r and attenuation k_i are dependent on the wave frequency. These results are shown in Fig. 6-8 and Fig. 6-9, respectively. The dependency is different for different ice covers. For wave number, the first test is closer to open water due to the very thin and soft ice cover. For the second test, the wave number becomes smaller than open water for $f > 0.8\text{Hz}$. In the third test with fragmented floes, the wave

number is clearly much smaller than other cases. The attenuation results show increasing trends with frequency in all three tests. From Fig. 6-9, it is obvious that both ice thickness and ice type affect damping. The ice cover in Wang and Shen [100] was very similar to the first test, but the thickness was similar to the third test show in Table 1.

Wave/Ice Parameters	Frazil/Pancake Ice	Pancake Ice	Fragmented Ice	Wang and Shen [96]
Ice Thickness (cm)	2.5	4	7.5	8.5
Ice Diameter (cm)	2	2.5	20	20

Table 6-1. The comparison on ice parameters among different ice covers.

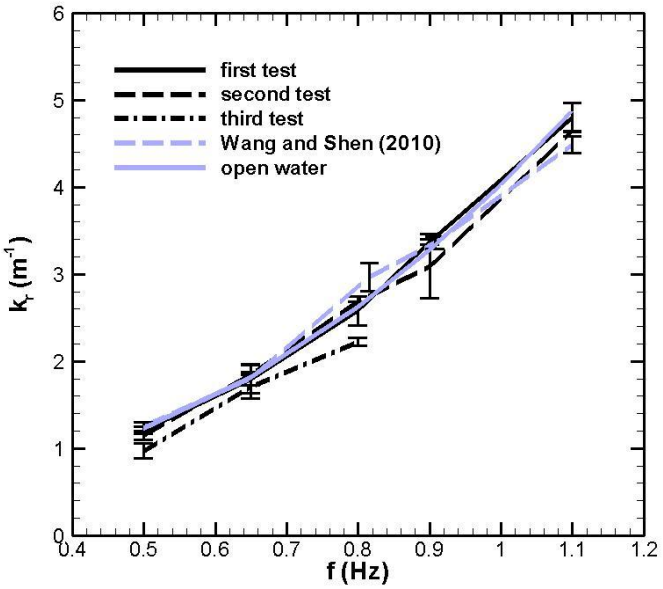

Fig. 6-8 Wave number with respect to wave frequency.

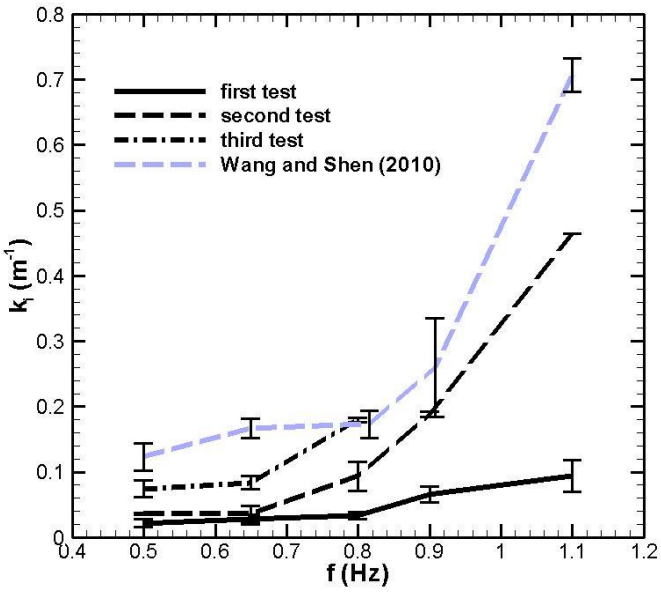

Fig. 6-9 Wave attenuation with respect to wave frequency.

6.4.2 Viscosity and Shear Modulus

We now use the method shown in section 6.3 to inversely determine the viscosity and the shear modulus for different ice covers. There are two purposes for this calculation. First, we need to examine if the viscoelastic model could simulate these different ice conditions. The other is to establish a direct relation between ice morphology and its mechanical parameters. This relation is important for further application of viscoelastic model in ocean wave models. Based on the mean wave number and attenuation results in Fig. 6-8 and Fig. 6-9, we inversely calculate the viscosity and the shear modulus for each test case and different wave frequency as shown in Fig. 6-10 and Fig. 6-11.

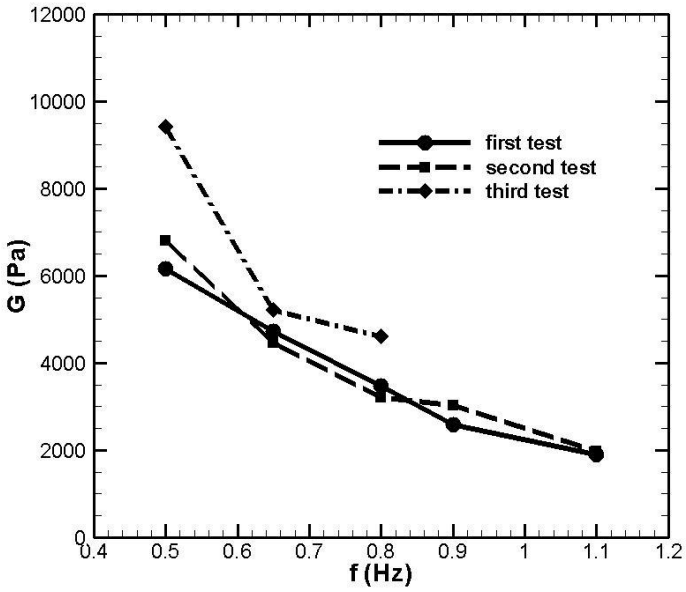

Fig. 6-10 Effective shear modulus with respect to wave frequency by inverse method.

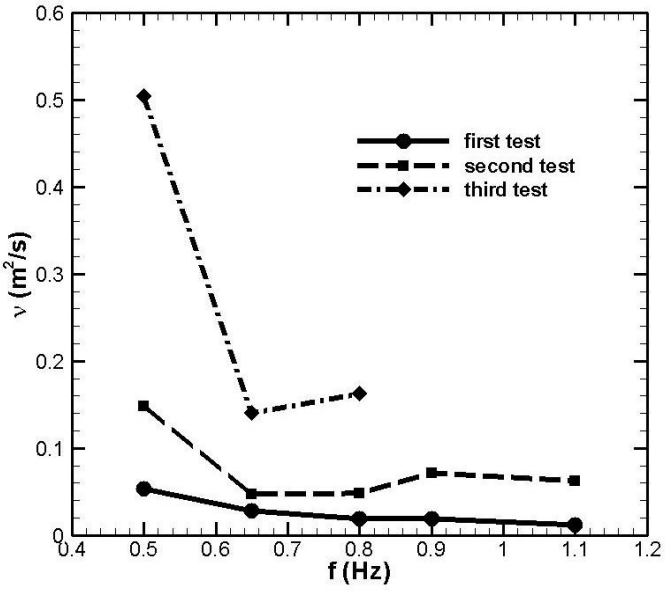

Fig. 6-11 Effective viscosity with respect to wave frequency by inverse method.

Although with these results the calculated (G , ν) precisely reproduce the measured (k_r, k_i), frequency dependent (G, ν) is impractical for applications. It is much more desirable to have a direct relationship between a given ice morphology and its equivalent mechanical properties. We thus look for a best fit (G , ν) pair to each of the ice covers for the whole range of frequencies tested. This is done with the Levenberg–Marquardt algorithm. We minimize the overall error defined as the following

$$\varepsilon = \sum_{n=1}^{N} \left(k_r - k_r^n\right)^2 + \left(k_i - k_i^n\right)^2$$

Here k_r^n and k_i^n are measured wave number and attenuation and k_r , k_i are the calculated values corresponding to a (G , ν) pair . The results are shown in Fig.6-12-Fig.6-15. The wave number is better fitted than the attenuation.

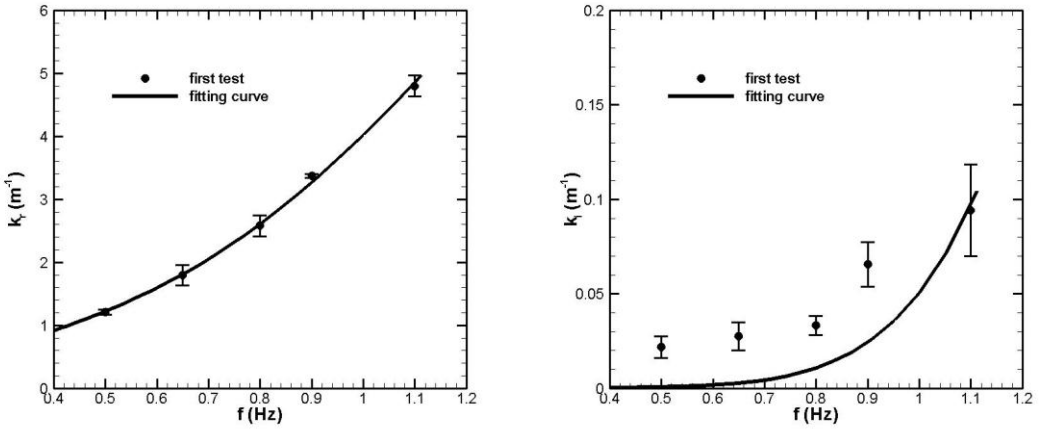

Fig. 6-12 Data fitting by viscoelastic model for the first test using Levenberg–Marquardt algorithm (LMA). $G = 21\text{Pa}$; $\nu = 0.014\text{m}^2/\text{s}$.

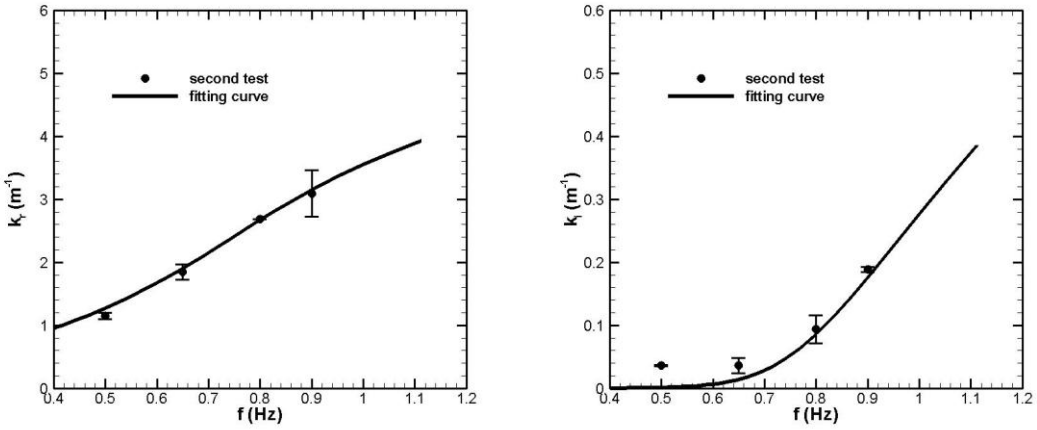

Fig. 6-13 Data fitting by viscoelastic model for the second test using Levenberg–Marquardt algorithm (LMA). $G = 5.1\times10^{5}\,\mathrm{Pa}$; $\nu = 61.1\mathrm{m}^2/\mathrm{s}$.

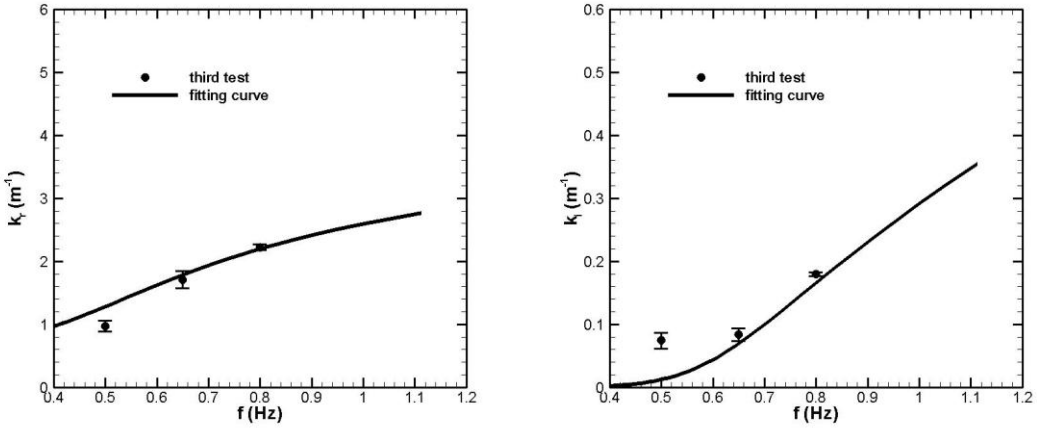

Fig. 6-14 Data fitting by viscoelastic model for the third test using Levenberg–Marquardt algorithm (LMA). $G = 1.0\times10^{6}\,\mathrm{Pa}$; $\nu = 139.3\mathrm{m}^2/\mathrm{s}$.

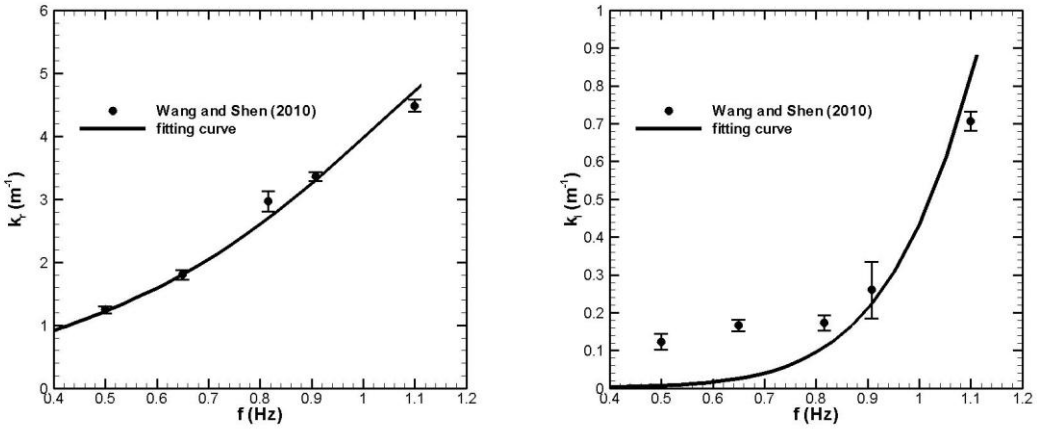

Fig. 6-15 Data fitting by viscoelastic model for Wang and Shen (2010a) using Levenberg–Marquardt algorithm (LMA). $G = 48.24\text{Pa}$; $\nu = 0.04\text{m}^2/\text{s}$.

6.5 Discussions

There are several observations from the present study. First it is reconfirmed that the type of ice cover does affect its dispersion behavior. Frazil/pancake ice covers do not change the wave numbers as much as the fragmented ice. Attenuation is strongly dependent on ice cover thickness and the type of ice. Which of the two is the dominant factor is difficult to conclude with the limited data. Rigidity is an important parameter to include for ice covers except the soft grease ice. For this HSVA experiment, due to the continuous cooling throughout the tests, in addition to growing thickness, the surface of the ice became harder as its temperature dropped. An infrared camera was in the plan for the oil detection part of the experiment but it was not operational in time for the reported tests. Even though there is no sufficient knowledge to relate the ice surface temperature to its mechanical properties, with the coldness of the ice cover we might be better

informed of their physical rigidity. Direct mechanical measurements of the viscoelastic properties of the ice covers, such as the vibrational tests or creep tests, have been performed for consolidated ice sheets [103]. For the present types of ice such tests are not possible.

Concerning the inverse method and the resulting viscoelastic parameters, the frequency by frequency results match precisely the measured wave data. Due to potential experimental uncertainties from many sources, including the environment and the sensor performance, variance of the inversely determined (G, ν) is expected. However, the trend is probably robust. For application purpose, frequency by frequency (G, ν) is not practical at least for the time being. What we need is a direct relationship between the measurable ice characteristics, such as the type of ice and the cover thickness, and its equivalent mechanical properties. Using an optimization procedure we thus determined (G, ν) for the three types of ice covers. The results are reasonable because the rigidity increased as the ice cover evolved from the frazil/pancake stage to pancakes and finally to the most rigid fragmented floes. The viscosity parameter also increased simultaneously. The same method is used to test the previous data from Wang and Shen [96] which had an ice cover type very similar to test 1 but with very different ice cover thickness. The resulting (G, ν) are nearly identical to the present values. Viscosity is a phenomenological parameter that embraces all rate dependent damping mechanisms. The underlying assumption of the current model shown in Eq. (6.7) is that these mechanisms are all linearly dependent on the rate of deformation, which is subject to further scrutiny. Nonetheless, before more realistic theories are developed, the viscoelastic model does a reasonable job fitting the measured data and providing estimates for the mechanical

properties for three types of ice cover. The only consistent discrepancy between the viscoelastic model and the measured data is the damping at lower frequencies. We did try to change the objective function defined in Eq. (6.8) by weighting the k_i term more. However, by increasing the weight of the error from k_i the fit for k_r becomes worse while k_i is still consistently underestimated.

Another phenomenon worth noting is that in processing the data, we found that fragmented ice cover behaved very differently from the frazil/pancake ice covers. Even though higher frequency runs were made, wave speed and attenuation calculations were not feasible. The wave energy at the paddle frequency decayed over very short distance. We compare the surface elevation signal at sensor B for the first test and the third test. For the first test, clear wave form with a single frequency lasts for the whole duration. But for the third test, the wave becomes random like from the beginning with multiple frequencies. Visual observations suggest that wave scattering and ice collision may have influenced the wave condition in the third test. The high frequency wave data from the third test is too weak for reliable estimates.

From the curve-fitting results, the under predictions from viscoelastic model for attenuation at long wave shows that the current wave ice interaction model still misses some important mechanism to damp the wave energy. The possible sources for such damping may be the wave scattering by ice floes or the nonlinear interaction among different wave numbers.

6.6 Conclusions

In summary, we tested three different types of ice covers: frazil/pancake ice, pancake ice, and fragmented ice over a range of wave frequencies. The wave number and

attenuation are obtained for each wave frequency. Using an inverse method, we obtain the equivalent viscoelastic properties of different ice covers under different wave frequencies. A least square fitting method is used to inversely determine viscosity and shear modulus for each ice condition. The viscoelastic model did a reasonable job simulating the three different ice covers. The frazil pancake ice is shown to have the least equivalent elasticity and viscosity. The fragmented ice cover has the highest equivalent elasticity and viscosity. The pancake ice cover lies in between the two. The present study provides useful information to establish a direct relationship between ice morphology and the mechanical parameters of the ice cover. Appropriate scaling analysis needs to be developed to extrapolate the laboratory results to field conditions.

CHAPTER 7 GOVERNING EQUATIONS OF WAVE SCATTERING

In this chapter, we derive the governing equations for wave scatterings with the Eddington approximation or diffusion approximation. The advantage of such approximation is to avoid calculating the complex integral kernel in the integral-differential equation of the wave action density function. The diffusion approximation, or the Eddington approximation, is commonly used in the radiation transfer problem in a random medium. With three-term decomposition for the wave action density function, we obtain three differential equations for the wave action density. To evaluate the scattering coefficient, we employ a statistical method to get consistent results with previous scattering theories.

7.1 Decomposition of wave action density function

Recall that the wave energy balance equation is

$$\frac{\partial}{\partial t}N+\frac{\partial}{\partial x}\dot{x}N+\frac{\partial}{\partial y}\dot{y}N+\frac{\partial}{\partial k}\dot{k}N+\frac{\partial}{\partial \theta}\dot{\theta}N=\frac{S}{\omega} \tag{2.1}$$

If we ignore all other processes and focus on the scattering process alone, the above equation becomes [104, 105],

$$\begin{aligned}&\frac{\partial}{\partial t}N(\mathbf{x},t,k,\theta)+c_g\theta\cdot\nabla N(\mathbf{x},t,k,\theta)=-c_g\alpha_s(\mathbf{x},t,k,\theta)N(\mathbf{x},t,k,\theta)\\&+c_g\int_0^{2\pi}S_k(\mathbf{x},t,k,\theta,\theta')N(\mathbf{x},t,k,\theta')d\theta'\end{aligned} \tag{7.1}$$

Here, α_s is scattering attenuation, c_g is the group velocity, and S_k is the kernel of wave energy redistribution. The right hand side of the above is the conservative wave source term mentioned in Chapter 2 :

$$S_{ice,c} = -c_g \alpha_s(\mathbf{x},t,k,\theta) N(\mathbf{x},t,k,\theta) + c_g \int_0^{2\pi} S_k(\mathbf{x},t,k,\theta,\theta') N(\mathbf{x},t,k,\theta') d\theta' \qquad (7.2)$$

The energy conservation condition leads to

$$\alpha_s(\mathbf{x},t,k,\theta) = \int_0^{2\pi} S_k(\mathbf{x},t,k,\theta',\theta) d\theta' \qquad (7.3)$$

Thus, the redistribution of energy is exactly the loss of energy in the given wave direction. Now, we linearly decompose the wave action density function into two parts as the following,

$$N(\mathbf{x},t,k,\theta) = A(\mathbf{x},t,k,\theta) + B(\mathbf{x},t,k,\theta) \qquad (7.4)$$

$A(\mathbf{x},t,k,\theta)$ is the incident part or the transmitted part, and $B(\mathbf{x},t,k,\theta)$ is the scattered part or the reflected part. The governing equations for these two parts are as the following,

$$\frac{\partial}{\partial t} A(\mathbf{x},t,k,\theta) + c_g \theta \cdot \nabla A(\mathbf{x},t,k,\theta) = -c_g \alpha_s(\mathbf{x},t,k,\theta) A(\mathbf{x},t,k,\theta) \qquad (7.5)$$

$$\begin{aligned} &\frac{\partial}{\partial t} B(\mathbf{x},t,k,\theta) + c_g \theta \cdot \nabla B(\mathbf{x},t,k,\theta) = -c_g \alpha_s(\mathbf{x},t,k,\theta) B(\mathbf{x},t,k,\theta) \\ &+ c_g \int_0^{2\pi} S_k(\mathbf{x},t,k,\theta,\theta') B(\mathbf{x},t,k,\theta') d\theta' + c_g \int_0^{2\pi} S_k(\mathbf{x},t,k,\theta,\theta') A(\mathbf{x},t,k,\theta') d\theta' \end{aligned} \qquad (7.6)$$

Then, we decompose B with directional average part and fluctuating part as the following,

$$B(\mathbf{x},t,k,\theta) = \overline{B}(\mathbf{x},t,k) + B'(\mathbf{x},t,k,\theta) \qquad (7.7)$$

$$\overline{B}(\mathbf{x},t,k) = \frac{1}{2\pi} \int_0^{2\pi} B(\mathbf{x},t,k,\theta) d\theta \qquad (7.8)$$

Using Eddington approximation in radiative transfer [104, 105], we have

$$B'(\mathbf{x},t,k,\theta) = -\frac{1}{\alpha_s} \theta \cdot \nabla \overline{B}(\mathbf{x},t,k) \qquad (7.9)$$

7.2 Derivations of governing equations

To obtain the governing equation of $\overline{B}(\mathbf{x},t,k)$, we take the directional average of the equation of $B(\mathbf{x},t,k,\theta)$ which yields

$$\begin{aligned}&\frac{\partial}{\partial t}\overline{B}(\mathbf{x},t,k)+c_g\frac{1}{2\pi}\int_0^{2\pi}\theta\cdot\nabla B(\mathbf{x},t,k,\theta)d\theta=\\&-c_g\frac{1}{2\pi}\int_0^{2\pi}\alpha_s(\mathbf{x},t,k,\theta)B(\mathbf{x},t,k,\theta)d\theta+c_g\frac{1}{2\pi}\int_0^{2\pi}\int_0^{2\pi}S_k(\mathbf{x},t,k,\theta,\theta')d\theta B(\mathbf{x},t,k,\theta')d\theta'\\&+c_g\frac{1}{2\pi}\int_0^{2\pi}\int_0^{2\pi}S_k(\mathbf{x},t,k,\theta,\theta')d\theta A(\mathbf{x},t,k,\theta')d\theta'\end{aligned} \tag{7.10}$$

Using the energy conservation condition Eqn. (7.3), we obtain

$$\begin{aligned}&\frac{\partial}{\partial t}\overline{B}(\mathbf{x},t,k)+c_g\frac{1}{2\pi}\int_0^{2\pi}\theta\cdot\nabla B(\mathbf{x},t,k,\theta)d\theta=\\&-c_g\frac{1}{2\pi}\int_0^{2\pi}\alpha_s(\mathbf{x},t,k,\theta)B(\mathbf{x},t,k,\theta)d\theta+c_g\frac{1}{2\pi}\int_0^{2\pi}\alpha_s(\mathbf{x},t,k,\theta')B(\mathbf{x},t,k,\theta')d\theta'\\&+c_g\frac{1}{2\pi}\int_0^{2\pi}\alpha_s(\mathbf{x},t,k,\theta')A(\mathbf{x},t,k,\theta')d\theta'\end{aligned} \tag{7.11}$$

Eliminating the first and second terms on the right hand side of the above equation, we get

$$\frac{\partial}{\partial t}\overline{B}(\mathbf{x},t,k)+c_g\frac{1}{2\pi}\int_0^{2\pi}\theta\cdot\nabla B(\mathbf{x},t,k,\theta)d\theta=c_g\frac{1}{2\pi}\int_0^{2\pi}\alpha_s(\mathbf{x},t,k,\theta')A(\mathbf{x},t,k,\theta')d\theta' \tag{7.12}$$

For the second term of the left hand side in the above equation, we substitute equations (7.7) and (7.9).

$$\begin{aligned}&\frac{1}{2\pi}\int_0^{2\pi}\theta\cdot\nabla B(\mathbf{x},t,k,\theta)d\theta=\frac{1}{2\pi}\left(\int_0^{2\pi}\cos\theta d\theta+\int_0^{2\pi}\sin\theta d\theta\right)\frac{\partial}{\partial x}\overline{B}(\mathbf{x},t,k)\\&-\frac{1}{2\pi}\int_0^{2\pi}\theta\cdot\nabla\frac{1}{\alpha_s}\theta\cdot\nabla\overline{B}(\mathbf{x},t,k)d\theta\end{aligned} \tag{7.13}$$

The first term of the right hand side in the above equation equals to zero.

$$\frac{1}{2\pi}\int_0^{2\pi}\theta\cdot\nabla B(\mathbf{x},t,k,\theta)d\theta=-\frac{1}{2\pi}\int_0^{2\pi}\theta\cdot\nabla\frac{1}{\alpha_s}\theta\cdot\nabla\overline{B}(\mathbf{x},t,k)d\theta \tag{7.14}$$

Then we have

$$\begin{aligned}&\frac{1}{2\pi}\int_0^{2\pi}\theta\cdot\nabla\frac{1}{\alpha_s}\theta\cdot\nabla\overline{B}(\mathbf{x},t,k)d\theta=\\&\frac{1}{2\pi}\int_0^{2\pi}\cos\theta\frac{\partial}{\partial x}\left(\frac{1}{\alpha_s}\left(\cos\theta\frac{\partial}{\partial x}\overline{B}(\mathbf{x},t,k)+\sin\theta\frac{\partial}{\partial x}\overline{B}(\mathbf{x},t,k)\right)\right)d\theta\\&+\frac{1}{2\pi}\int_0^{2\pi}\sin\theta\frac{\partial}{\partial x}\left(\frac{1}{\alpha_s}\left(\cos\theta\frac{\partial}{\partial x}\overline{B}(\mathbf{x},t,k)+\sin\theta\frac{\partial}{\partial x}\overline{B}(\mathbf{x},t,k)\right)\right)d\theta\end{aligned} \tag{7.15}$$

If the scattering attenuation is isotropic, we can rewrite the equation as the following

$$\begin{aligned}&\frac{1}{2\pi}\int_0^{2\pi}\theta\cdot\nabla\frac{1}{\alpha_s}\theta\cdot\nabla\overline{B}(\mathbf{x},t,k)d\theta=\\&\frac{1}{2\pi}\int_0^{2\pi}\cos^2\theta d\theta\frac{\partial}{\partial x}\left(\frac{1}{\alpha_s}\frac{\partial}{\partial x}\overline{B}(\mathbf{x},t,k)\right)+\frac{1}{2\pi}\int_0^{2\pi}\sin^2\theta d\theta\frac{\partial}{\partial y}\left(\frac{1}{\alpha_s}\frac{\partial}{\partial y}\overline{B}(\mathbf{x},t,k)\right)\end{aligned} \tag{7.16}$$

This directly leads to

$$\frac{1}{2\pi}\int_0^{2\pi}\theta\cdot\nabla\frac{1}{\alpha_s}\theta\cdot\nabla\overline{B}(\mathbf{x},t,k)d\theta=\frac{1}{2}\frac{\partial}{\partial x}\left(\frac{1}{\alpha_s}\frac{\partial}{\partial x}\overline{B}(\mathbf{x},t,k)\right)+\frac{1}{2}\frac{\partial}{\partial y}\left(\frac{1}{\alpha_s}\frac{\partial}{\partial y}\overline{B}(\mathbf{x},t,k)\right) \tag{7.17}$$

$$\frac{1}{2\pi}\int_0^{2\pi}\theta\cdot\nabla\frac{1}{\alpha_s}\theta\cdot\nabla\overline{B}(\mathbf{x},t,k)d\theta=\nabla\cdot D(\mathbf{x},t,k)\nabla\overline{B}(\mathbf{x},t,k) \tag{7.18}$$

Here, the diffusion coefficient is defined as

$$D(\mathbf{x},t,k)=\frac{1}{2\alpha_s(\mathbf{x},t,k)} \tag{7.19}$$

If the scattering attenuation is anisotropic, we have the diffusion coefficient tensor as the following

$$\mathbf{D}(\mathbf{x},t,k)=\frac{1}{2}\begin{bmatrix}\int_0^{2\pi}\cos^2\theta/2\pi\alpha_s(\mathbf{x},t,k,\theta)d\theta & \int_0^{2\pi}\cos\theta\sin\theta/2\pi\alpha_s(\mathbf{x},t,k,\theta)d\theta\\ \int_0^{2\pi}\cos\theta\sin\theta/2\pi\alpha_s(\mathbf{x},t,k,\theta)d\theta & \int_0^{2\pi}\sin^2\theta/2\pi\alpha_s(\mathbf{x},t,k,\theta)d\theta\end{bmatrix} \tag{7.20}$$

$$\frac{1}{2\pi}\int_0^{2\pi}\theta\cdot\nabla\frac{1}{\alpha_s}\theta\cdot\nabla\overline{B}(\mathbf{x},t,k)d\theta=\nabla\cdot\mathbf{D}(\mathbf{x},t,k)\cdot\nabla\overline{B}(\mathbf{x},t,k) \tag{7.21}$$

Substituting the above equation into Eq. (7.12), we get

$$\frac{\partial}{\partial t}\overline{B}(\mathbf{x},t,k)=\nabla\cdot\mathbf{D}(\mathbf{x},t,k)\cdot\nabla\overline{B}(\mathbf{x},t,k)+c_g\frac{1}{2\pi}\int_0^{2\pi}\alpha_s(\mathbf{x},t,k,\theta')A(\mathbf{x},t,k,\theta')d\theta' \tag{7.22}$$

In summary, we obtain the governing equations for energy density function as the followings,

$$N(\mathbf{x},t,k,\theta)=A(\mathbf{x},t,k,\theta)+\overline{B}(\mathbf{x},t,k)+B'(\mathbf{x},t,k,\theta) \tag{7.23}$$

$$\frac{\partial}{\partial t}A(\mathbf{x},t,k,\theta)+c_g\theta\cdot\nabla A(\mathbf{x},t,k,\theta)=-c_g\alpha_s(\mathbf{x},t,k,\theta)A(\mathbf{x},t,k,\theta) \tag{7.24}$$

$$\frac{\partial}{\partial t}\overline{B}(\mathbf{x},t,k)=\nabla\cdot\mathbf{D}(\mathbf{x},t,k)\cdot\nabla\overline{B}(\mathbf{x},t,k)+c_g\frac{1}{2\pi}\int_0^{2\pi}\alpha_s(\mathbf{x},t,k,\theta')A(\mathbf{x},t,k,\theta')d\theta' \tag{7.25}$$

$$B'(\mathbf{x},t,k,\theta)=-\frac{1}{\alpha_s}\theta\cdot\nabla\overline{B}(\mathbf{x},t,k) \tag{7.26}$$

7.3 Evaluation of scattering attenuation

Now, we need to evaluate the scattering attenuation coefficient α_s. Because there is no well defined differential equation for one wave reflection event, we use the discrete version for the evolution equation of the wave action density function.

$$A(\mathbf{x},t+\Delta t,k,\theta)-A(\mathbf{x},t,k,\theta)=-c_g\theta\cdot\nabla A(\mathbf{x},t,k,\theta)\Delta t-r(\mathbf{x},t,k,\theta)A(\mathbf{x},t,k,\theta) \tag{7.27}$$

Here, $r(\mathbf{x},t,k,\theta)=R^2(\mathbf{x},t,k,\theta)$ is a random value for randomly distribted ice floe field, and $R(\mathbf{x},t,k,\theta)$ is the wave reflection coefficient. This equation assumes that in Δt there is only one wave reflection event. But if the time step Δt is large, we have $M(\mathbf{x},t,k,\theta,\Delta t)$ wave reflection events. Thus, the energy loss from wave reflection can be expressed as the following

$$\Delta A(\mathbf{x},t,k,\theta) = -\sum_{i=1}^{M} r(1-r)^{i-1} A(\mathbf{x},t,k,\theta) = -\left(1-(1-r)^{M}\right)A(\mathbf{x},t,k,\theta) \qquad (7.28)$$

Here, $M(\mathbf{x},t,k,\theta,\Delta t) = \Delta t/\sigma$, $\sigma = l/c_g$ is the characteristic time step for one wave reflection event. l is the distance between two ice floes. In terms of these variables we have such discrete equation:

$$A(\mathbf{x},t+\Delta t,k,\theta) - A(\mathbf{x},t,k,\theta) = -c_g\theta\cdot\nabla A(\mathbf{x},t,k,\theta)\Delta t - \left(1-(1-r)^{c_g\Delta t/l}\right)A(\mathbf{x},t,k,\theta) \quad (7.29)$$

Next we divide the above equation with Δt

$$\frac{A(\mathbf{x},t+\Delta t,k,\theta) - A(\mathbf{x},t,k,\theta)}{\Delta t} = -c_g\theta\cdot\nabla A(\mathbf{x},t,k,\theta) - \frac{\left(1-(1-r)^{c_g\Delta t/l}\right)}{\Delta t}A(\mathbf{x},t,k,\theta) \quad (7.30)$$

Let $\Delta t \to 0$,

$$\frac{\partial A(\mathbf{x},t,k,\theta)}{\partial t} = -c_g\theta\cdot\nabla A(\mathbf{x},t,k,\theta) + \frac{c_g}{l}\ln(1-r)A(\mathbf{x},t,k,\theta) \qquad (7.31)$$

From the above, we have the temporal scattering attenuation coefficient

$$\alpha_s' = -\frac{c_g}{l}\ln(1-r) \qquad (7.32)$$

The spatial scattering attenuation coefficient is thus

$$\alpha_s = -\frac{1}{l}\ln(1-r) \qquad (7.33)$$

This result is consistent with Wadhams' scattering theory [17] and Squire's statistical calculation [53, 54].

7.4 Eddington approximation and multipole expansion

In this section, we show Eddington approximation is that the second order approximation in the mulptipole expansion of "spherical harmonics". For any function

defined on a sphere, the function can be represented as the sum of standard spherical harmonics:

$$f(\theta,\phi)=\sum_{i=0}^{\infty}\sum_{m=-i}^{i}C_i^m Y_i^m(\theta,\phi) \tag{7.34}$$

Here, $Y_i^m(\theta,\phi)'s$ are standard spherical harmonics, and $C_i^m's$ are constant coefficients which depend on the function. Equivalently, the series also can be written as the following,

$$f(\theta,\phi)=C+C_i n^i+C_{ij}n^i n^j+C_{ijk}n^i n^j n^k+C_{ijkl}n^i n^j n^k n^l+\cdots \tag{7.35}$$

Here, $n^i's$ represent the components of a unit vector in the direction given by the angles (θ,ϕ). Similarly, for a three dimensional function the series expainsion is as the following,

$$f(r,\theta,\phi)=C(r)+C_i(r)n^i+C_{ij}(r)n^i n^j+C_{ijk}(r)n^i n^j n^k+C_{ijkl}(r)n^i n^j n^k n^l+\cdots \tag{7.36}$$

Considering the scattered part of the wave action density function of ocean waves, the expansion is,

$$B(\mathbf{x},t,k,\theta)=\overline{B}(\mathbf{x},t,k)+B'(\mathbf{x},t,k,\theta)+B''(\mathbf{x},t,k,\theta)+B'''(\mathbf{x},t,k,\theta)+\cdots \tag{7.37}$$

Here,

$$B'(\mathbf{x},t,k,\theta)=C_i(\mathbf{x},t,k)n^i, \tag{7.38}$$

$$B''(\mathbf{x},t,k,\theta)=C_{ij}(\mathbf{x},t,k)n^i n^j, \tag{7.39}$$

$$B'''(\mathbf{x},t,k,\theta)=C_{ijl}(\mathbf{x},t,k)n^i n^j n^l. \tag{7.40}$$

The governing equations for each term without assuming c_g is isotropic are,

$$\frac{\partial}{\partial t}\overline{B}(\mathbf{x},t,k)=\nabla\cdot\mathbf{D}(\mathbf{x},t,k)\cdot\nabla\overline{B}(\mathbf{x},t,k)+c_g\frac{1}{2\pi}\int_0^{2\pi}\alpha_s(\mathbf{x},t,k,\theta')A(\mathbf{x},t,k,\theta')d\theta' \tag{7.41}$$

$$\frac{\partial}{\partial t}B'(\mathbf{x},t,k,\theta)+c_g\theta\cdot\nabla B(\mathbf{x},t,k)=-c_g\alpha_s(\mathbf{x},t,k,\theta)B'(\mathbf{x},t,k,\theta)$$
$$+c_g\int_0^{2\pi}S_k(\mathbf{x},t,k,\theta,\theta')B'(\mathbf{x},t,k,\theta')d\theta' \tag{7.42}$$

If we igore the time derivative term and directional redistribution term in Eq. (7.42), the equation directly leads to Eddington approximation.

$$B'(\mathbf{x},t,k,\theta)=-\frac{1}{\alpha_s}\theta\cdot\nabla\overline{B}(\mathbf{x},t,k) \tag{7.43}$$

CHAPTER 8 IMPLEMENTATION TO WW3 MODEL

To implement the theories developed in this study into the WW3 (or any other wave models) we need to have first the mechanical parameters, G and ν, of the ice covers and second an efficient way to solve for the wave number and attenuation, k_r and k_i. The former is linked to the group velocity V_g and the latter to the source term in Eq. (2.1). The dispersion relation is shown in Eq. (2.16). Once we have ice parameters for the region of interest, we can input these parameters into the wave ice interaction models to compute the wave speed and attenuation. This procedure is not straitforward, because for operational purpose we need to have a fast algorithm to find the solution for any parameter combination. In this chapter, we provide two possible parameterization to estimate G and ν. We then present a procedure to speedily implement the dispersion relation of the viscoelastic model into any wave models without the need to use pre-calculated lookup tables. This direct calculation is shown to converge quickly.

8.1 Introduction

The ice cover is modeled as a viscoelastic continuum with two parameters: shear modulus and viscosity. With five parameters (wave period, ice thickness, water depth, shear modulus, and viscosity) each over a broad range, it is not efficient to pre-calculate the wave speed and attenuation for all possible cases and present the results in a lookup table. Albeit such pre-calculation can be done once and for all, to access a lookup table in runtime can slow down the simulation considerably. Here we introduce a fast algorithm to solve the dispersion relation quickly. The speed of convergence for different parameter ranges is determined. This algorithm can easily be implemented in any wave models. The

unknown rheological parameters, i.e. the shear modulus and viscosity, need to be determined by measured data and more fundamental theories that relate the ice morphology to its mechanical properties.

8.2 Model description and the numerical procedure

In this section, we revisit the governing equations of ocean surface wave model, and explain how to implement viscoelastic wave ice interaction model in an ocean surface wave model.

8.2.1 Governing equation of ocean surface wave model

The dispersion relation for wave propagation under a viscoelastic ice cover has been developed in Wang and Shen [2010] as shown in subsection 2.3.4.

This dispersion relation has multiple modes as shown in chapter 5. The dominant mode is chosen to be used in WW3 because it contains most of the wave energy. This dominant mode is the one closest to the open water case.

8.2.2 Numerical procedure

In this section, we will introduce the numerical procedure to solve the roots of the dispersion relation, Eq. (2.16), from the viscoelastic model. We employ the Muller method [107]. There are multiple solutions. In the present analysis, we consider only the dominant mode, i.e. the mode closest to the open water case. It was found that the mode closest to the open water case contains the majority of the propagating wave energy, hence is an appropriate approximation for the full solution.

Muller's method uses a quadratic function to determine the roots as shown in Appendix G. This recursive method converges faster than the secant method which uses a

linear function. Starting with three initial values z_0, z_1 and z_2, the first iteration calculates the first approximation z_3. Each iteration uses the last three generated approximations to obtain the next.

The key step is to design a method that gives reasonable initial values z_0, z_1 and z_2 since they determine which root will be found and the convergence rate. From the previous study [23], we know that the dominant wave number under a viscoelastic cover is very close to the wave number of open water for wave periods greater than 10s. But for smaller wave periods, there is a large difference between the region under the viscoelastic cover and open water. Therefore, we separate the calculation procedure for initial values to two cases.

(1) If the wave period T is larger than 10s, we first solve the open water k_0 under the given angular frequency and water depth with initial values $z_0 = 0.01$, $z_1 = 0.1$ and $z_2 = 1$. Since the open water case has only two roots, one of them is negative hence unphysical, to ensure that we converge to the positive root, we use three positive initial values. The solving procedure is not sensitive to the initial values as long as they are positive. After k_0 is found, we then set $z_0 = 0.9k_0$, $z_1 = k_0$ and $z_2 = 1.1k_0$ as the initial values for the covered case to proceed.

(2) If wave period T is smaller than 10s, we first obtain the dominant root of Eq. (2.16) for a 10s wave with the given parameters using the method in case (1). We then approach T with an increment of $\Delta T = 0.1s$. At the n^{th} increment, we let the three initial guesses be $z_0 = 0.9k_{n-1}$, $z_1 = k_{n-1}$ and $z_2 = 1.1k_{n-1}$ where k_{n-1} is the root for the $(n-1)^{th}$ increment or a period of $10-(n-1)\Delta T$.

In regional or global wave models, a spectrum of wave periods needs to be followed in time and space. In step (2) above, if at each wave period one restarts from the 10s wave, there would be a lot of unnecessary repetition. To speed up, a period sweeping in the simulation should start from the lowest frequency and highest frequency. Once the solution of k is found, it should be saved for the next period. As long as the stepping size is maintained at $\Delta T \le 0.1s$ convergence to the desired root is confirmed.

The present algorithm is an alternative to constructing a lookup table. We have not tested the speed of using a lookup table to make a quantitative comparison.

8.3 Sample results

To test the numerical procedure in the above section, we calculate the real and imaginary part of the wave number and the group velocity with respect to wave period from 1s to 100s. Several viscoelastic parameters are selected. From Fig. 8-2 to Fig. 8-7, we show the sample results for the wave group velocity, wave attenuation and real wave number. Figure 8-8 provides the real part of the wave number normalized by the wave number of open water. This figure shows the numerical methods always converge to the dominant mode, which is close to open water case. The subsequent figures provide solutions for different viscoelastic materials with various equivalent shear moduli.

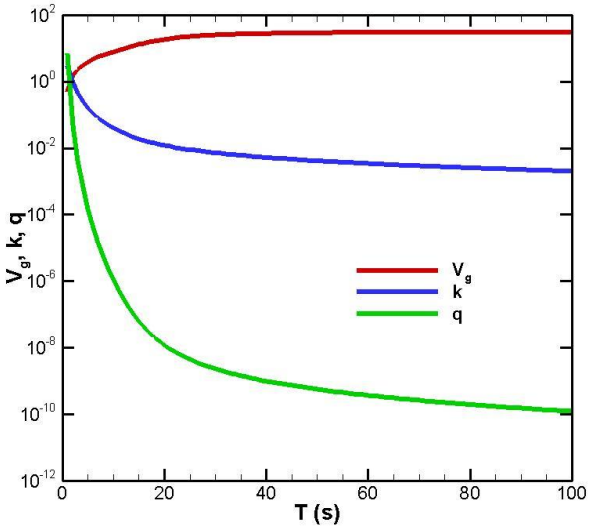

Fig. 8-2 Real part κ and imaginary part q and group velocity V_g with respect to wave period T. $\nu_{ice} = 0.05m^2/s$, $G = 0Pa$. $h = 1m$, $H = 100m$.

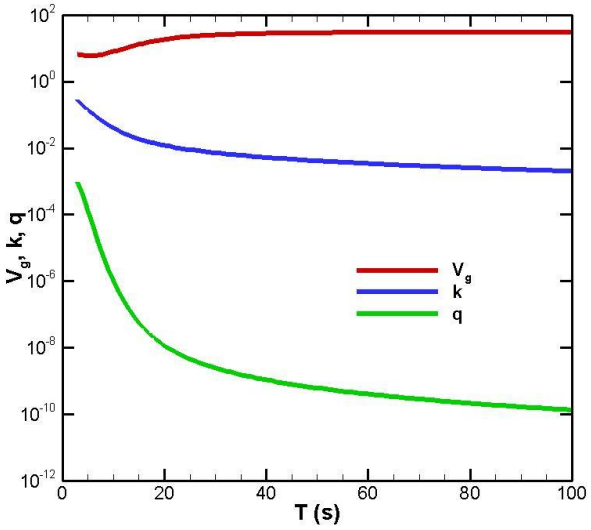

Fig. 8-3 Real part κ and imaginary part q and group velocity V_g with respect to wave period T. $\nu_{ice} = 0.05m^2/s$, $G = 10^4 Pa$. $h = 1m$, $H = 100m$.

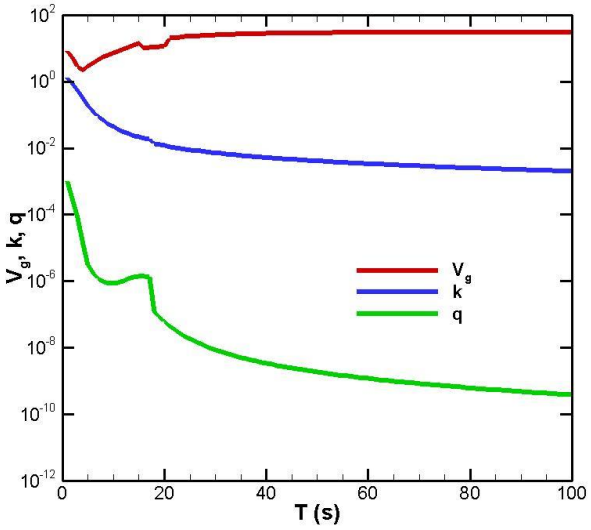

Fig. 8-4 Real part κ and imaginary part q and group velocity V_g with respect to wave period T. $\nu_{ice} = 0.05m^2/s$, $G = 10^5 Pa$. $h = 1m, H = 100m$.

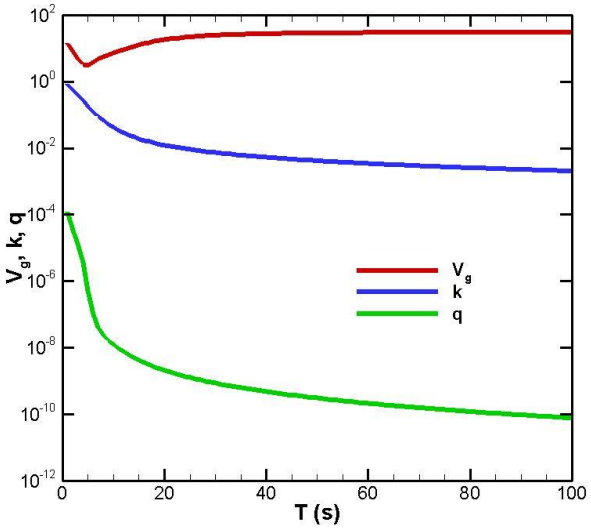

Fig. 8-5 Real part κ and imaginary part q and group velocity V_g with respect to wave period T. $\nu_{ice} = 0.05m^2/s$, $G = 5\times10^5 Pa$. $h = 1m, H = 100m$.

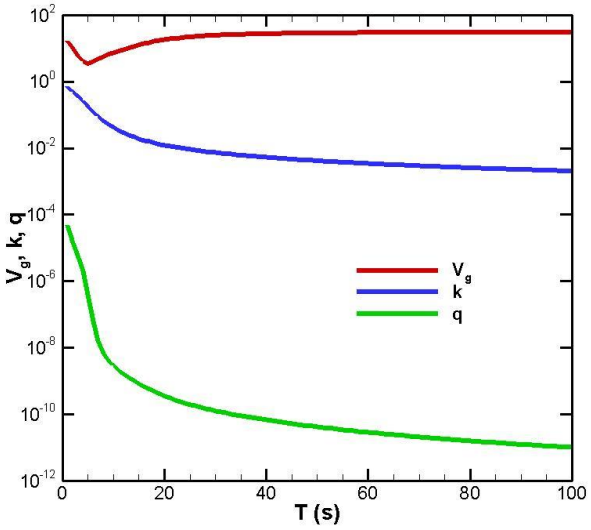

Fig. 8-6 Real part κ and imaginary part q and group velocity V_g with respect to wave period T. $\nu_{ice} = 0.05m^2/s$, $G = 10^6 Pa$. $h = 1m, H = 100m$.

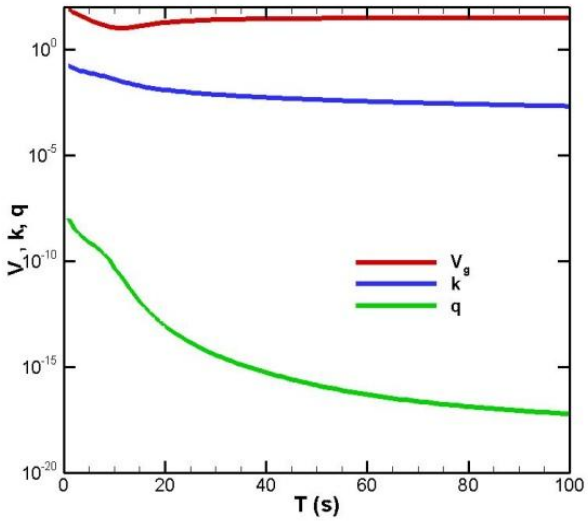

Fig. 8-7 Real part κ and imaginary part q and group velocity V_g with respect to wave period T. $\nu_{ice} = 0.05m^2/s$, $G = 10^9 Pa$. $h = 1m, H = 100m$.

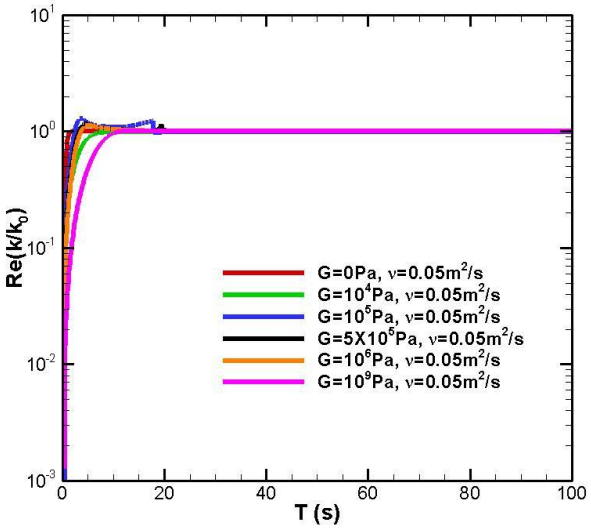

Fig. 8-8 Real part κ / k_0 with respect to wave period T. $h = 1m, H = 100m$.

From these results there are two phenomena worth noting:

As the period increases, not all three parameters, V_g, κ, q behave monotonically. As G increases, group velocity develops a minimum at some T.

The case $G = 10^4 Pa$ as shown in Fig. 8-4 and Fig. 8-8 is peculiar. The reason for the bumps in the curves is the mode switching phenomenon described in Wang and Shen [23]. In the regions where the bumps occur, a single dominant mode is insufficient to describe the wave propagation. At least two modes share similar energy and thus must be included. We consider these as special cases that require further study.

8. 4 Convergence rate

The convergence rate for the Muller method depends on the set convergence error. There are two convergence criteria: $\left|\frac{\Delta z}{z}\right| = \left|\frac{z_n - z_{n-1}}{z_n}\right| \le \varepsilon_1$; $\left|\Delta F(z)\right| = \left|F(z_n) - F(z_{n-1})\right| \le \varepsilon_2$.

The root computation is assumed to be achieved by satisfying both criteria. If the

convergence errors ε_1 and ε_2 are both set at 10^{-5}, the solution converges in about 3 steps for $T \geq 10$s. Figure 8-9 shows the computational time for different periods using an Intel Core2 Duo CPU T8300 @ 2.40GHz. If we do not sweep from long period to short period and save the solution for the next period, the time requirement increases with each shorter period. If we save the solution of the previous period and use it to construct the initial three values for the next period, the speed of convergence is constant for each period.

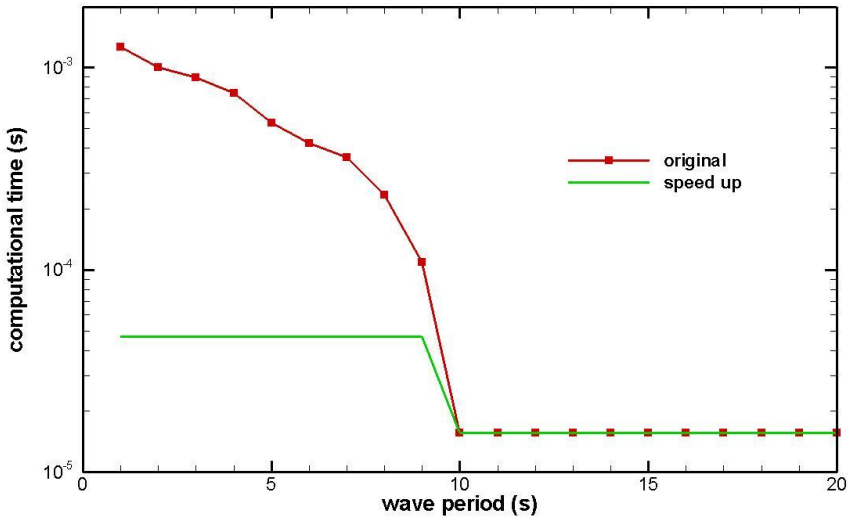

Fig. 8-9 Computational time with respect to wave period for original method and speed up method.

8.5 The viscoelastic parameter

To implement the above viscoelastic wave ice interaction model into a wave model, we need to estimate the viscoelastic parameter $\nu_e = \nu_{ice} + iG/\rho_{ice}\omega$. In other words, we need to determine the viscosity ν and shear modulus G from the physical composition of the ice cover. As discussed in chapter 6, field and laboratory studies are needed to bridge the ice cover morphology to its mechanical parameters. To date, there have been no theories, whether empirical or from the first principles, to relate the shear

modulus of an ice cover to its physical composition. Below we will make some recommendations based on very limited amount of study.

Sakai and Hanai [50] conducted wave flume experiment using polyethylene sheets as artificial ice floes. They propagated monochromatic wave over a group of floes. By changing the individual floe size while keeping the total covered area constant, the resulting phase velocity of the waves was measured. Using the dispersion relation from a pure thin elastic cover, they then determined the equivalent Young's modulus E of the fragmented ice cover as follows:

$$\frac{E}{E_{in}} = \begin{cases} 0 & IF \le 0.145 \\ \dfrac{IF - 0.145}{0.455} & 0.145 < IF \le 0.6 \\ 1 & IF > 0.6 \end{cases} \tag{8.3}$$

where

$$IF = \left(h / l_c\right)^{1/2} \log\left(l_i / l_c\right) \tag{8.4}$$

$$l_c = \left(E_{in} h^3 / 12 \rho_{ice} g \left(1 - \nu_p^2\right)\right)^{1/4} \tag{8.5}$$

E_{in} is the Young's modulus for individual ice floe, and ν_p is the Poisson ratio for individual ice floe. ρ_{ice} is the density of ice, and g is the gravity acceleration. Knowing the typical ice floe thickness h and length l_i, we can then obtain the equivalent Young's modulus of the ice-covered region E. The shear modulus and Young's modulus have the following relation:

$$G = \frac{E}{2\left(1 + \nu_p\right)} \tag{8.6}$$

For the viscosity of an ice cover region ν_{ice}, de Carolis et al. [106] derived a theory based on rigorous fluid mechanics of two-phase flows:

$$\nu_{ice} = \nu_{\max} f'(c_{ice}) \tag{8.7}$$

Here $\nu_{\max}$ is the maximum value of the viscosity, and $f'(c_{ice})$ is a function of c_{ice}, which is the concentration of the ice crystals in the water body. This theory is more appropriate for frazil ice where the composition of the ice cover is similar to a slurry. Before more advanced theories are developed, we may, based on the above study, suppose a linear function for $f'(c_{ice}) = c_{ice}$ and set $\nu_{\max} \approx 0.05 m^2/s$.

Another approach to estimate the viscoelastic parameters of the ice cover for use in the wave dispersion has been suggested by Erick Rogers of the Naval Research Laboratory [personal communication]. This idea is described below. The oceanic general circulation model (OGCM) is a numerical model to study the behavior of ocean at the mesoscale and global scale. In which, the movement of ice covers is an integral part of the model. The rheology of ice covers provides the necessary constitutive relation between the unknown internal ice stress to its kinematics, which then completes the momentum equation. This rheology is based on the theories developed by Hibler [108]. In this rheology, viscoelastic paramters have been calibrated to best reproduce the observed large scale ice kinematics. If indeed these paramters are reflections of the ice cover properties, there is no reason why they should be different in the wave-ice interaction process. Hence, we may also try to use the same parameterization as in the OGCM ice models for predicting wave under ice covers. The procedure for such estimates is shown in Appendix H with a sample data set provided by Rogers. What we have found is that the rheology in the OGCM yields very high viscosity parameter but reasonable elasticity parameters. It is worthwhile noting that OGCM ice products are mainly focused on the large scale ice cover motion, while wave propagation in ice covers

is mainly a marginal ice zone phenomenon. Once entered into the ice cover, attenuation rapidly decays the wave amplitude. The importance of waves is quickly diminished. In the marginal ice zone, where the ice cover meets the open ocean, the OGCM model and its parameterization may not work well. In fact, this topic is under active research at present (http://www.apl.washington.edu/project/project.php?id=miz).

8.6 Summary and conclusions

In the study of this chapter, we introduce a systematic algorithm to implement a viscoelastic wave ice interaction model into ocean wave models. This algorithm provides a speedy alternative to lookup table. This method is needed to extend the current "approximate" solution to include more modes. Two approaches are explained to provide parameterization. Both are highly speculative. More accurate methods to determine the shear modulus and viscosity of ice covers await further research. Two parameterization ideas are presented. Data from the field and laboratory experiments are needed to relate the ice cover morphology to their mechanical properties.

CHAPTER 9 SUMMARY AND FUTURE WORK

In this thesis, we briefly introduce the classification of sea ice based on their spatial distribution and their property. A three layer viscoelastic model which can simulate different kinds of ice covers is derived. This model can coverge to other wave ice interaction models under limiting conditions. Also, we provide an efficient algorithm to implement such kind of wave ice interaction model into the operational ocean wave models. In this thesis, we show how to analytically calculate the coefficients of reflection and transmission waves with approximate method and variational method. The behavior of these coefficients in relation to the mechanical properties of the ice cover is examined. Finally, we develop a set of governing equations to prepare the implementation of wave scattering into WW3 model with a diffusion approximation.

The finished research consists of eight tasks:

1. Review previous theories and research on wave ice interaction; (Chapter 2)
2. Develop a three-layer viscoelastic model to generalize previous six classic wave ice interaction models; (Chapter 3)
3. Design an efficient numerical method to implement viscoelastic model into ice covered ocean wave model; (Chapter 8)
4. Investigate the reflection and transmission coefficients between two connected ice-covered ocean region using the approximate solution method; (Chapter 4)
5. Investigate the reflection and transmission coefficients between two connected ice-covered ocean region using the variational method; (Chapter 5)

6. Derive the governing equations for wave scattering by randomly distributed ice floes for global ocean wave model; (Chapter 7)
7. Experimentally study the wave propagation under ice covers; (Chapter 6)
8. Apply sea ice model in the oceanic general circulation model to parameterize physical parameters in viscoelastic model. (Chapter 9)

There are several important future improvements required as listed below:

1. Study the source terms of wind input, dissipation and nonlinear interaction for ocean wave models in the ice covered region.
2. Apply the governing equations for wave scattering to be implemented into a global ocean wave model.
3. Study the "roll over" behavior of attenuation with full ocean wave model.
4. Apply the optimization inverse method to estimate the physical parameters in viscoelastic models from the laboratory and field data.
5. Establish the direct relation between ice morphology and physical parameters in the viscoelastic model.
6. Apply ocean wave model with wave ice interaction model for different kinds of ice covers to examine the existing models;
7. Examine other viscoelastic models different from the Voigt model.

We elaborate the above needs as follows.

Presently in all global wave models the wind energy input and wave breaking dissipation are simply reduced by the fraction of open water in the ice covered seas. The

nonlinear wave interaction term is unchanged. Theories developed for these terms are all based on the air-sea interactions. The presence of ice may significantly modify these physical processes.

Wave scattering effect is calculated for different kinds of regular ice floes and even for floes of arbitrary shapes. A linear Boltzmann equation is derived based on this calculation. This is expected to simulate the conservative term of sea ice source term for WW3 ocean wave model. But an exact model for wave scattering at single ice floe scale is computationally too expensive for a global ocean wave model. Probably, a statistical model based on scattering theory is more practical, because wave reflection/scatter is discontinuous and random both in time and space in the real ice covered ocean. This statistical model should be formulated as a governing equation for a continuum. Present three terms decomposition formulation is one option. We will integrate the three governing equations for wave scattering to compare with exact model to examine its accuracy.

Most wave ice interaction models cannot predict the roll-over effect of wave attenuation except Liu and Mollo-Christensen's eddy viscosity model [41]. The roll-over effect is only observed in field measurements, but in laboratory research such effect has not been found. On the other hand, including nonlinear wave interaction and wind effect, Perrie and Hu [14] also produced the roll-over effect. So it is interesting to check whether the roll-over is caused by wave-ice interaction alone, or by the combined effect of nonlinear wave interactions and wind wave generation.

The viscoelastic model is shown to incorporate all three distinct classic models. It has the capability to describe all different ice types by tuning the two materials

parameters: rigidity and viscosity. These two parameters are extremely difficult to derive from first principles. We propose to use an inverse method, i.e. directly measure wave number and wave attenuation as two inputs, through the dispersion relation, we may calculate the rigidity and viscosity. In this way we expect to find the relation between ice morphology and rheological parameters. Hence, extensive field and laboratory study is needed to provide sufficient data for both wave attenuation and wave number under various ice covers.

For viscous attenuation, the viscoelastic model can simulate different ice covers, such as grease ice, pancake ice, and continuous ice sheet. This model is already implemented into the most recent version of WW3 ocean wave model. The reflection phenomenon due to ice edge or inhomogeneous ice distribution is studied. We expect to also include such effect into WW3 to simulate a real ice covered ocean.

Finally, the calculation of the viscoelastic model is based on the Voigt model. We need to investigate the differences between Voigt model and other models, such as Maxwell-Voigt model [112] to see if there is any fundamental differences between the resulting dispersion relation.

REFERENCES

1. Komen G J, Cavaleri L, Donelan M, Hasselmann K, Hasselmann S, Janssen P A E M. Dynamics and modeling of ocean waves . Cambridge university press, 1996.
2. Thomson J, Rogers W E. Swell and sea in the emerging Arctic Ocean. Geophysical Research Letters, 2014.
3. Wadhams P. Ice in the Ocean. CRC Press, 2000.
4. Toyota T, Takatsuji S, Nakayama M. Characteristics of sea ice floe size distribution in the seasonal ice zone. Geophysical research letters, 2006, 33(2).
5. Perrie, W, Hu Y, 1997: Air–Ice–Ocean Momentum Exchange. Part II: Ice Drift. J. Phys. Oceanogr., 27, 1976–1996.
6. Dai M, Shen H H, Hopkins M A, et al. Wave rafting and the equilibrium pancake ice cover thickness. Journal of Geophysical Research: Oceans (1978–2012), 2004, 109(C7).
7. Tolman H L. Treatment of unresolved islands and ice in wind wave models. Ocean Modelling, 2003, 5(3): 219-231.
8. Kohout A L, Williams M J M, Dean S M, et al. Storm-induced sea-ice breakup and the implications for ice extent. Nature, 2014, 509(7502): 604-607.
9. Wadhams P, Squire V A, Goodman D J, et al. The attenuation rates of ocean waves in the marginal ice zone. Journal of Geophysical Research: Oceans (1978–2012), 1988, 93(C6): 6799-6818.
10. Squire V A, Dugan J P, Wadhams P, et al. Of ocean waves and sea ice. Annual Review of Fluid Mechanics, 1995, 27(1): 115-168.
11. Squire V A. Of ocean waves and sea-ice revisited. Cold Regions Science and Technology, 2007, 49(2): 110-133.
12. Dumont D, Kohout A, Bertino L. A wave‐based model for the marginal ice zone including a floe breaking parameterization. Journal of Geophysical Research: Oceans (1978–2012), 2011, 116(C4).
13. Masson D, LeBlond P H. Spectral evolution of wind-generated surface gravity waves in a dispersed ice field. Journal of Fluid Mechanics, 1989, 202: 43-81.
14. Perrie W, Hu Y. Air-ice-ocean momentum exchange. Part 1: Energy transfer between

waves and ice floes. Journal of physical oceanography, 1996, 26(9): 1705-1720.

15. Peters A S. The effect of a floating mat on water waves. Communications on Pure and Applied Mathematics, 1950, 3(4): 319-354.
16. Weitz M, Keller J B. Reflection of water waves from floating ice in water of finite depth. Communications on Pure and Applied Mathematics, 1950, 3(3): 305-318.
17. Wadhams P. The seasonal ice zone. The geophysics of sea ice. Springer US, 1986: 825-991.
18. Fox C, Squire V A. Reflection and transmission characteristics at the edge of shore fast sea ice. Journal of Geophysical Research: Oceans (1978–2012), 1990, 95(C7): 11629-11639.
19. Fox C, Squire V A. On the oblique reflexion and transmission of ocean waves at shore fast sea ice. Philosophical Transactions of the Royal Society of London. Series A: Physical and Engineering Sciences, 1994, 347(1682): 185-218.
20. Barrett M D, Squire V A. Ice-coupled wave propagation across an abrupt change in ice rigidity, density, or thickness. Journal of Geophysical Research: Oceans (1978–2012), 1996, 101(C9): 20825-20832.
21. Keller J B. Gravity waves on ice covered water. Journal of Geophysical Research: Oceans (1978–2012), 1998, 103(C4): 7663-7669.
22. De Carolis G, Desiderio D. Dispersion and attenuation of gravity waves in ice: a two-layer viscous fluid model with experimental data validation. Physics Letters A, 2002, 305(6): 399-412.
23. Wang R, Shen H H. Gravity waves propagating into an ice covered ocean: A viscoelastic model. Journal of Geophysical Research: Oceans (1978–2012), 2010, 115(C6).
24. Tolman H L. User manual and system documentation of WAVEWATCH III TM version 4.18b, 2014.
25. Miles J W. On the generation of surface waves by shear flows. Journal of Fluid Mechanics, 1957, 3(02): 185-204.
26. Gent P R, Taylor P A. A numerical model of the air flow above water waves. Journal of Fluid Mechanics, 1976, 77(01): 105-128.
27. Riley D S, Donelan M A, Hui W H. An extended Miles' theory for wave generation

by wind. Boundary-Layer Meteorology, 1982, 22(2): 209-225.
28. Al-Zanaidi M A, Hui W H. Turbulent airflow over water waves-a numerical study. Journal of Fluid Mechanics, 1984, 148: 225-246.
29. Jacobs S J. An asymptotic theory for the turbulent flow over a progressive water wave. Journal of Fluid Mechanics, 1987, 174: 69-80.
30. Chalikov D V, Makin V K. Models of the wave boundary layer. Boundary-Layer Meteorology, 1991, 56(1-2): 83-99.
31. Hasselmann K. On the non-linear energy transfer in a gravity-wave spectrum Part 1: General theory. J. Fluid Mech, 1962, 12(481-500): 15.
32. Hasselmann K. On the non-linear energy transfer in a gravity wave spectrum part 2. Conservation theorems; wave-particle analogy; inreversibility. Journal of Fluid Mechanics, 1963, 15(02): 273-281.
33. Hasselmann K. On the non-linear energy transfer in a gravity-wave spectrum. Part 3. Evaluation of the energy flux and swell-sea interaction for a Neumann spectrum. Journal of Fluid Mechanics, 1963, 15(03): 385-398.
34. Zakharov V E. Stability of periodic waves of finite amplitude on the surface of a deep fluid. Journal of Applied Mechanics and Technical Physics, 1968, 9(2): 190-194.
35. Janssen P. The interaction of ocean waves and wind. Cambridge University Press, 2004.
36. Hasselmann K. On the spectral dissipation of ocean waves due to white capping. Boundary-Layer Meteorology, 1974, 6(1-2): 107-127.
37. Phillips O M. Spectral and statistical properties of the equilibrium range in wind-generated gravity waves. Journal of Fluid Mechanics, 1985, 156: 505-531.
38. Jenkins A D. A Lagrangian model for wind-and wave-induced near-surface currents. Coastal engineering, 1987, 11(5): 513-526.
39. Rogers W E, Orzech M D. Implementation and testing of ice and mud source functions in WAVEWATCH III. NRL Memorandum Report. NRL/MR/7320–13-9462, 31 pp, 2013.
40. Gaster M. A note on the relation between temporally-increasing and spatially-increasing disturbances in hydrodynamic stability. Journal of Fluid Mechanics, 1962, 14(02): 222-224.

41. Liu A K, Mollo-Christensen E. Wave propagation in a solid ice pack. Journal of physical oceanography, 1988, 18(11): 1702-1712.
42. Meylan M H, Squire V A, Fox C. Toward realism in modeling ocean wave behavior in marginal ice zones. Journal of Geophysical Research: Oceans (1978–2012), 1997, 102(C10): 22981-22991.
43. Meylan M H, Masson D. A linear Boltzmann equation to model wave scattering in the marginal ice zone. Ocean Modelling, 2006, 11(3): 417-427.
44. Liu A K, Holt B, Vachon P W. Wave propagation in the marginal ice zone: Model predictions and comparisons with buoy and synthetic aperture radar data. Journal of Geophysical Research: Oceans (1978–2012), 1991, 96(C3): 4605-4621.
45. Squire V A, Allan A J, Propagation of flexural gravity waves in sea ice, in Sea Ice Processe and Models, Proceedings of the Arctic Ice Dynamics Joint Experiment, edited by R. S. Pritchard, pp. 327-338, University of Washington Press, Seattle, 1980.
46. Shen H H, Squire V A. Wave damping in compact pancake ice fields due to interactions between pancakes. Antarctic Sea Ice: Physical Processes, Interactions and Variability, 1998: 325-341.
47. Wang R X. Water Wave Propagation in Ice-Covered Oceans. PhD thesis, Clarkson University, USA, 2010.
48. Lange M A, Ackley S F, Wadhams P, et al. Development of sea ice in the Weddell Sea . Ann. Glaciol, 1989, 12: 92-96.
49. Squire V A. A comparison of the mass-loading and elastic plate models of an ice field . Cold regions science and technology, 1993, 21(3): 219-229.
50. Sakai S, Hanai K. Empirical formula of dispersion relation of waves in sea ice. Ice in the environment: Proceedings of the 16th IAHR International Symposium on Ice. 2002: 327-335.
51. Newyear K, Martin S. A comparison of theory and laboratory measurements of wave propagation and attenuation in grease ice. Journal of Geophysical Research: Oceans (1978–2012), 1997, 102(C11): 25091-25099.
52. Newyear K, Martin S. Comparison of laboratory data with a viscous two layer model of wave propagation in grease ice. Journal of Geophysical Research: Oceans (1978–2012), 1999, 104(C4): 7837-7840.

53. Bennetts L G, Squire V A. On the calculation of an attenuation coefficient for transects of ice-covered ocean. Proceedings of the Royal Society A: Mathematical, Physical and Engineering Science, 2012, 468(2137): 136-162.
54. Bennetts L G, Squire V A. Model sensitivity analysis of scattering-induced attenuation of ice-coupled waves. Ocean Modelling, 2012, 45: 1-13.
55. Meylan M, Squire V A. The response of ice floes to ocean waves. Journal of Geophysical Research: Oceans (1978–2012), 1994, 99(C1): 891-900.
56. Kohout A L. Water Wave Scattering by Floating Elastic Plates with Application to Sea Ice. PhD thesis, University of Auckland, USA, 2008.
57. Kohout A L, Meylan M H, Sakai S, et al. Linear water wave propagation through multiple floating elastic plates of variable properties. Journal of fluids and structures, 2007, 23(4): 649-663.
58. Wang R, Shen H H. A continuum model for the linear wave propagation in ice-covered oceans: An approximate solution. Ocean Modelling, 2011, 38(3): 244-250.
59. Zhao X, Shen H H. Ocean wave transmission and reflection between two connecting viscoelastic ice covers: An approximate solution. Ocean Modelling, 2013, 71: 102-113.
60. Sarpkaya T, Isaacson M. Mechanics of wave forces on offshore structures. New York: Van Nostrand Reinhold Company, 1981.
61. Meylan M H, Squire V A. Response of a circular ice floe to ocean waves. Journal of Geophysical Research: Oceans (1978–2012), 1996, 101(C4): 8869-8884.
62. Zhao X, Shen H H. Ocean wave transmission and reflection between two connecting viscoelastic ice covers: A variational approach, Ocean Modeling, submitted, 2014.
63. Meylan M H. Wave response of an ice floe of arbitrary geometry. Journal of Geophysical Research: Oceans (1978–2012), 2002, 107(C1): 5-1-5-11.
64. Kohout A L, Meylan M H. An elastic plate model for wave attenuation and ice floe breaking in the marginal ice zone. Journal of Geophysical Research: Oceans (1978–2012), 2008, 113(C9).
65. Dumont D, Kohout A, Bertino L. A wave‐based model for the marginal ice zone including a floe breaking parameterization. Journal of Geophysical Research: Oceans (1978–2012), 2011, 116(C4).

66. Williams T D, Bennetts L G, Squire V A, et al. Wave–ice interactions in the marginal ice zone. Part 1: Theoretical foundations. Ocean Modelling, 2013, 71: 81-91.
67. Williams T D, Bennetts L G, Squire V A, et al. Wave–ice interactions in the marginal ice zone. Part 2: Numerical implementation and sensitivity studies along 1D transects of the ocean surface. Ocean Modelling, 2013, 71: 92-101.
68. Toyota T, Haas C, Tamura T. Size distribution and shape properties of relatively small sea-ice floes in the Antarctic marginal ice zone in late winter. Deep Sea Research Part II: Topical Studies in Oceanography, 2011, 58(9): 1182-1193.
69. Harms V W. Steady wave-drift of modeled ice floes. Journal of Waterway, Port, Coastal, and Ocean Engineering, 1987, 113(6): 606-622.
70. Huang G, Law A W K, Huang Z. Wave-induced drift of small floating objects in regular waves. Ocean Engineering, 2011, 38(4): 712-718.
71. Huang G, Law A W K. Wave-induced drift of large floating objects in regular waves. Journal of Waterway, Port, Coastal, and Ocean Engineering, 2013, 139(6): 535-542.
72. Montiel F, Bonnefoy F, Ferrant P, et al. Hydroelastic response of floating elastic discs to regular waves. Part 1. Wave basin experiments. Journal of Fluid Mechanics, 2013, 723: 604-628.
73. Montiel F, Bennetts L G, Squire V A, et al. Hydroelastic response of floating elastic discs to regular waves. Part 2. Modal analysis. Journal of Fluid Mechanics, 2013, 723: 629-652.
74. Toyota T. A Study on Growth Processes of Sea Ice in the Southern Region of the Okhotsk Sea, Evaluated from Heat Budget and Sea Ice Sample Analysis, Ph.D. Dissertation, Hokkaido University, 143p, 1998.
75. Shen H H, Ackley S F, Yuan Y. Limiting diameter of pancake ice. Journal of Geophysical Research: Oceans (1978–2012), 2004, 109(C12).
76. Wang R, Shen H H and Evers K U. An experimental study of wave induced ice production. Proceedings of the 19th IAHR International Symposium on Ice, Vancouver, Canada, July 6-11, 2008.
77. Callinan C, Evers K U, Wilkinson J, Shen H H. Wave propagation in frazil/pancake and fragmented ice covers – part I: Description of the laboratory study. Proceedings of the 22nd IAHR Ice Symposium, Aug. 11-15, 2014, Singapore.

78. Zhao X, Callinan C, Shen H H. Wave propagation in frazil/pancake and fragmented ice covers – part II: Preliminary data analysis. Proceedings of the 22nd IAHR Ice Symposium, Aug. 11-15, 2014, Singapore.
79. Lansing A. Endurance: Shackleton's Incredible Voyage, Carroll and Graf Publishers. ISBN 0-7867-0621-X, 288p, 1959, 2nd ed. 1999.
80. Squire V A, Moore S C. Direct measurement of the attenuation of ocean waves by pack ice . Nature, 1980, 283: 365-368.
81. Wadhams P, Squire V A, Ewing J A, et al. The effect of the marginal ice zone on the directional wave spectrum of the ocean. Journal of physical oceanography, 1986, 16(2): 358-376.
82. Wadhams P, Squire V A, Goodman D J, et al. The attenuation rates of ocean waves in the marginal ice zone. Journal of Geophysical Research: Oceans (1978–2012), 1988, 93(C6): 6799-6818.
83. Frankenstein S, Loset S, Shen H H. Wave-ice interactions in Barents Sea marginal ice zone . Journal of cold regions engineering, 2001, 15(2): 91-102.
84. McKenna R F, Crocker G B. Ice‐floe collisions interpreted from acceleration data during LIMEX '89. Atmosphere-Ocean, 1992, 30(2): 246-269.
85. Rottier P J. Floe pair interaction event rates in the marginal ice zone. Journal of Geophysical Research: Oceans (1978–2012), 1992, 97(C6): 9391-9400.
86. Campbell A J, Bechle A J, Wu C H. Observations of surface waves interacting with ice using stereo imaging. Journal of Geophysical Research: Oceans, 2014.
87. Kwok R, Rignot E, Holt B, et al. Identification of sea ice types in spaceborne synthetic aperture radar data. Journal of Geophysical Research: Oceans (1978–2012), 1992, 97(C2): 2391-2402.
88. Wadhams P. Sea ice thickness distribution in the Greenland Sea and Eurasian Basin, May 1987. Journal of Geophysical Research: Oceans (1978–2012), 1992, 97(C4): 5331-5348.
89. Spreen G, Kaleschke L, Heygster G. Sea ice remote sensing using AMSR‐E 89‐GHz channels. Journal of Geophysical Research: Oceans (1978–2012), 2008, 113(C2).
90. Holt B, Rothrock D A, Kwok R. Determination of sea ice motion from satellite

images. Microwave Remote Sensing of Sea Ice, 1992: 343-354.

91. Luding S. Introduction to discrete element methods: basic of contact force models and how to perform the micro-macro transition to continuum theory. European Journal of Environmental and Civil Engineering, 2008, 12(7-8): 785-826.
92. Sun S, Shen H H. Simulation of pancake ice load on a circular cylinder in a wave and current field. Cold Regions Science and Technology, 2012, 78: 31-39.
93. Zhao X., Shen H H. Numerical simulation of gravity waves in viscous and viscoelastic materials, Proceedings of the 7th International Symposium on Environmental Hydraulics 2014 ISEH VII, Jan. 7-9, 2014 Singapore.
94. McPhee M G, Martinson D G. Turbulent mixing under drifting pack ice in the Weddell Sea. Science, 1994, 263(5144): 218-221.
95. Lamb, S. H. Hydrodynamics, Dover, New York, 1932.
96. Wadhams, P. The effect of a sea ice cover on ocean surface waves, Ph.D thesis, Univ. of Cambridge, England, 1973.
97. Wadhams, P. Attenuation of swell by sea ice, J. Geophys. Res., 1973, 78(18), 3552-3563.
98. Williams, T. D., Porter, R. The effect of submergence on the scattering by the interface between two semi-infinite sheets, Journal of Fluids and Structures, 2009, 25(5), 777-793.
99. Wilkinson, J. P., et al. Ice tank experiments highlight changes in sea ice types. Eos, Transactions American Geophysical Union, 2009, 90(10), 81-82.
100. Wang, R., Shen, H.H. Experimental study on surface wave propagating through a grease-pancake ice mixture. Cold Regions Science and Technology, 2010, 61, 90-96.
101. Callinan, C., Evers, K.-U., Wilkinson, J., Shen, H.H. A laboratory study of wave propagation in frazil/pancake and fragmented ice covers. Report 14-02, Department of Civil and Environmental Engineering, 2014, Clarkson University, Potsdam, NY, 16p.
102. Smedsrud, L.H., Skogseth, R. Field measurements of Arctic grease ice properties and processes. Cold Reg. Sci. Technol., 2006, 44, 171–183.
103. Timco, G. W., Weeks, W. F. A review of the engineering properties of sea ice. Cold Reg. Sci. Technol., 2010, 60, 107–129.

104. Pomraning G C. The equations of radiation hydrodynamics. Courier Dover Publications, 1973.

105. Wang L V, Wu H. Biomedical optics: principles and imaging. John Wiley and Sons, 2012.

106. de Carolis, G., Olla, P., Pignagnoli, L. (2005). Effective viscosity of grease ice in linearized gravity waves. Journal of Fluid Mechanics, *535*, 369-381.

107. Muller, David E. A Method for Solving Algebraic Equations Using an Automatic Computer, Mathematical Tables and Other Aids to Computation, 1956, 10, 208-215.

108. Hibler III, W. D. A dynamic thermodynamic sea ice model. Journal of Physical Oceanography, 1979, 9(4), 815-846.

109. Hunke, E. C., Dukowicz, J. K. An elastic-viscous-plastic model for sea ice dynamics. Journal of Physical Oceanography, 1997, 27(9), 1849-1867.

110. Hunke, E. C., Lipscomb, W. H. CICE: the Los Alamos sea ice model documentation and software user's manual. Los Alamos National Laboratory.

111. Hunke, E. C., Dukowicz, J. K. The elastic-viscous-plastic sea ice dynamics model in general orthogonal curvilinear coordinates on a sphere-incorporation of metric terms. Monthly Weather Review, 2002, 130(7), 1848-1865.

112. Squire V A, Allan A. Propagation of flexural gravity waves in sea ice . Sea Ice Processes and Models, Universtiy of Washington Press, Seattle, Washington, 1977.

Appendix A: Reduced boundary conditions in the three layer viscoelastic model

This appendix contains the reduced boundary condition equations in terms of potential functions and stream functions for the three-layer viscoelastic model.

$$-2\frac{\partial^2\phi_1}{\partial x\partial z}-\frac{\partial^2\psi_1}{\partial z^2}+\frac{\partial^2\psi_1}{\partial x^2}=0,\ z=h. \tag{A.1}$$

$$-\frac{\partial^2\phi_1}{\partial t^2}+g\left(-\frac{\partial\phi_1}{\partial z}+\frac{\partial\psi_1}{\partial x}\right)+2\nu_1\left(-\frac{\partial^3\phi_1}{\partial z^2\partial t}+\frac{\partial^3\psi_1}{\partial x\partial z\partial t}\right)=0,\ z=h. \tag{A.2}$$

$$\begin{aligned}&\rho_1\left[-\frac{\partial^2\phi_1}{\partial t^2}+g\left(-\frac{\partial\phi_1}{\partial z}+\frac{\partial\psi_1}{\partial x}\right)+2\nu_1\left(-\frac{\partial^3\phi_1}{\partial z^2\partial t}+\frac{\partial^3\psi_1}{\partial x\partial z\partial t}\right)\right]\\&-\rho_2\left[-\frac{\partial^2\phi_2}{\partial t^2}+g\left(-\frac{\partial\phi_2}{\partial z}+\frac{\partial\psi_2}{\partial x}\right)+2\nu_2\left(-\frac{\partial^3\phi_2}{\partial z^2\partial t}+\frac{\partial^3\psi_2}{\partial x\partial z\partial t}\right)\right]=0\end{aligned},\ z=0. \tag{A.3}$$

$$\rho_1\nu_1\left(-2\frac{\partial^2\phi_1}{\partial x\partial z}-\frac{\partial^2\psi_1}{\partial z^2}+\frac{\partial^2\psi_1}{\partial x^2}\right)-\rho_2\nu_2\left(-\frac{\partial^2\phi_2}{\partial x\partial z}-\frac{\partial^2\psi_2}{\partial z^2}+\frac{\partial^2\psi_2}{\partial x^2}\right)=0,\ z=0. \tag{A.4}$$

$$-\frac{\partial\phi_1}{\partial x}-\frac{\partial\psi_1}{\partial z}+\frac{\partial\phi_2}{\partial x}+\frac{\partial\psi_2}{\partial z},\ z=0. \tag{A.5}$$

$$-\frac{\partial\phi_1}{\partial z}+\frac{\partial\psi_1}{\partial x}+\frac{\partial\phi_2}{\partial z}-\frac{\partial\psi_2}{\partial x},\ z=0. \tag{A.6}$$

$$-\frac{\partial^2\phi_2}{\partial t^2}+2\nu_2\left(-\frac{\partial^3\phi_2}{\partial z^2\partial t}+\frac{\partial^3\psi_2}{\partial x\partial z\partial t}\right)+\frac{i\omega}{k\tanh k(z+H)}\frac{\partial w_2}{\partial t}=0,\ z=-b. \tag{A.7}$$

$$-2\frac{\partial^2\phi_2}{\partial x\partial z}-\frac{\partial^2\psi_2}{\partial z^2}+\frac{\partial^2\psi_2}{\partial x^2}=0,\ z=-b. \tag{A.8}$$

For the boundary condition equations for the two layer model, the first six boundary conditions are the same as the equations (A.1)-(A.6). The rest two equations are replaced by the non-slip boundary conditions.

$$u_2 = -\frac{\partial \phi_2}{\partial x} - \frac{\partial \psi_2}{\partial z} = 0\,,\ z = -H\,. \tag{A.9}$$

$$w_2 = -\frac{\partial \phi_2}{\partial z} + \frac{\partial \psi_2}{\partial x} = 0\,,\ z = -H\,. \tag{A.10}$$

Appendix B: Derivations of normal stresses and shear stresses in terms of the potential and stream functions

Substitute the velocity potential and stream functions into the expressions for stresses, we get

$$\tau_{xzi} = \tau_{zxi} = \rho_{ice}\nu_{ei}\left(\frac{\partial u_i}{\partial z} + \frac{\partial w_i}{\partial x}\right) = \rho_{ice}\nu_{ei}\left(-2\frac{\partial^2\varphi_i(x,z)}{\partial x\partial z} - \frac{\partial^2\psi_i(x,z)}{\partial z^2} + \frac{\partial^2\psi_i(x,z)}{\partial x^2}\right); \quad \text{(B.1)}$$

$$\tau_{xxi} = -p_i + 2\rho_{ice}\nu_{ei}\frac{\partial u_i}{\partial x} = i\omega\rho_{ice}\varphi_i(x,z) + 2\rho_{ice}\nu_{ei}\left(-\frac{\partial^2\varphi_i(x,z)}{\partial x^2} - \frac{\partial^2\psi_i(x,z)}{\partial x\partial z}\right); \quad \text{(B.2)}$$

$$\tau_{zzi} = -p_i + 2\rho_{ice}\nu_{ei}\frac{\partial w_i}{\partial z} = i\omega\rho_{ice}\varphi_i(x,z) + 2\rho_{ice}\nu_{ei}\left(-\frac{\partial^2\varphi_i(x,z)}{\partial z^2} + \frac{\partial^2\psi_i(x,z)}{\partial x\partial z}\right); \quad \text{(B.3)}$$

i=1,3

$$\tau_{xzi} = \tau_{zxi} = 0; \quad \text{(B.4)}$$

$$\tau_{xxi} = -p_i = i\omega\rho_{ice}\varphi_i(x,z); \quad \text{(B.5)}$$

$$\tau_{xxi} = -p_i = i\omega\rho_{ice}\varphi_i(x,z); \quad \text{(B.6)}$$

i=2,4

Appendix C: Matrix for solving $A_i(n)$, $B_i(n)$, $C_i(n)$, $D_i(n)$ and $E_i(n)$

Substituting the general solution into vertical boundary conditions, we obtain the matrix for solving the coefficients $A_i(n)$, $B_i(n)$, $C_i(n)$, $D_i(n)$ as follows.

$$\begin{bmatrix} 0 & 2ik_i^2(n) & \alpha_i^2(n)+k_i^2(n) & 0 \\ -2ik_i^2(n)Sk_i^n & 2ik_i^2(n)Ck_i^n & (\alpha_i^2(n)+k_i^2(n))C\alpha_i^n & -(\alpha_i^2(n)+k_i^2(n))S\alpha_i^n \\ N_i^n\omega & -k_i(n)g & ik_i(n)g & L_i^n \\ -M_i^nSk_i^n+N_i^n\omega Ck_i^n & M_i^nCk_i^n-N_i^n\omega Sk_i^n & -iM_i^nC\alpha_i^n-L_i^nS\alpha_i^n & iM_i^nS\alpha_i^n+L_i^nC\alpha_i^n \end{bmatrix} \begin{bmatrix} A_i(n) \\ B_i(n) \\ C_i(n) \\ D_i(n) \end{bmatrix} = \begin{bmatrix} 0 \\ 0 \\ 0 \\ 0 \end{bmatrix} \quad \text{(C.1)}$$

i=1,3 and n=1,2;

Here,

$$Sk_i^n = \sinh k_i(n)h_i \qquad \text{i=1,3 and n=1,2} \qquad \text{(C.2)}$$

$$Ck_i^n = \cosh k_i(n)h_i \qquad \text{i=1,3 and n=1,2} \qquad \text{(C.3)}$$

and

$$S\alpha_i^n = \sinh \alpha_i(n)h_i \qquad \text{i=1,3 and n=1,2} \qquad \text{(C.4)}$$

$$C\alpha_i^n = \cosh \alpha_i(n)h_i \qquad \text{i=1,3 and n=1,2} \qquad \text{(C.5)}$$

$$N_i^n = \omega + 2i\nu_{ei}k_i^2(n) \qquad \text{i=1,3 and n=1,2} \qquad \text{(C.6)}$$

$$M_i^n = \left(\frac{\rho_{water}}{\rho_{ice}} - 1\right)k_i(n)g - \frac{\rho_{water}}{\rho_{ice}}\frac{\omega}{\tanh(H-h_i)} \qquad \text{i=1,3 and n=1,2} \qquad \text{(C.7)}$$

$$L_i^n = 2\nu_{ei}\omega k_i(n)\alpha_i(n) \qquad \text{i=1,3 and n=1,2} \qquad \text{(C.8)}$$

Since the ice cover is considered as a continuum, the vertical velocity at the interface between two adjacent regions must be continuous. Therefore,

$$-\frac{\partial \varphi_2}{\partial z} = -\frac{\partial \varphi_1}{\partial z} + \frac{\partial \psi_1}{\partial x} \text{ at } z = -h_1 \tag{C.9}$$

$$-\frac{\partial \varphi_4}{\partial z} = -\frac{\partial \varphi_3}{\partial z} + \frac{\partial \psi_3}{\partial x} \text{ at } z = -h_3 \tag{C.10}$$

With these relations we can obtain $E_i(n)$:

$$E_i(n) = \frac{-A_i(n)Sk_i^n + B_i(n)Ck_i^n - iC_i(n)C\alpha_i^n + iD_i(n)S\alpha_i^n}{\sinh k_i(H-h_i)} \text{ i=1,3 and n=1,2} \tag{C.11}$$

Appendix D: Matrix for solving $I(1), R(1), R(2), T(1), T(2)$

Substituting the general solutions into the horizontal boundary conditions, we obtain the matrix for solving coefficients $I(1), R(1), R(2), T(1), T(2)$ as follows.

$$\mathbf{MT} = \mathbf{0} \tag{D.1}$$

$$\mathbf{T} = \left[I(1), R(1), R(2), T(1), T(2)\right]^T \tag{D.2}$$

In which $\mathbf{M}$ is a 9×5 matrix:

$$M_{1,1} = \frac{E_1(1)}{k_1(1)} \sinh k_1(1)(H - h_3); \tag{D.3}$$

$$M_{1,2} = M_{1,1}; \tag{D.4}$$

$$M_{1,3} = \frac{E_1(2)}{k_1(2)} \sinh k_1(2)(H - h_3); \tag{D.5}$$

$$M_{1,4} = \frac{E_3(1)}{k_3(1)} \sinh k_3(1)(H - h_3); \tag{D.6}$$

$$M_{1,5} = -\frac{E_3(2)}{k_3(2)} \sinh k_3(2)(H - h_3); \tag{D.7}$$

$$M_{2,1} = iE_1(1) \sinh k_1(1)(H - h_3); \tag{D.8}$$

$$M_{2,2} = -M_{2,1}; \tag{D.9}$$

$$M_{2,3} = iE_1(2) \sinh k_1(2)(H - h_3); \tag{D.10}$$

$$M_{2,4} = -iE_3(1) \sinh k_3(1)(H - h_3); \tag{D.11}$$

$$M_{2,5} = -iE_3(2) \sinh k_3(2)(H - h_3); \tag{D.12}$$

$$M_{3,1} = iA_1(1)\sinh k_1(1)h_1 + iB_1(1)(1-\cosh k_1(1)h_1) + C_1(1)(1-\cosh \alpha_1(1)h_1) + D_1(1)\sinh \alpha_1(1)h_1$$
; (D.13)

$$M_{3,2} = -iA_1(1)\sinh k_1(1)h_1 - iB_1(1)(1-\cosh k_1(1)h_1) + C_1(1)(1-\cosh \alpha_1(1)h_1) + D_1(1)\sinh \alpha_1(1)h_1$$
; (D.14)

$$M_{3,3} = -iA_1(2)\sinh k_1(2)h_1 - iB_1(2)(1-\cosh k_1(2)h_1) + C_1(2)(1-\cosh \alpha_1(2)h_1) + D_1(2)\sinh \alpha_1(2)h_1$$
; (D.15)

$$M_{3,4} = -iA_3(1)\sinh k_3(1)h_1 - iB_3(1)(1-\cosh k_3(1)h_1) - C_3(1)(1-\cosh \alpha_3(1)h_1) - D_3(1)\sinh \alpha_3(1)h_1$$
; (D.16)

$$M_{3,5} = -iA_3(2)\sinh k_3(2)h_1 - iB_3(2)(1-\cosh k_3(2)h_1) - C_3(2)(1-\cosh \alpha_3(2)h_1) - D_3(2)\sinh \alpha_3(2)h_1$$
; (D.17)

$$M_{4,1} = \frac{i\omega\rho_{ice}A_1(1)}{k_1(1)}\sinh k_1(1)h_1 + \frac{i\omega\rho_{ice}B_1(1)}{k_1(1)}(1-\cosh k_1(1)h_1) + 2\rho_{ice}\nu_{e1}k_1(1)A_1(1)\sinh k_1(1)h_1 +$$
$$2\rho_{ice}\nu_{e1}k_1(1)B_1(1)(1-\cosh k_1(1)h_1) - 2i\rho_{ice}\nu_{e1}k_1(1)C_1(1)(1-\cosh \alpha_1(1)h_1) - 2i\rho_{ice}\nu_{e1}k_1(1)D_1(1)\sinh \alpha_1(1)h_1$$
; (D.18)

$$M_{4,2} = \frac{i\omega\rho_{ice}A_1(1)}{k_1(1)}\sinh k_1(1)h_1 + \frac{i\omega\rho_{ice}B_1(1)}{k_1(1)}(1-\cosh k_1(1)h_1) + 2\rho_{ice}\nu_{e1}k_1(1)A_1(1)\sinh k_1(1)h_1 +$$
$$2\rho_{ice}\nu_{e1}k_1(1)B_1(1)(1-\cosh k_1(1)h_1) + 2i\rho_{ice}\nu_{e1}k_1(1)C_1(1)(1-\cosh \alpha_1(1)h_1) + 2i\rho_{ice}\nu_{e1}k_1(1)D_1(1)\sinh \alpha_1(1)h_1$$
; (D.19)

$$M_{4,3} = \frac{i\omega\rho_{ice}A_1(2)}{k_1(2)}\sinh k_1(2)h_1 + \frac{i\omega\rho_{ice}B_1(2)}{k_1(2)}(1-\cosh k_1(2)h_1) + 2\rho_{ice}\nu_{e1}k_1(2)A_1(2)\sinh k_1(2)h_1 +$$
$$2\rho_{ice}\nu_{e1}k_1(2)B_1(2)(1-\cosh k_1(2)h_1) + 2i\rho_{ice}\nu_{e1}k_1(2)C_1(2)(1-\cosh \alpha_1(2)h_1) + 2i\rho_{ice}\nu_{e1}k_1(2)D_1(2)\sinh \alpha_1(2)h_1$$
; (D.20)

$$M_{4,4} = -\frac{i\omega\rho_{ice}A_3(1)}{k_3(1)}\sinh k_3(1)h_1 + \frac{i\omega\rho_{ice}B_3(1)}{k_3(1)}(1-\cosh k_3(1)h_1) - 2\rho_{ice}\nu_{e3}k_3(1)A_3(1)\sinh k_3(1)h_1 -$$
$$2\rho_{ice}\nu_{e3}k_3(1)B_3(1)(1-\cosh k_3(1)h_1) + 2i\rho_{ice}\nu_{e3}k_3(1)C_3(1)(1-\cosh \alpha_3(1)h_1) + 2i\rho_{ice}\nu_{e3}k_3(1)D_3(1)\sinh \alpha_3(1)h_1$$
; (D.21)

$$M_{4,5} = -\frac{i\omega\rho_{ice}A_3(2)}{k_3(2)}\sinh k_3(2)h_1 - \frac{i\omega\rho_{ice}B_3(2)}{k_3(2)}(1-\cosh k_3(2)h_1) - 2\rho_{ice}\nu_{e3}k_3(2)A_3(2)\sinh k_3(2)h_1 -$$
$$2\rho_{ice}\nu_{e3}k_3(2)B_3(2)(1-\cosh k_3(2)h_1) + 2i\rho_{ice}\nu_{e3}k_3(2)C_3(2)(1-\cosh\alpha_3(2)h_1) + 2i\rho_{ice}\nu_{e3}k_3(2)D_3(2)\sinh\alpha_3(2)h_1 \quad ; \text{(D.22)}$$

$$M_{5,1} = iE_1(1)[\sinh k_1(1)(H-h_1) - \sinh k_1(1)(H-h_3)] \quad ; \text{(D.23)}$$

$$M_{5,2} = -M_{5,1} \quad ; \text{(D.24)}$$

$$M_{5,3} = -iE_1(2)[\sinh k_1(2)(H-h_1) - \sinh k_1(2)(H-h_3)] \quad \text{(D.25)}$$

$$M_{5,4} = iA_3(1)(\sinh k_3(1)h_1 - \sinh k_3(1)h_3) - iB_3(1)(\cosh k_3(1)h_1 - \cosh k_3(1)h_3)$$
$$-C_3(1)(\cosh\alpha_3(1)h_1 - \cosh\alpha_3(1)h_3) + D_3(1)(\sinh\alpha_3(1)h_1 - \sinh\alpha_3(1)h_3) \quad ; \text{(D.26)}$$

$$M_{5,5} = iA_3(2)(\sinh k_3(2)h_1 - \sinh k_3(2)h_3) - iB_3(2)(\cosh k_3(2)h_1 - \cosh k_3(2)h_3)$$
$$-C_3(2)(\cosh\alpha_3(2)h_1 - \cosh\alpha_3(2)h_3) + D_3(2)(\sinh\alpha_3(2)h_1 - \sinh\alpha_3(2)h_3) \quad ; \text{(D.27)}$$

$$M_{6,1} = \frac{i\omega\rho_{water}E_1(1)}{k_1(1)}[\sinh k_1(1)(H-h_1) - \sinh k_1(1)(H-h_3)] \quad ; \text{(D.28)}$$

$$M_{6,2} = -M_{6,1} \quad ; \text{(D.29)}$$

$$M_{6,3} = \frac{i\omega\rho_{water}E_1(2)}{k_1(2)}[\sinh k_1(2)(H-h_1) - \sinh k_1(2)(H-h_3)] \quad ; \text{(D.30)}$$

$$M_{6,4} = \frac{i\omega\rho_{ice}A_3(1)}{k_3(1)}(\sinh k_3(1)h_1 - \sinh k_3(1)h_3) - \frac{i\omega\rho_{ice}B_3(1)}{k_3(1)}(\cosh k_3(1)h_1 - \cosh k_3(1)h_3)$$
$$+2\rho_{ice}\nu_{e3}k_3(1)A_3(1)(\sinh k_3(1)h_1 - \sinh k_3(1)h_3) - 2\rho_{ice}\nu_{e3}k_3(1)B_3(1)(\cosh k_3(1)h_1 - \cosh k_3(1)h_3)$$
$$+2i\rho_{ice}\nu_{e3}k_3(1)C_3(1)(\cosh\alpha_3(1)h_1 - \cosh\alpha_3(1)h_3) - 2i\rho_{ice}\nu_{e3}k_3(1)D_3(1)(\sinh\alpha_3(1)h_1 - \sinh\alpha_3(1)h_3) \quad ; \text{(D.31)}$$

$$M_{6,5} = \frac{i\omega\rho_{ice}A_3(2)}{k_3(2)}(\sinh k_3(2)h_1 - \sinh k_3(2)h_3) - \frac{i\omega\rho_{ice}B_3(2)}{k_3(2)}(\cosh k_3(2)h_1 - \cosh k_3(2)h_3)$$
$$+ 2\rho_{ice}\nu_{e3}k_3(2)A_3(2)(\sinh k_3(2)h_1 - \sinh k_3(2)h_3) - 2\rho_{ice}\nu_{e3}k_3(2)B_3(2)(\cosh k_3(2)h_1 - \cosh k_3(2)h_3)$$
$$+ 2i\rho_{ice}\nu_{e3}k_3(2)C_3(2)(\cosh\alpha_3(2)h_1 - \cosh\alpha_3(2)h_3) - 2i\rho_{ice}\nu_{e3}k_3(2)D_3(2)(\sinh\alpha_3(2)h_1 - \sinh\alpha_3(2)h_3)$$
; (D.32)

$$M_{7,1} = 0\,; \tag{D.33}$$

$$M_{7,2} = 0\,; \tag{D.34}$$

$$M_{7,3} = 0\,; \tag{D.35}$$

$$\begin{aligned} M_{7,4} &= 2i\rho_{ice}\nu_{e3}A_3(1)k_3(1)(\cosh k_3(1)h_3 - \cosh k_3(1)h_1) \\ &+ 2i\rho_{ice}\nu_{e3}B_3(1)k_3(1)(\sinh k_3(1)h_3 - \sinh k_3(1)h_1) \\ &+ 2i\rho_{ice}\nu_{e3}C_3(1)\left(\alpha_3(1) + \frac{k_3^2(1)}{\alpha_3(1)}\right)(\sinh\alpha_3(1)h_3 - \sinh\alpha_3(1)h_1) \\ &+ 2i\rho_{ice}\nu_{e3}D_3(1)\left(\alpha_3(1) + \frac{k_3^2(1)}{\alpha_3(1)}\right)(\cosh\alpha_3(1)h_3 - \cosh\alpha_3(1)h_1) \end{aligned}\,; \tag{D.36}$$

$$\begin{aligned} M_{7,5} &= 2i\rho_{ice}\nu_{e3}A_3(2)k_3(2)(\cosh k_3(2)h_3 - \cosh k_3(2)h_1) \\ &+ 2i\rho_{ice}\nu_{e3}B_3(2)k_3(2)(\sinh k_3(2)h_3 - \sinh k_3(2)h_1) \\ &+ 2i\rho_{ice}\nu_{e3}C_3(2)\left(\alpha_3(2) + \frac{k_3^2(2)}{\alpha_3(2)}\right)(\sinh\alpha_3(2)h_3 - \sinh\alpha_3(2)h_1) \\ &+ 2i\rho_{ice}\nu_{e3}D_3(2)\left(\alpha_3(2) + \frac{k_3^2(2)}{\alpha_3(2)}\right)(\cosh\alpha_3(2)h_3 - \cosh\alpha_3(2)h_1) \end{aligned}\,; \tag{D.37}$$

$$M_{8,1} = -2i\rho_{ice}\nu_{e1}A_1(1)k_1(1)(1 - \cosh k_1(1)h_1) - 2i\rho_{ice}\nu_{e1}B_1(1)k_1(1)\sinh k_1(1)h_1$$
$$- \rho_{ice}\nu_{e1}C_1(1)\left(\alpha_1(1) + \frac{k_1^2(1)}{\alpha_1(1)}\right)\sinh\alpha_1(1)h_1 - \rho_{ice}\nu_{e1}D_1(1)\left(\alpha_1(1) + \frac{k_1^2(1)}{\alpha_1(1)}\right)(1 - \cosh\alpha_1(1)h_1)$$
; (D.38)

$$M_{8,2} = 2i\rho_{ice}\nu_{e1}A_1(1)k_1(1)(1-\cosh k_1(1)h_1) + 2i\rho_{ice}\nu_{e1}B_1(1)k_1(1)\sinh k_1(1)h_1$$
$$-\rho_{ice}\nu_{e1}C_1(1)\left(\alpha_1(1)+\frac{k_1^2(1)}{\alpha_1(1)}\right)\sinh\alpha_1(1)h_1 - \rho_{ice}\nu_{e1}D_1(1)\left(\alpha_1(1)+\frac{k_1^2(1)}{\alpha_1(1)}\right)(1-\cosh\alpha_1(1)h_1)$$
;

(D.39)

$$M_{8,3} = 2i\rho_{ice}\nu_{e1}A_1(2)k_1(2)(1-\cosh k_1(2)h_1) + 2i\rho_{ice}\nu_{e1}B_1(2)k_1(2)\sinh k_1(2)h_1$$
$$-\rho_{ice}\nu_{e1}C_1(2)\left(\alpha_1(2)+\frac{k_1^2(2)}{\alpha_1(2)}\right)\sinh\alpha_1(2)h_1 - \rho_{ice}\nu_{e1}D_1(2)\left(\alpha_1(2)+\frac{k_1^2(2)}{\alpha_1(2)}\right)(1-\cosh\alpha_1(2)h_1)$$
;

(D.40)

$$M_{8,4} = 2i\rho_{ice}\nu_{e3}A_3(1)k_3(1)(1-\cosh k_3(1)h_1) + 2i\rho_{ice}\nu_{e3}B_3(1)k_3(1)\sinh k_3(1)h_1$$
$$+\rho_{ice}\nu_{e3}C_3(1)\left(\alpha_3(1)+\frac{k_3^2(1)}{\alpha_3(1)}\right)\sinh\alpha_3(1)h_1 + \rho_{ice}\nu_{e3}D_3(1)\left(\alpha_3(1)+\frac{k_3^2(1)}{\alpha_3(1)}\right)(1-\cosh\alpha_3(1)h_1)$$
;

(D.41)

$$M_{8,5} = 2i\rho_{ice}\nu_{e3}A_3(2)k_3(2)(1-\cosh k_3(2)h_1) + 2i\rho_{ice}\nu_{e3}B_3(2)k_3(2)\sinh k_3(2)h_1$$
$$+\rho_{ice}\nu_{e3}C_3(2)\left(\alpha_3(2)+\frac{k_3^2(2)}{\alpha_3(2)}\right)\sinh\alpha_3(2)h_1 + \rho_{ice}\nu_{e3}D_3(2)\left(\alpha_3(2)+\frac{k_3^2(2)}{\alpha_3(2)}\right)(1-\cosh\alpha_3(2)h_1)$$
; (D.42)

$$M_{9,1} = -A_1(1)(1-\cosh k_1(1)h_1) - B_1(1)\sinh k_1(1)h_1$$
$$+i\frac{k_1(1)}{\alpha_1(1)}C_1(1)\sinh\alpha_1(1)h_1 + i\frac{k_1(1)}{\alpha_1(1)}D_1(1)(1-\cosh\alpha_1(1)h_1)$$
; (D.43)

$$M_{9,2} = -A_1(1)(1-\cosh k_1(1)h_1) - B_1(1)\sinh k_1(1)h_1$$
$$-i\frac{k_1(1)}{\alpha_1(1)}C_1(1)\sinh\alpha_1(1)h_1 - i\frac{k_1(1)}{\alpha_1(1)}D_1(1)(1-\cosh\alpha_1(1)h_1)$$
; (D.44)

$$M_{9,3} = -A_1(2)(1-\cosh k_1(2)h_1) - B_1(1)\sinh k_1(2)h_1$$
$$-i\frac{k_1(2)}{\alpha_1(2)}C_1(2)\sinh\alpha_1(2)h_1 - i\frac{k_1(2)}{\alpha_1(2)}D_1(2)(1-\cosh\alpha_1(2)h_1)$$
; (D.45)

$$M_{9,4} = A_3(1)(1-\cosh k_3(1)h_1) + B_3(1)\sinh k_3(1)h_1$$
$$-i\frac{k_3(1)}{\alpha_3(1)}C_3(1)\sinh \alpha_3(1)h_1 - i\frac{k_3(1)}{\alpha_3(1)}D_3(1)(1-\cosh \alpha_3(1)h_1); \quad \text{(D.46)}$$

$$M_{9,5} = A_3(2)(1-\cosh k_3(2)h_1) + B_3(2)\sinh k_3(2)h_1$$
$$-i\frac{k_3(2)}{\alpha_3(2)}C_3(2)\sinh \alpha_3(2)h_1 - i\frac{k_3(2)}{\alpha_3(2)}D_3(2)(1-\cosh \alpha_3(2)h_1); \quad \text{(D.47)}$$

Appendix E: Derivation for transmission and reflection coefficients

Due to the continuity requirement at the origin between ice region 1 and ice region 3,

$$\eta_1(0,t) = \eta_3(0,t)\,. \tag{E.1}$$

Here η_1 and η_3 are the displacement at the top of ice region 1 and ice region 3, respectively. This implies

$$\frac{\partial \eta_1(0,t)}{\partial t} = \frac{\partial \eta_3(0,t)}{\partial t}\,. \tag{E.2}$$

Hence the vertical velocity is continuous at the origin:

$$w_1(0,0) = w_3(0,0)\,. \tag{E.3}$$

Substituting the potential and stream functions for velocity into Eq. (E.3), we can obtain:

$$-\frac{\partial \varphi_1(0,0)}{\partial z} + \frac{\partial \psi_1(0,0)}{\partial x} = -\frac{\partial \varphi_3(0,0)}{\partial z} + \frac{\partial \psi_3(0,0)}{\partial x}\,. \tag{E.4}$$

We then substitute the general solution into Eq. (E.4) to get:

$$\begin{aligned} &-I(1)k_1(1)B_1(1) - R(1)k_1(1)B_1(1) - R(2)k_1(2)B_1(2) \\ &+iI(1)k_1(1)C_1(1) - iR(1)k_1(1)C_1(1) - iR(2)k_1(2)C_1(2) = \\ &-T(1)k_3(1)B_3(1) - T(2)k_3(2)B_3(2) + iT(1)k_3(1)C_3(1) + iT(2)k_3(2)C_3(2) \end{aligned} \quad ; \tag{E.5}$$

Simplify Eq. (E.5), we obtain the relation between reflection coefficient and transmission coefficient:

$$\begin{aligned} &I(1)(-k_1(1)B_1(1) + ik_1(1)C_1(1)) + R(1)(-k_1(1)B_1(1) - ik_1(1)C_1(1)) \\ &+ R(2)(-k_1(2)B_1(2) - ik_1(2)C_1(2)) = \\ &T(1)(-k_3(1)B_3(1) + ik_3(1)C_3(1)) + T(2)(-k_3(2)B_3(2) + ik_3(2)C_3(2)) \end{aligned} \quad ; \tag{E.6}$$

The following equations can be obtained:

$$R(1) = \frac{\left|R(1)\right\|k_1(1)B_1(1) + ik_1(1)C_1(1)\right|}{\left|I(1)\right\|k_1(1)B_1(1) - ik_1(1)C_1(1)\right|}; \tag{E.7}$$

$$R(2) = \frac{\left|R(2)\right\|k_1(2)B_1(2) + ik_1(2)C_1(2)\right|}{\left|I(1)\right\|k_1(1)B_1(1) - ik_1(1)C_1(1)\right|}; \tag{E.8}$$

$$T(1) = \frac{\left|T(1)\right\|k_3(1)B_3(1) - ik_3(1)C_3(1)\right|}{\left|I(1)\right\|k_1(1)B_1(1) - ik_1(1)C_1(1)\right|}; \tag{E.9}$$

$$T(2) = \frac{\left|T(2)\right\|k_3(2)B_3(2) - ik_3(2)C_3(2)\right|}{\left|I(1)\right\|k_1(1)B_1(1) - ik_1(1)C_1(1)\right|}. \tag{E.10}$$

Appendix F: Matrix $\mathbf{Q_n}$ for solving coefficients vector $\mathbf{u}$

If we substitute the general solutions into the error function, we can analytically calculate the matrix $\{\mathbf{Q_n}\}_{n=1}^{9}$.

The calculation of elements of matrix $\mathbf{Q_1}$

Firstly, we have

$$\varphi_2(0,z)-\varphi_4(0,z)=I(1)E_1(1)\cosh k_1(1)(z+H)+\sum_{n=1}^{N+2}R(n)E_1(n)\cosh k_1(n)(z+H)$$
$$-\sum_{n=1}^{N+2}T(n)E_3(n)\cosh k_3(n)(z+H) \tag{F.1}$$

We definne the vectors $\mathbf{e}$ and $\mathbf{k}$ as follows

$$\mathbf{e}=\left(E_1(1),E_1(1),E_1(2),\cdots,E_1(N+2),-E_3(1),-E_3(2),\cdots,-E_3(N+2)\right)^T \tag{F.2}$$

$$\mathbf{k}=\left(k_1(1),k_1(1),k_1(2),\cdots,k_1(N+2),k_3(1),k_3(2),\cdots,k_3(N+2)\right)^T \tag{F.3}$$

Then the element Q_{ij}^1 of matrix $\mathbf{Q_1}$ can be calculated as follows

$$\begin{aligned}Q_{ij}^1&=\int_{-H}^{-h_3}e_i^*e_j\cosh k_i^*(z+H)\cosh k_j(z+H)dz\\&=\frac{e_i^*e_j}{2}\int_{-H}^{-h_3}\left(\cosh(k_i^*+k_j)(z+H)+\cosh(k_i^*-k_j)(z+H)\right)dz\\&=\frac{e_i^*e_j}{2}\left(\frac{\sinh(k_i^*+k_j)(H-h_3)}{k_i^*+k_j}+\frac{\sinh(k_i^*-k_j)(z+H)}{k_i^*-k_j}\right)\end{aligned} \tag{F.4}$$

The calculation of elements of matrix $\mathbf{Q}_2$

$$u_2(0,z)-u_4(0,z)=\frac{\partial\varphi_2(0,z)}{\partial x}-\frac{\partial\varphi_4(0,z)}{\partial x}$$
$$=ik_1(1)I(1)E_1(1)\cosh k_1(1)(z+H)-\sum_{n=1}^{N+2}ik_1(n)R(n)E_1(n)\cosh k_1(n)(z+H)$$
$$-\sum_{n=1}^{N+2}ik_3(n)R(n)E_3(n)\cosh k_3(n)(z+H)$$

(F.5)

We define new $\mathbf{e}$ and $\mathbf{k}$ for this calculation

$$\mathbf{e}=(ik_1(1)E_1(1),-ik_1(1)E_1(1),-ik_1(2)E_1(2),\cdots,-ik_1(N+2)E_1(N+2),$$
$$-ik_3(1)E_3(1),-ik_3(2)E_3(2),\cdots,-ik_3(N+2)E_3(N+2))^T \quad \text{(F.6)}$$

$$\mathbf{k}=\left(k_1(1),k_1(1),k_1(2),\cdots,k_1(N+2),k_3(1),k_3(2),\cdots,k_3(N+2)\right)^T \quad \text{(F.7)}$$

Then we obtain

$$Q_{ij}^2=\int_{-H}^{-h_3}e_i^*e_j\cosh k_i^*(z+H)\cosh k_j(z+H)dz$$
$$=\frac{e_i^*e_j}{2}\left(\frac{\sinh(k_i^*+k_j)(H-h_3)}{k_i^*+k_j}+\frac{\sinh(k_i^*-k_j)(z+H)}{k_i^*-k_j}\right) \quad \text{(F.8)}$$

The calculation of elements of matrix $\mathbf{Q}_3$

$$-(u_1(0,z)-u_3(0,z))=\frac{\partial\varphi_1(0,z)}{\partial x}+\frac{\partial\psi_1(0,z)}{\partial z}-\frac{\partial\varphi_3(0,z)}{\partial x}-\frac{\partial\psi_3(0,z)}{\partial z}$$
$$=I(1)(ik_1(1)A_1(1)\cosh k_1(1)z+ik_1(1)B_1(1)\sinh k_1(1)z+\alpha_1(1)C_1(1)\sinh\alpha_1(1)z+\alpha_1(1)D_1(1)\cosh\alpha_1(1)z)$$
$$+\sum_{n=1}^{N+2}R(n)(-ik_1(n)A_1(n)\cosh k_1(n)z-ik_1(n)B_1(n)\sinh k_1(n)z+\alpha_1(n)C_1(n)\sinh\alpha_1(n)z+\alpha_1(n)D_1(n)\cosh\alpha_1(n)z)$$
$$-\sum_{n=1}^{N+2}T(n)(ik_3(n)A_3(n)\cosh k_3(n)z+ik_3(n)B_3(n)\sinh k_3(n)z+\alpha_3(n)C_3(n)\sinh\alpha_3(n)z+\alpha_3(n)D_3(n)\cosh\alpha_3(n)z)$$

(F.9)

We define vectors $\mathbf{a}$, $\mathbf{b}$, $\mathbf{c}$, $\mathbf{d}$, $\mathbf{k}$ and $\boldsymbol{\alpha}$ as follows

$$\mathbf{a}=(ik_1(1)A_1(1),-ik_1(1)A_1(1),-ik_1(2)A_1(2),\cdots,-ik_1(N+2)A_1(N+2),$$
$$-ik_3(1)A_3(1),-ik_3(2)A_3(2),\cdots,-ik_3(N+2)A_3(N+2))^T \quad \text{(F.10)}$$

$$\mathbf{b} = (ik_1(1)B_1(1), -ik_1(1)B_1(1), -ik_1(2)B_1(2), \cdots, -ik_1(N+2)B_1(N+2), \\ -ik_3(1)B_3(1), -ik_3(2)B_3(2), \cdots, -ik_3(N+2)B_3(N+2))^T \tag{F.11}$$

$$\mathbf{c} = (\alpha_1(1)C_1(1), \alpha_1(1)C_1(1), \alpha_1(2)C_1(2), \cdots, \alpha_1(N+2)C_1(N+2), \\ -\alpha_3(1)C_3(1), -\alpha_3(2)C_3(2), \cdots, -\alpha_3(N+2)C_3(N+2))^T \tag{F.12}$$

$$\mathbf{d} = (\alpha_1(1)D_1(1), \alpha_1(1)D_1(1), \alpha_1(2)D_1(2), \cdots, \alpha_1(N+2)D_1(N+2), \\ -\alpha_3(1)D_3(1), -\alpha_3(2)D_3(2), \cdots, -\alpha_3(N+2)D_3(N+2))^T \tag{F.13}$$

$$\mathbf{k} = \left(k_1(1), k_1(1), k_1(2), \cdots, k_1(N+2), k_3(1), k_3(2), \cdots, k_3(N+2)\right)^T \tag{F.14}$$

$$\boldsymbol{\alpha} = \left(\alpha_1(1), \alpha_1(1), \alpha_1(2), \cdots, \alpha_1(N+2), \alpha_3(1), \alpha_3(2), \cdots, \alpha_3(N+2)\right)^T \tag{F.15}$$

Then we can obtain

$$Q_{ij}^{3}=\int_{-h_1}^{0}(a_i^*\cosh k_i^*z+b_i^*\sinh k_i^*z+c_i^*\sinh\alpha_i^*z+d_i^*\cosh\alpha_i^*z)$$
$$(a_j\cosh k_jz+b_j\sinh k_jz+c_j\sinh\alpha_jz+d_j\cosh\alpha_jz)dz$$
$$=\frac{a_i^*a_j}{2}\left(\frac{\sinh(k_i^*+k_j)h_1}{k_i^*+k_j}+\frac{\sinh(k_i^*-k_j)h_1}{k_i^*-k_j}\right)+\frac{b_i^*a_j}{2}\left(\frac{1-\cosh(k_i^*+k_j)h_1}{k_i^*+k_j}+\frac{1-\cosh(k_i^*-k_j)h_1}{k_i^*-k_j}\right)$$
$$+\frac{c_i^*a_j}{2}\left(\frac{1-\cosh(\alpha_i^*+k_j)h_1}{\alpha_i^*+k_j}+\frac{1-\cosh(\alpha_i^*-k_j)h_1}{\alpha_i^*-k_j}\right)+\frac{d_i^*a_j}{2}\left(\frac{\sinh(\alpha_i^*+k_j)h_1}{\alpha_i^*+k_j}+\frac{\sinh(\alpha_i^*-k_j)h_1}{\alpha_i^*-k_j}\right)$$
$$+\frac{a_i^*b_j}{2}\left(\frac{1-\cosh(k_i^*+k_j)h_1}{k_i^*+k_j}-\frac{1-\cosh(k_i^*-k_j)h_1}{k_i^*-k_j}\right)+\frac{b_i^*b_j}{2}\left(\frac{\sinh(k_i^*+k_j)h_1}{k_i^*+k_j}-\frac{\sinh(k_i^*-k_j)h_1}{k_i^*-k_j}\right)$$
$$+\frac{c_i^*b_j}{2}\left(\frac{\sinh(\alpha_i^*+k_j)h_1}{\alpha_i^*+k_j}-\frac{\sinh(\alpha_i^*-k_j)h_1}{\alpha_i^*-k_j}\right)+\frac{d_i^*b_j}{2}\left(\frac{1-\cosh(\alpha_i^*+k_j)h_1}{\alpha_i^*+k_j}-\frac{1-\cosh(\alpha_i^*-k_j)h_1}{\alpha_i^*-k_j}\right)$$
$$+\frac{a_i^*c_j}{2}\left(\frac{1-\cosh(k_i^*+\alpha_j)h_1}{k_i^*+\alpha_j}-\frac{1-\cosh(k_i^*-\alpha_j)h_1}{k_i^*-\alpha_j}\right)+\frac{b_i^*c_j}{2}\left(\frac{\sinh(k_i^*+\alpha_j)h_1}{k_i^*+\alpha_j}-\frac{\sinh(k_i^*-\alpha_j)h_1}{k_i^*-\alpha_j}\right)$$
$$+\frac{c_i^*c_j}{2}\left(\frac{\sinh(\alpha_i^*+\alpha_j)h_1}{\alpha_i^*+\alpha_j}-\frac{\sinh(\alpha_i^*-\alpha_j)h_1}{\alpha_i^*-\alpha_j}\right)+\frac{d_i^*c_j}{2}\left(\frac{1-\cosh(\alpha_i^*+\alpha_j)h_1}{\alpha_i^*+\alpha_j}-\frac{1-\cosh(\alpha_i^*-\alpha_j)h_1}{\alpha_i^*-\alpha_j}\right)$$
$$+\frac{a_i^*d_j}{2}\left(\frac{\sinh(k_i^*+\alpha_j)h_1}{k_i^*+\alpha_j}+\frac{\sinh(k_i^*-\alpha_j)h_1}{k_i^*-\alpha_j}\right)+\frac{b_i^*d_j}{2}\left(\frac{1-\cosh(k_i^*+\alpha_j)h_1}{k_i^*+\alpha_j}+\frac{1-\cosh(k_i^*-\alpha_j)h_1}{k_i^*-\alpha_j}\right)$$
$$+\frac{c_i^*d_j}{2}\left(\frac{1-\cosh(\alpha_i^*+\alpha_j)h_1}{\alpha_i^*+\alpha_j}+\frac{1-\cosh(\alpha_i^*-\alpha_j)h_1}{\alpha_i^*-\alpha_j}\right)+\frac{d_i^*d_j}{2}\left(\frac{\sinh(\alpha_i^*+\alpha_j)h_1}{\alpha_i^*+\alpha_j}+\frac{\sinh(\alpha_i^*-\alpha_j)h_1}{\alpha_i^*-\alpha_j}\right)$$

(F.16)

The calculation of elements of matrix $\mathbf{Q}_4$

$$-(w_1(0,z)-w_3(0,z))=\frac{\partial\varphi_1(0,z)}{\partial z}-\frac{\partial\psi_1(0,z)}{\partial x}-\frac{\partial\varphi_3(0,z)}{\partial z}+\frac{\partial\psi_3(0,z)}{\partial x}$$
$$=I(1)(k_1(1)A_1(1)\sinh k_1(1)z+k_1(1)B_1(1)\cosh k_1(1)z-ik_1(1)C_1(1)\cosh\alpha_1(1)z-ik_1(1)D_1(1)\sinh\alpha_1(1)z)$$
$$+\sum_{n=1}^{N+2}R(n)(k_1(n)A_1(n)\sinh k_1(n)z+k_1(n)B_1(n)\cosh k_1(n)z+ik_1(n)C_1(n)\sinh\alpha_1(n)z+ik_1(n)D_1(n)\sinh\alpha_1(n)z)$$
$$-\sum_{n=1}^{N+2}T(n)(k_3(n)A_3(n)\sinh k_3(n)z+k_3(n)B_3(n)\cosh k_3(n)z-ik_3(n)C_3(n)\cosh\alpha_3(n)z-ik_3(n)D_3(n)\sinh\alpha_3(n)z)$$

(F.17)

We define new vectors $\mathbf{a}$, $\mathbf{b}$, $\mathbf{c}$, $\mathbf{d}$, $\mathbf{k}$ and $\boldsymbol{\alpha}$ as follows

$$\mathbf{a} = (k_1(1)A_1(1), k_1(1)A_1(1), k_1(2)A_1(2), \cdots, k_1(N+2)A_1(N+2), \\ -k_3(1)A_3(1), -k_3(2)A_3(2), \cdots, -k_3(N+2)A_3(N+2))^T \tag{F.18}$$

$$\mathbf{b} = (k_1(1)B_1(1), k_1(1)B_1(1), k_1(2)B_1(2), \cdots, k_1(N+2)B_1(N+2), \\ -k_3(1)B_3(1), -k_3(2)B_3(2), \cdots, -k_3(N+2)B_3(N+2))^T \tag{F.19}$$

$$\mathbf{c} = (-ik_1(1)C_1(1), ik_1(1)C_1(1), ik_1(2)C_1(2), \cdots, ik_1(N+2)C_1(N+2), \\ ik_3(1)C_3(1), ik_3(2)C_3(2), \cdots, ik_3(N+2)C_3(N+2))^T \tag{F.20}$$

$$\mathbf{d} = (-ik_1(1)D_1(1), ik_1(1)D_1(1), ik_1(2)D_1(2), \cdots, ik_1(N+2)D_1(N+2), \\ ik_3(1)D_3(1), ik_3(2)D_3(2), \cdots, ik_3(N+2)D_3(N+2))^T \tag{F.21}$$

$$\mathbf{k} = \left(k_1(1), k_1(1), k_1(2), \cdots, k_1(N+2), k_3(1), k_3(2), \cdots, k_3(N+2)\right)^T \tag{F.22}$$

$$\boldsymbol{\alpha} = \left(\alpha_1(1), \alpha_1(1), \alpha_1(2), \cdots, \alpha_1(N+2), \alpha_3(1), \alpha_3(2), \cdots, \alpha_3(N+2)\right)^T \tag{F.23}$$

Then we can obtain

$$Q_{ij}^4 = \int_{-h_1}^{0} (a_i^* \sinh k_i^* z + b_i^* \cosh k_i^* z + c_i^* \cosh \alpha_i^* z + d_i^* \sinh \alpha_i^* z)$$

$$(a_j \sinh k_j z + b_j \cosh k_j z + c_j \cosh \alpha_j z + d_j \sinh \alpha_j z) dz$$

$$= \frac{a_i^* a_j}{2}\left(\frac{\sinh(k_i^* + k_j)h_1}{k_i^* + k_j} - \frac{\sinh(k_i^* - k_j)h_1}{k_i^* - k_j}\right) + \frac{b_i^* a_j}{2}\left(\frac{1-\cosh(k_i^* + k_j)h_1}{k_i^* + k_j} - \frac{1-\cosh(k_i^* - k_j)h_1}{k_i^* - k_j}\right)$$

$$+ \frac{c_i^* a_j}{2}\left(\frac{1-\cosh(\alpha_i^* + k_j)h_1}{\alpha_i^* + k_j} - \frac{1-\cosh(\alpha_i^* - k_j)h_1}{\alpha_i^* - k_j}\right) + \frac{d_i^* a_j}{2}\left(\frac{\sinh(\alpha_i^* + k_j)h_1}{\alpha_i^* + k_j} - \frac{\sinh(\alpha_i^* - k_j)h_1}{\alpha_i^* - k_j}\right)$$

$$+ \frac{a_i^* b_j}{2}\left(\frac{1-\cosh(k_i^* + k_j)h_1}{k_i^* + k_j} + \frac{1-\cosh(k_i^* - k_j)h_1}{k_i^* - k_j}\right) + \frac{b_i^* b_j}{2}\left(\frac{\sinh(k_i^* + k_j)h_1}{k_i^* + k_j} + \frac{\sinh(k_i^* - k_j)h_1}{k_i^* - k_j}\right)$$

$$+ \frac{c_i^* b_j}{2}\left(\frac{\sinh(\alpha_i^* + k_j)h_1}{\alpha_i^* + k_j} + \frac{\sinh(\alpha_i^* - k_j)h_1}{\alpha_i^* - k_j}\right) + \frac{d_i^* b_j}{2}\left(\frac{1-\cosh(\alpha_i^* + k_j)h_1}{\alpha_i^* + k_j} + \frac{1-\cosh(\alpha_i^* - k_j)h_1}{\alpha_i^* - k_j}\right)$$

$$+ \frac{a_i^* c_j}{2}\left(\frac{1-\cosh(k_i^* + \alpha_j)h_1}{k_i^* + \alpha_j} + \frac{1-\cosh(k_i^* - \alpha_j)h_1}{k_i^* - \alpha_j}\right) + \frac{b_i^* c_j}{2}\left(\frac{\sinh(k_i^* + \alpha_j)h_1}{k_i^* + \alpha_j} + \frac{\sinh(k_i^* - \alpha_j)h_1}{k_i^* - \alpha_j}\right)$$

$$+ \frac{c_i^* c_j}{2}\left(\frac{\sinh(\alpha_i^* + \alpha_j)h_1}{\alpha_i^* + \alpha_j} + \frac{\sinh(\alpha_i^* - \alpha_j)h_1}{\alpha_i^* - \alpha_j}\right) + \frac{d_i^* c_j}{2}\left(\frac{1-\cosh(\alpha_i^* + \alpha_j)h_1}{\alpha_i^* + \alpha_j} + \frac{1-\cosh(\alpha_i^* - \alpha_j)h_1}{\alpha_i^* - \alpha_j}\right)$$

$$+ \frac{a_i^* d_j}{2}\left(\frac{\sinh(k_i^* + \alpha_j)h_1}{k_i^* + \alpha_j} - \frac{\sinh(k_i^* - \alpha_j)h_1}{k_i^* - \alpha_j}\right) + \frac{b_i^* d_j}{2}\left(\frac{1-\cosh(k_i^* + \alpha_j)h_1}{k_i^* + \alpha_j} - \frac{1-\cosh(k_i^* - \alpha_j)h_1}{k_i^* - \alpha_j}\right)$$

$$+ \frac{c_i^* d_j}{2}\left(\frac{1-\cosh(\alpha_i^* + \alpha_j)h_1}{\alpha_i^* + \alpha_j} - \frac{1-\cosh(\alpha_i^* - \alpha_j)h_1}{\alpha_i^* - \alpha_j}\right) + \frac{d_i^* d_j}{2}\left(\frac{\sinh(\alpha_i^* + \alpha_j)h_1}{\alpha_i^* + \alpha_j} - \frac{\sinh(\alpha_i^* - \alpha_j)h_1}{\alpha_i^* - \alpha_j}\right) \tag{F.24}$$

The calculation of elements of matrix $\mathbf{Q}_5$

$$
\begin{aligned}
&\tau_{xx1}(0,z)-\tau_{xx3}(0,z)\\
&=i\omega\rho_{ice}\varphi_1(0,z)-2\rho_{ice}\nu_{e1}\left(\frac{\partial^2\varphi_1(0,z)}{\partial x^2}+\frac{\partial^2\psi_1(0,z)}{\partial x\partial z}\right)-i\omega\rho_{ice}\varphi_3(0,z)+2\rho_{ice}\nu_{e3}\left(\frac{\partial^2\varphi_3(0,z)}{\partial x^2}+\frac{\partial^2\psi_3(0,z)}{\partial x\partial z}\right)\\
&=i\omega\rho_{ice}I(1)\left(A_1(1)\cosh k_1(1)z+B_1(1)\sinh k_1(1)z\right)\\
&+\sum_{n=1}^{N+2}i\omega\rho_{ice}R(n)\left(A_1(n)\cosh k_1(n)z+B_1(n)\sinh k_1(n)z\right)\\
&+2\rho_{ice}\nu_{e1}k_1^2(1)I(1)\left(A_1(1)\cosh k_1(1)z+B_1(1)\sinh k_1(1)z\right)\\
&+\sum_{n=1}^{N+2}2\rho_{ice}\nu_{e1}k_1^2(n)R(n)\left(A_1(n)\cosh k_1(n)z+B_1(n)\sinh k_1(n)z\right)\\
&-2i\rho_{ice}\nu_{e1}k_1(1)\alpha_1(1)I(1)\left(C_1(1)\sinh\alpha_1(1)z+D_1(1)\cosh\alpha_1(1)z\right)\\
&+\sum_{n=1}^{N+2}2i\rho_{ice}\nu_{e1}k_1(n)\alpha_1(n)R(n)\left(C_1(n)\sinh\alpha_1(n)z+D_1(n)\cosh\alpha_1(n)z\right)\\
&-\sum_{n=1}^{N+2}i\omega\rho_{ice}T(n)\left(A_3(n)\cosh k_3(n)z+B_3(n)\sinh k_3(n)z\right)\\
&-\sum_{n=1}^{N+2}2\rho_{ice}\nu_{e3}k_3^2(n)T(n)\left(A_3(n)\cosh k_3(n)z+B_3(n)\sinh k_3(n)z\right)\\
&+\sum_{n+1}^{N+2}2i\rho_{ice}\nu_{e3}k_3(n)\alpha_3(n)T(n)\left(C_3(n)\sinh\alpha_3(n)z+D_3(n)\cosh\alpha_3(n)z\right)
\end{aligned}
\tag{F.25}
$$

We define new vectors $\mathbf{a}$, $\mathbf{b}$, $\mathbf{c}$, $\mathbf{d}$, $\mathbf{k}$ and $\boldsymbol{\alpha}$ as follows

$$
\begin{aligned}
\mathbf{a}=&((i\omega\rho_{ice}+2\rho_{ice}\nu_{e1}k_1^2(1))A_1(1),(i\omega\rho_{ice}+2\rho_{ice}\nu_{e1}k_1^2(1))A_1(1),(i\omega\rho_{ice}+2\rho_{ice}\nu_{e1}k_1^2(2))A_1(2),\\
&\cdots,(i\omega\rho_{ice}+2\rho_{ice}\nu_{e1}k_1^2(N+2))A_1(N+2),-(i\omega\rho_{ice}+2\rho_{ice}\nu_{e3}k_3^2(1))A_3(1),-(i\omega\rho_{ice}+2\rho_{ice}\nu_{e3}k_3^2(2))A_3(2),\\
&\cdots,-(i\omega\rho_{ice}+2\rho_{ice}\nu_{e3}k_3^2(N+2))A_3(N+2))^T
\end{aligned}
\tag{F.26}
$$

$$
\begin{aligned}
\mathbf{b}=&((i\omega\rho_{ice}+2\rho_{ice}\nu_{e1}k_1^2(1))B_1(1),(i\omega\rho_{ice}+2\rho_{ice}\nu_{e1}k_1^2(1))B_1(1),(i\omega\rho_{ice}+2\rho_{ice}\nu_{e1}k_1^2(2))B_1(2),\\
&\cdots,(i\omega\rho_{ice}+2\rho_{ice}\nu_{e1}k_1^2(N+2))B_1(N+2),-(i\omega\rho_{ice}+2\rho_{ice}\nu_{e3}k_3^2(1))B_3(1),-(i\omega\rho_{ice}+2\rho_{ice}\nu_{e3}k_3^2(2))B_3(2),\\
&\cdots,-(i\omega\rho_{ice}+2\rho_{ice}\nu_{e3}k_3^2(N+2))B_3(N+2))^T
\end{aligned}
\tag{F.27}
$$

$$
\begin{aligned}
\mathbf{c}=&(-2i\rho_{ice}\nu_{e1}k_1(1)\alpha_1(1)C_1(1),2i\rho_{ice}\nu_{e1}k_1(1)\alpha_1(1)C_1(1),2i\rho_{ice}\nu_{e1}k_1(2)\alpha_1(2)C_1(2),\\
&\cdots,2i\rho_{ice}\nu_{e1}k_1(N+2)\alpha_1(N+2)C_1(N+2),2i\rho_{ice}\nu_{e3}k_3(1)\alpha_3(1)C_3(1),2i\rho_{ice}\nu_{e3}k_3(2)\alpha_3(2)C_3(2),\\
&\cdots,2i\rho_{ice}\nu_{e3}k_3(N+2)\alpha_3(N+2)C_3(N+2))^T
\end{aligned}
\tag{F.28}
$$

$$\mathbf{d} = (-2i\rho_{ice}\nu_{e1}k_1(1)\alpha_1(1)D_1(1), 2i\rho_{ice}\nu_{e1}k_1(1)\alpha_1(1)D_1(1), 2i\rho_{ice}\nu_{e1}k_1(2)\alpha_1(2)D_1(2),$$
$$\cdots, 2i\rho_{ice}\nu_{e1}k_1(N+2)\alpha_1(N+2)D_1(N+2), 2i\rho_{ice}\nu_{e3}k_3(1)\alpha_3(1)D_3(1), 2i\rho_{ice}\nu_{e3}k_3(2)\alpha_3(2)D_3(2),$$
$$\cdots, 2i\rho_{ice}\nu_{e3}k_3(N+2)\alpha_3(N+2)D_3(N+2))^T \tag{F.29}$$

$$\mathbf{k} = \left(k_1(1), k_1(1), k_1(2), \cdots, k_1(N+2), k_3(1), k_3(2), \cdots, k_3(N+2)\right)^T \tag{F.30}$$

$$\boldsymbol{\alpha} = \left(\alpha_1(1), \alpha_1(1), \alpha_1(2), \cdots, \alpha_1(N+2), \alpha_3(1), \alpha_3(2), \cdots, \alpha_3(N+2)\right)^T \tag{F.31}$$

Then we can obtain

$$Q_{ij}^5 = \int_{-h_1}^{0} (a_i^* \cosh k_i^* z + b_i^* \sinh k_i^* z + c_i^* \sinh \alpha_i^* z + d_i^* \cosh \alpha_i^* z)$$
$$(a_j \cosh k_j z + b_j \sinh k_j z + c_j \sinh \alpha_j z + d_j \cosh \alpha_j z) dz$$
$$= \frac{a_i^* a_j}{2}\left(\frac{\sinh(k_i^*+k_j)h_1}{k_i^*+k_j} + \frac{\sinh(k_i^*-k_j)h_1}{k_i^*-k_j}\right) + \frac{b_i^* a_j}{2}\left(\frac{1-\cosh(k_i^*+k_j)h_1}{k_i^*+k_j} + \frac{1-\cosh(k_i^*-k_j)h_1}{k_i^*-k_j}\right)$$
$$+ \frac{c_i^* a_j}{2}\left(\frac{1-\cosh(\alpha_i^*+k_j)h_1}{\alpha_i^*+k_j} + \frac{1-\cosh(\alpha_i^*-k_j)h_1}{\alpha_i^*-k_j}\right) + \frac{d_i^* a_j}{2}\left(\frac{\sinh(\alpha_i^*+k_j)h_1}{\alpha_i^*+k_j} + \frac{\sinh(\alpha_i^*-k_j)h_1}{\alpha_i^*-k_j}\right)$$
$$+ \frac{a_i^* b_j}{2}\left(\frac{1-\cosh(k_i^*+k_j)h_1}{k_i^*+k_j} - \frac{1-\cosh(k_i^*-k_j)h_1}{k_i^*-k_j}\right) + \frac{b_i^* b_j}{2}\left(\frac{\sinh(k_i^*+k_j)h_1}{k_i^*+k_j} - \frac{\sinh(k_i^*-k_j)h_1}{k_i^*-k_j}\right)$$
$$+ \frac{c_i^* b_j}{2}\left(\frac{\sinh(\alpha_i^*+k_j)h_1}{\alpha_i^*+k_j} - \frac{\sinh(\alpha_i^*-k_j)h_1}{\alpha_i^*-k_j}\right) + \frac{d_i^* b_j}{2}\left(\frac{1-\cosh(\alpha_i^*+k_j)h_1}{\alpha_i^*+k_j} - \frac{1-\cosh(\alpha_i^*-k_j)h_1}{\alpha_i^*-k_j}\right)$$
$$+ \frac{a_i^* c_j}{2}\left(\frac{1-\cosh(k_i^*+\alpha_j)h_1}{k_i^*+\alpha_j} - \frac{1-\cosh(k_i^*-\alpha_j)h_1}{k_i^*-\alpha_j}\right) + \frac{b_i^* c_j}{2}\left(\frac{\sinh(k_i^*+\alpha_j)h_1}{k_i^*+\alpha_j} - \frac{\sinh(k_i^*-\alpha_j)h_1}{k_i^*-\alpha_j}\right)$$
$$+ \frac{c_i^* c_j}{2}\left(\frac{\sinh(\alpha_i^*+\alpha_j)h_1}{\alpha_i^*+\alpha_j} - \frac{\sinh(\alpha_i^*-\alpha_j)h_1}{\alpha_i^*-\alpha_j}\right) + \frac{d_i^* c_j}{2}\left(\frac{1-\cosh(\alpha_i^*+\alpha_j)h_1}{\alpha_i^*+\alpha_j} - \frac{1-\cosh(\alpha_i^*-\alpha_j)h_1}{\alpha_i^*-\alpha_j}\right)$$
$$+ \frac{a_i^* d_j}{2}\left(\frac{\sinh(k_i^*+\alpha_j)h_1}{k_i^*+\alpha_j} + \frac{\sinh(k_i^*-\alpha_j)h_1}{k_i^*-\alpha_j}\right) + \frac{b_i^* d_j}{2}\left(\frac{1-\cosh(k_i^*+\alpha_j)h_1}{k_i^*+\alpha_j} + \frac{1-\cosh(k_i^*-\alpha_j)h_1}{k_i^*-\alpha_j}\right)$$
$$+ \frac{c_i^* d_j}{2}\left(\frac{1-\cosh(\alpha_i^*+\alpha_j)h_1}{\alpha_i^*+\alpha_j} + \frac{1-\cosh(\alpha_i^*-\alpha_j)h_1}{\alpha_i^*-\alpha_j}\right) + \frac{d_i^* d_j}{2}\left(\frac{\sinh(\alpha_i^*+\alpha_j)h_1}{\alpha_i^*+\alpha_j} + \frac{\sinh(\alpha_i^*-\alpha_j)h_1}{\alpha_i^*-\alpha_j}\right) \tag{F.32}$$

The calculation of elements of matrix $\mathbf{Q}_6$

$$
\begin{aligned}
&\tau_{xz1}(0,z)-\tau_{xz3}(0,z)\\
&=\rho_{ice}\nu_{e1}\left(2\frac{\partial^2\varphi_1(0,z)}{\partial x\partial z}+\frac{\partial^2\psi_1(0,z)}{\partial z^2}-\frac{\partial^2\psi_1(0,z)}{\partial x^2}\right)-\rho_{ice}\nu_{e3}\left(2\frac{\partial^2\varphi_3(0,z)}{\partial x\partial z}+\frac{\partial^2\psi_3(0,z)}{\partial z^2}-\frac{\partial^2\psi_3(0,z)}{\partial x^2}\right)\\
&=2i\rho_{ice}\nu_{e1}k_1^2(1)I(1)\left(A_1(1)\sinh k_1(1)z+B_1(1)\cosh k_1(1)z\right)\\
&-\sum_{n=1}^{N+2}2i\rho_{ice}\nu_{e1}k_1^2(n)R(n)\left(A_1(n)\sinh k_1(n)z+B_1(n)\cosh k_1(n)z\right)\\
&+\rho_{ice}\nu_{e1}\alpha_1^2(1)I(1)\left(C_1(1)\cosh\alpha_1(1)z+D_1(1)\sinh\alpha_1(1)z\right)\\
&+\sum_{n=1}^{N+1}\rho_{ice}\nu_{e1}\alpha_1^2(n)R(n)\left(C_1(n)\cosh\alpha_1(n)z+D_1(n)\sinh\alpha_1(n)z\right)\\
&+\rho_{ice}\nu_{e1}k_1^2(1)I(1)\left(C_1(1)\cosh\alpha_1(1)z+D_1(1)\sinh\alpha_1(1)z\right)\\
&+\sum_{n=1}^{N+1}\rho_{ice}\nu_{e1}k_1^2(n)R(n)\left(C_1(n)\cosh\alpha_1(n)z+D_1(n)\sinh\alpha_1(n)z\right)\\
&-\sum_{n=1}^{N+2}2i\rho_{ice}\nu_{e3}k_3^2(n)T(n)\left(A_3(n)\sinh k_3(n)z+B_3(n)\cosh k_3(n)z\right)\\
&-\sum_{n=1}^{N+2}\rho_{ice}\nu_{e3}\alpha_3^2(n)T(n)\left(C_3(n)\cosh\alpha_3(n)z+D_3(n)\sinh\alpha_3(n)z\right)\\
&-\sum_{n=1}^{N+2}\rho_{ice}\nu_{e3}k_3^2(n)T(n)\left(C_3(n)\cosh\alpha_3(n)z+D_3(n)\sinh\alpha_3(n)z\right)
\end{aligned}
\tag{F.33}
$$

We define new vectors $\mathbf{a}$, $\mathbf{b}$, $\mathbf{c}$, $\mathbf{d}$, $\mathbf{k}$ and $\boldsymbol{\alpha}$ as follows

$$
\begin{aligned}
\mathbf{a}=&(2i\rho_{ice}\nu_{e1}k_1^2(1)A_1(1),-2i\rho_{ice}\nu_{e1}k_1^2(1))A_1(1),-2i\rho_{ice}\nu_{e1}k_1^2(2)A_1(2),\\
&\cdots,-2i\rho_{ice}\nu_{e1}k_1^2(N+2)A_1(N+2),-2i\rho_{ice}\nu_{e3}k_3^2(1)A_3(1),-2i\rho_{ice}\nu_{e3}k_3^2(2)A_3(2),\\
&\cdots,-2i\rho_{ice}\nu_{e3}k_3^2(N+2)A_3(N+2))^T
\end{aligned}
\tag{F.34}
$$

$$
\begin{aligned}
\mathbf{b}=&(2i\rho_{ice}\nu_{e1}k_1^2(1)B_1(1),-2i\rho_{ice}\nu_{e1}k_1^2(1))B_1(1),-2i\rho_{ice}\nu_{e1}k_1^2(2)B_1(2),\\
&\cdots,-2i\rho_{ice}\nu_{e1}k_1^2(N+2)B_1(N+2),-2i\rho_{ice}\nu_{e3}k_3^2(1)B_3(1),-2i\rho_{ice}\nu_{e3}k_3^2(2)B_3(2),\\
&\cdots,-2i\rho_{ice}\nu_{e3}k_3^2(N+2)B_3(N+2))^T
\end{aligned}
\tag{F.35}
$$

$$\mathbf{c} = (\rho_{ice}\nu_{e1}(\alpha_1^2(1)+k_1^2(1))C_1(1), \rho_{ice}\nu_{e1}(\alpha_1^2(1)+k_1^2(1))C_1(1), \rho_{ice}\nu_{e1}(\alpha_1^2(2)+k_1^2(2))C_1(2),$$
$$\cdots, \rho_{ice}\nu_{e1}(\alpha_1^2(N+2)+k_1^2(N+2))C_1(N+2), -\rho_{ice}\nu_{e3}(\alpha_3^2(1)+k_3^2(1))C_3(1), -\rho_{ice}\nu_{e3}(\alpha_3^2(2)+k_3^2(2))C_3(2),$$
$$\cdots, -\rho_{ice}\nu_{e3}(\alpha_3^2(N+2)+k_3^2(N+2))C_3(N+2))^T \tag{F.36}$$

$$\mathbf{d} = (\rho_{ice}\nu_{e1}(\alpha_1^2(1)+k_1^2(1))D_1(1), \rho_{ice}\nu_{e1}(\alpha_1^2(1)+k_1^2(1))D_1(1), \rho_{ice}\nu_{e1}(\alpha_1^2(2)+k_1^2(2))D_1(2),$$
$$\cdots, \rho_{ice}\nu_{e1}(\alpha_1^2(N+2)+k_1^2(N+2))D_1(N+2), -\rho_{ice}\nu_{e3}(\alpha_3^2(1)+k_3^2(1))D_3(1), -\rho_{ice}\nu_{e3}(\alpha_3^2(2)+k_3^2(2))D_3(2),$$
$$\cdots, -\rho_{ice}\nu_{e3}(\alpha_3^2(N+2)+k_3^2(N+2))D_3(N+2))^T \tag{F.37}$$

$$\mathbf{k} = \left(k_1(1), k_1(1), k_1(2), \cdots, k_1(N+2), k_3(1), k_3(2), \cdots, k_3(N+2)\right)^T \tag{F.38}$$

$$\boldsymbol{\alpha} = \left(\alpha_1(1), \alpha_1(1), \alpha_1(2), \cdots, \alpha_1(N+2), \alpha_3(1), \alpha_3(2), \cdots, \alpha_3(N+2)\right)^T \tag{F.39}$$

Then we can obtain

$$Q_{ij}^{6}=\int_{-h_1}^{0}(a_i^*\sinh k_i^*z+b_i^*\cosh k_i^*z+c_i^*\cosh\alpha_i^*z+d_i^*\sinh\alpha_i^*z)$$
$$(a_j\sinh k_jz+b_j\cosh k_jz+c_j\cosh\alpha_jz+d_j\sinh\alpha_jz)dz$$
$$=\frac{a_i^*a_j}{2}\left(\frac{\sinh(k_i^*+k_j)h_1}{k_i^*+k_j}-\frac{\sinh(k_i^*-k_j)h_1}{k_i^*-k_j}\right)+\frac{b_i^*a_j}{2}\left(\frac{1-\cosh(k_i^*+k_j)h_1}{k_i^*+k_j}-\frac{1-\cosh(k_i^*-k_j)h_1}{k_i^*-k_j}\right)$$
$$+\frac{c_i^*a_j}{2}\left(\frac{1-\cosh(\alpha_i^*+k_j)h_1}{\alpha_i^*+k_j}-\frac{1-\cosh(\alpha_i^*-k_j)h_1}{\alpha_i^*-k_j}\right)+\frac{d_i^*a_j}{2}\left(\frac{\sinh(\alpha_i^*+k_j)h_1}{\alpha_i^*+k_j}-\frac{\sinh(\alpha_i^*-k_j)h_1}{\alpha_i^*-k_j}\right)$$
$$+\frac{a_i^*b_j}{2}\left(\frac{1-\cosh(k_i^*+k_j)h_1}{k_i^*+k_j}+\frac{1-\cosh(k_i^*-k_j)h_1}{k_i^*-k_j}\right)+\frac{b_i^*b_j}{2}\left(\frac{\sinh(k_i^*+k_j)h_1}{k_i^*+k_j}+\frac{\sinh(k_i^*-k_j)h_1}{k_i^*-k_j}\right)$$
$$+\frac{c_i^*b_j}{2}\left(\frac{\sinh(\alpha_i^*+k_j)h_1}{\alpha_i^*+k_j}+\frac{\sinh(\alpha_i^*-k_j)h_1}{\alpha_i^*-k_j}\right)+\frac{d_i^*b_j}{2}\left(\frac{1-\cosh(\alpha_i^*+k_j)h_1}{\alpha_i^*+k_j}+\frac{1-\cosh(\alpha_i^*-k_j)h_1}{\alpha_i^*-k_j}\right)$$
$$+\frac{a_i^*c_j}{2}\left(\frac{1-\cosh(k_i^*+\alpha_j)h_1}{k_i^*+\alpha_j}+\frac{1-\cosh(k_i^*-\alpha_j)h_1}{k_i^*-\alpha_j}\right)+\frac{b_i^*c_j}{2}\left(\frac{\sinh(k_i^*+\alpha_j)h_1}{k_i^*+\alpha_j}+\frac{\sinh(k_i^*-\alpha_j)h_1}{k_i^*-\alpha_j}\right)$$
$$+\frac{c_i^*c_j}{2}\left(\frac{\sinh(\alpha_i^*+\alpha_j)h_1}{\alpha_i^*+\alpha_j}+\frac{\sinh(\alpha_i^*-\alpha_j)h_1}{\alpha_i^*-\alpha_j}\right)+\frac{d_i^*c_j}{2}\left(\frac{1-\cosh(\alpha_i^*+\alpha_j)h_1}{\alpha_i^*+\alpha_j}+\frac{1-\cosh(\alpha_i^*-\alpha_j)h_1}{\alpha_i^*-\alpha_j}\right)$$
$$+\frac{a_i^*d_j}{2}\left(\frac{\sinh(k_i^*+\alpha_j)h_1}{k_i^*+\alpha_j}-\frac{\sinh(k_i^*-\alpha_j)h_1}{k_i^*-\alpha_j}\right)+\frac{b_i^*d_j}{2}\left(\frac{1-\cosh(k_i^*+\alpha_j)h_1}{k_i^*+\alpha_j}-\frac{1-\cosh(k_i^*-\alpha_j)h_1}{k_i^*-\alpha_j}\right)$$
$$+\frac{c_i^*d_j}{2}\left(\frac{1-\cosh(\alpha_i^*+\alpha_j)h_1}{\alpha_i^*+\alpha_j}-\frac{1-\cosh(\alpha_i^*-\alpha_j)h_1}{\alpha_i^*-\alpha_j}\right)+\frac{d_i^*d_j}{2}\left(\frac{\sinh(\alpha_i^*+\alpha_j)h_1}{\alpha_i^*+\alpha_j}-\frac{\sinh(\alpha_i^*-\alpha_j)h_1}{\alpha_i^*-\alpha_j}\right)$$

(F.40)

The calculation of elements of matrix $\mathbf{Q}_7$

$$-(u_2(0,z)-u_3(0,z))$$
$$=\frac{\partial\varphi_2(0,z)}{\partial x}-\frac{\partial\varphi_3(0,z)}{\partial x}-\frac{\partial\psi_3(0,z)}{\partial z}$$
$$=ik_1(1)I(1)E_1(1)\cosh k_1(1)(z+H)-\sum_{n=1}^{N+2}ik_1(n)R(n)E_1(n)\cosh k_1(n)(z+H)$$
$$-\sum_{n=1}^{N+2}ik_3(n)T(n)\left(A_3(n)\cosh k_3(n)z+B_3(n)\sinh k_3(n)z\right)$$
$$-\sum_{n=1}^{N+2}\alpha_3(n)T(n)\left(C_3(n)\sinh\alpha_3(n)z+D_3(n)\cosh\alpha_3(n)z\right)$$

(F.41)

We define new vectors $\mathbf{a}$, $\mathbf{b}$, $\mathbf{c}$, $\mathbf{d}$, $\mathbf{e}$, $\mathbf{k}$ and $\boldsymbol{\alpha}$ as follows

$$\mathbf{a} = (0,0,0,\cdots,0,-ik_3(1)A_3(1),-ik_3(2)A_3(2),\cdots,-ik_3(N+2)A_3(N+2))^T \tag{F.42}$$

$$\mathbf{b} = (0,0,0,\cdots,0,-ik_3(1)B_3(1),-ik_3(2)B_3(2),\cdots,-ik_3(N+2)B_3(N+2))^T \tag{F.43}$$

$$\mathbf{c} = (0,0,0,\cdots,0,-\alpha_3(1)C_3(1),-\alpha_3(2)C_3(2),\cdots,-\alpha_3(N+2)C_3(N+2))^T \tag{F.44}$$

$$\mathbf{d} = (0,0,0,\cdots,0,-\alpha_3(1)D_3(1),-\alpha_3(2)D_3(2),\cdots,-\alpha_3(N+2)D_3(N+2))^T \tag{F.45}$$

$$\mathbf{e} = (ik_1(1)E_1(1),-ik_1(1)E_1(1),-ik_1(2)E_1(2),\cdots,-ik_1(N+2)E_1(N+2),0,0,\cdots,0)^T \tag{F.46}$$

$$\mathbf{k} = \left(k_1(1),k_1(1),k_1(2),\cdots,k_1(N+2),k_3(1),k_3(2),\cdots,k_3(N+2)\right)^T \tag{F.47}$$

$$\boldsymbol{\alpha} = \left(\alpha_1(1),\alpha_1(1),\alpha_1(2),\cdots,\alpha_1(N+2),\alpha_3(1),\alpha_3(2),\cdots,\alpha_3(N+2)\right)^T \tag{F.48}$$

$$\begin{aligned} Q_{ij}^7 &= \int_{-h_3}^{-h_1} (e_i^* \cosh k_i^*(z+H) + a_i^* \cosh k_i^* z + b_i^* \sinh k_i^* z + c_i^* \sinh \alpha_i^* z + d_i^* \cosh \alpha_i^* z) \\ &(e_j \cosh k_j(z+H) + a_j \cosh k_j z + b_j \sinh k_j z + c_j \sinh \alpha_j z + d_j \cosh \alpha_j z)dz \\ &= part1 + part2 + part3 \end{aligned} \tag{F.49}$$

$$part1 = \frac{e_i^* e_j}{2}\left(\frac{\sinh(k_i^*+k_j)(H-h_1) - \sinh(k_i^*+k_j)(H-h_3)}{k_i^*+k_j} + \frac{\sinh(k_i^*-k_j)(H-h_1) - \sinh(k_i^*-k_j)(H-h_3)}{k_i^*-k_j}\right) \tag{F.50}$$

*part*2

$$= \frac{a_i^* e_j}{2}\left(\frac{\sinh(-(k_i^*+k_j)h_1+k_jH)-\sinh(-(k_i^*+k_j)h_3+k_jH)}{k_i^*+k_j}+\frac{\sinh(-(k_i^*-k_j)h_1-k_jH)-\sinh(-(k_i^*-k_j)h_3-k_jH)}{k_i^*-k_j}\right)$$

$$+\frac{b_i^* e_j}{2}\left(\frac{\cosh(-(k_i^*+k_j)h_1+k_jH)-\cosh(-(k_i^*+k_j)h_3+k_jH)}{k_i^*+k_j}+\frac{\cosh(-(k_i^*-k_j)h_1-k_jH)-\cosh(-(k_i^*-k_j)h_3-k_jH)}{k_i^*-k_j}\right)$$

$$+\frac{c_i^* e_j}{2}\left(\frac{\cosh(-(\alpha_i^*+k_j)h_1+k_jH)-\cosh(-(\alpha_i^*+k_j)h_3+k_jH)}{\alpha_i^*+k_j}+\frac{\cosh(-(\alpha_i^*-k_j)h_1-k_jH)-\cosh(-(\alpha_i^*-k_j)h_3-k_jH)}{\alpha_i^*-k_j}\right)$$

$$+\frac{d_i^* e_j}{2}\left(\frac{\sinh(-(\alpha_i^*+k_j)h_1+k_jH)-\sinh(-(\alpha_i^*+k_j)h_3+k_jH)}{\alpha_i^*+k_j}+\frac{\sinh(-(\alpha_i^*-k_j)h_1-k_jH)-\sinh(-(\alpha_i^*-k_j)h_3-k_jH)}{\alpha_i^*-k_j}\right)$$

$$+\frac{e_i^* a_j}{2}\left(\frac{\sinh(-(k_i^*+k_j)h_1+k_i^*H)-\sinh(-(k_i^*+k_j)h_3+k_i^*H)}{k_i^*+k_j}+\frac{\sinh(-(k_i^*-k_j)h_1+k_i^*H)-\sinh(-(k_i^*-k_j)h_3+k_i^*H)}{k_i^*-k_j}\right)$$

$$+\frac{e_i^* b_j}{2}\left(\frac{\cosh(-(k_i^*+k_j)h_1+k_i^*H)-\cosh(-(k_i^*+k_j)h_3+k_i^*H)}{k_i^*+k_j}-\frac{\cosh(-(k_i^*-k_j)h_1+k_i^*H)-\cosh(-(k_i^*-k_j)h_3+k_i^*H)}{k_i^*-k_j}\right)$$

$$+\frac{e_i^* c_j}{2}\left(\frac{\cosh(-(k_i^*+\alpha_j)h_1+k_i^*H)-\cosh(-(k_i^*+\alpha_j)h_3+k_i^*H)}{k_i^*+\alpha_j}-\frac{\cosh(-(k_i^*-\alpha_j)h_1+k_i^*H)-\cosh(-(k_i^*-\alpha_j)h_3+k_i^*H)}{k_i^*-\alpha_j}\right)$$

$$+\frac{e_i^* d_j}{2}\left(\frac{\sinh(-(k_i^*+\alpha_j)h_1+k_i^*H)-\sinh(-(k_i^*+\alpha_j)h_3+k_i^*H)}{k_i^*+\alpha_j}+\frac{\sinh(-(k_i^*-\alpha_j)h_1+k_i^*H)-\sinh(-(k_i^*-\alpha_j)h_3+k_i^*H)}{k_i^*-\alpha_j}\right)$$

(F.51)

*part*3

$$= \frac{a_i^* a_j}{2}\left(\frac{\sinh(-(k_i^*+k_j)h_1)-\sinh(-(k_i^*+k_j)h_3)}{k_i^*+k_j}+\frac{\sinh(-(k_i^*-k_j)h_1)-\sinh(-(k_i^*-k_j)h_3)}{k_i^*-k_j}\right)$$

$$+\frac{b_i^* a_j}{2}\left(\frac{\cosh(-(k_i^*+k_j)h_1)-\cosh(-(k_i^*+k_j)h_3)}{k_i^*+k_j}+\frac{\cosh(-(k_i^*-k_j)h_1)-\cosh(-(k_i^*-k_j)h_3)}{k_i^*-k_j}\right)$$

$$+\frac{c_i^* a_j}{2}\left(\frac{\cosh(-(\alpha_i^*+k_j)h_1)-\cosh(-(\alpha_i^*+k_j)h_3)}{\alpha_i^*+k_j}+\frac{\cosh(-(\alpha_i^*-k_j)h_1)-\cosh(-(\alpha_i^*-k_j)h_3)}{\alpha_i^*-k_j}\right)$$

$$+\frac{d_i^* a_j}{2}\left(\frac{\sinh(-(\alpha_i^*+k_j)h_1)-\sinh(-(\alpha_i^*+k_j)h_3)}{\alpha_i^*+k_j}+\frac{\sinh(-(\alpha_i^*-k_j)h_1)-\sinh(-(\alpha_i^*-k_j)h_3)}{\alpha_i^*-k_j}\right)$$

$$+\frac{a_i^* b_j}{2}\left(\frac{\cosh(-(k_i^*+k_j)h_1)-\cosh(-(k_i^*+k_j)h_3)}{k_i^*+k_j}-\frac{\cosh(-(k_i^*-k_j)h_1)-\cosh(-(k_i^*-k_j)h_3)}{k_i^*-k_j}\right)$$

$$+\frac{b_i^* b_j}{2}\left(\frac{\sinh(-(k_i^*+k_j)h_1)-\sinh(-(k_i^*+k_j)h_3)}{k_i^*+k_j}-\frac{\sinh(-(k_i^*-k_j)h_1)-\sinh(-(k_i^*-k_j)h_3)}{k_i^*-k_j}\right)$$

$$+\frac{c_i^* b_j}{2}\left(\frac{\sinh(-(\alpha_i^*+k_j)h_1)-\sinh(-(\alpha_i^*+k_j)h_3)}{\alpha_i^*+k_j}-\frac{\sinh(-(\alpha_i^*-k_j)h_1)-\sinh(-(\alpha_i^*-k_j)h_3)}{\alpha_i^*-k_j}\right)$$

$$+\frac{d_i^* b_j}{2}\left(\frac{\cosh(-(\alpha_i^*+k_j)h_1)-\cosh(-(\alpha_i^*+k_j)h_3)}{\alpha_i^*+k_j}-\frac{\cosh(-(\alpha_i^*-k_j)h_1)-\cosh(-(\alpha_i^*-k_j)h_3)}{\alpha_i^*-k_j}\right)$$

$$+\frac{a_i^* c_j}{2}\left(\frac{\cosh(-(k_i^*+\alpha_j)h_1)-\cosh(-(k_i^*+\alpha_j)h_3)}{k_i^*+\alpha_j}-\frac{\cosh(-(k_i^*-\alpha_j)h_1)-\cosh(-(k_i^*-\alpha_j)h_3)}{k_i^*-\alpha_j}\right)$$

$$+\frac{b_i^* c_j}{2}\left(\frac{\sinh(-(k_i^*+\alpha_j)h_1)-\sinh(-(k_i^*+\alpha_j)h_3)}{k_i^*+\alpha_j}-\frac{\sinh(-(k_i^*-\alpha_j)h_1)-\sinh(-(k_i^*-\alpha_j)h_3)}{k_i^*-\alpha_j}\right)$$

$$+\frac{c_i^* c_j}{2}\left(\frac{\sinh(-(\alpha_i^*+\alpha_j)h_1)-\sinh(-(\alpha_i^*+\alpha_j)h_3)}{\alpha_i^*+\alpha_j}-\frac{\sinh(-(\alpha_i^*-\alpha_j)h_1)-\sinh(-(\alpha_i^*-\alpha_j)h_3)}{\alpha_i^*-\alpha_j}\right)$$

$$+\frac{d_i^* c_j}{2}\left(\frac{\cosh(-(\alpha_i^*+\alpha_j)h_1)-\cosh(-(\alpha_i^*+\alpha_j)h_3)}{\alpha_i^*+\alpha_j}-\frac{\cosh(-(\alpha_i^*-\alpha_j)h_1)-\cosh(-(\alpha_i^*-\alpha_j)h_3)}{\alpha_i^*-\alpha_j}\right)$$

$$+\frac{a_i^* d_j}{2}\left(\frac{\sinh(-(k_i^*+\alpha_j)h_1)-\sinh(-(k_i^*+\alpha_j)h_3)}{k_i^*+\alpha_j}+\frac{\sinh(-(k_i^*-\alpha_j)h_1)-\sinh(-(k_i^*-\alpha_j)h_3)}{k_i^*-\alpha_j}\right)$$

$$+\frac{b_i^* d_j}{2}\left(\frac{\cosh(-(k_i^*+\alpha_j)h_1)-\cosh(-(k_i^*+\alpha_j)h_3)}{k_i^*+\alpha_j}+\frac{\cosh(-(k_i^*-\alpha_j)h_1)-\cosh(-(k_i^*-\alpha_j)h_3)}{k_i^*-\alpha_j}\right)$$

$$+\frac{c_i^* d_j}{2}\left(\frac{\cosh(-(\alpha_i^*+\alpha_j)h_1)-\cosh(-(\alpha_i^*+\alpha_j)h_3)}{\alpha_i^*+\alpha_j}+\frac{\cosh(-(\alpha_i^*-\alpha_j)h_1)-\cosh(-(\alpha_i^*-\alpha_j)h_3)}{\alpha_i^*-\alpha_j}\right)$$

$$+\frac{d_i^* d_j}{2}\left(\frac{\sinh(-(\alpha_i^*+\alpha_j)h_1)-\sinh(-(\alpha_i^*+\alpha_j)h_3)}{\alpha_i^*+\alpha_j}+\frac{\sinh(-(\alpha_i^*-\alpha_j)h_1)-\sinh(-(\alpha_i^*-\alpha_j)h_3)}{\alpha_i^*-\alpha_j}\right)$$

(F.52)

The calculation of elements of matrix $\mathbf{Q}_8$

$$\begin{aligned}
&\tau_{xx2}(0,z)-\tau_{xx3}(0,z)\\
&=i\omega\rho_{water}\varphi_2(0,z)-i\omega\rho_{ice}\varphi_3(0,z)+2\rho_{ice}\nu_{e3}\left(\frac{\partial^2\varphi_3(0,z)}{\partial x^2}+\frac{\partial^2\psi_3(0,z)}{\partial x\partial z}\right)\\
&=i\omega\rho_{water}I(1)E_1(1)\cosh k_1(1)(z+H)+\sum_{n=1}^{N+2}i\omega\rho_{water}R(n)E_1(n)\cosh k_1(n)(z+H)\\
&-\sum_{n=1}^{N+2}i\omega\rho_{ice}T(n)\left(A_3(n)\cosh k_3(n)z+B_3(n)\sinh k_3(n)z\right)\\
&-\sum_{n=1}^{N+2}2\rho_{ice}\nu_{e3}k_3^2(n)T(n)\left(A_3(n)\cosh k_3(n)z+B_3(n)\sinh k_3(n)z\right)\\
&+\sum_{n+1}^{N+2}2i\rho_{ice}\nu_{e3}k_3(n)\alpha_3(n)T(n)\left(C_3(n)\sinh\alpha_3(n)z+D_3(n)\cosh\alpha_3(n)z\right)
\end{aligned}$$

(F.53)

We define new vectors $\mathbf{a}$, $\mathbf{b}$, $\mathbf{c}$, $\mathbf{d}$, $\mathbf{e}$, $\mathbf{k}$ and $\boldsymbol{\alpha}$ as follows

$$\mathbf{a}=(0,0,0,\cdots,0,-(i\omega+2k_3^2(1)\nu_{e3})\rho_{ice}A_3(1),-(i\omega+2k_3^2(2)\nu_{e3})\rho_{ice}A_3(2),\cdots,-(i\omega+2k_3^2(N+2)\nu_{e3})\rho_{ice}A_3(N+2))^T \quad \text{(F.54)}$$

$$\mathbf{b}=(0,0,0,\cdots,0,-(i\omega+2k_3^2(1)\nu_{e3})\rho_{ice}B_3(1),-(i\omega+2k_3^2(2)\nu_{e3})\rho_{ice}B_3(2),\cdots,-(i\omega+2k_3^2(N+2)\nu_{e3})\rho_{ice}B_3(N+2))^T \quad \text{(F.55)}$$

$$\mathbf{c}=(0,0,0,\cdots,0,2ik_3(1)\alpha_3(1)\rho_{ice}\nu_{e3}C_3(1),2ik_3(2)\alpha_3(2)\rho_{ice}\nu_{e3}C_3(2),\cdots,2ik_3(N+2)\alpha_3(N+2)\rho_{ice}\nu_{e3}C_3(N+2))^T \quad \text{(F.56)}$$

$$\mathbf{d}=(0,0,0,\cdots,0,2ik_3(1)\alpha_3(1)\rho_{ice}\nu_{e3}D_3(1),2ik_3(2)\alpha_3(2)\rho_{ice}\nu_{e3}D_3(2),\cdots,2ik_3(N+2)\alpha_3(N+2)\rho_{ice}\nu_{e3}D_3(N+2))^T \quad \text{(F.57)}$$

$$\mathbf{e}=(i\omega\rho_{water}E_1(1),i\omega\rho_{water}E_1(1),i\omega\rho_{water}E_1(2),\cdots,i\omega\rho_{water}E_1(N+2),0,0,\cdots,0)^T \quad \text{(F.58)}$$

$$\mathbf{k}=\left(k_1(1),k_1(1),k_1(2),\cdots,k_1(N+2),k_3(1),k_3(2),\cdots,k_3(N+2)\right)^T \quad \text{(F.59)}$$

$$\boldsymbol{\alpha}=\left(\alpha_1(1),\alpha_1(1),\alpha_1(2),\cdots,\alpha_1(N+2),\alpha_3(1),\alpha_3(2),\cdots,\alpha_3(N+2)\right)^T \quad \text{(F.60)}$$

Then we can obtain

$$Q_{ij}^{8} = \int_{-h_3}^{-h_1} (e_i^* \cosh k_i^*(z+H) + a_i^* \cosh k_i^* z + b_i^* \sinh k_i^* z + c_i^* \sinh \alpha_i^* z + d_i^* \cosh \alpha_i^* z)$$
$$(e_j \cosh k_j(z+H) + a_j \cosh k_j z + b_j \sinh k_j z + c_j \sinh \alpha_j z + d_j \cosh \alpha_j z)dz$$
$$= part1 + part2 + part3$$

(F.61)

$$part1$$
$$= \frac{e_i^* e_j}{2}\left(\frac{\sinh(k_i^* + k_j)(H-h_1) - \sinh(k_i^* + k_j)(H-h_3)}{k_i^* + k_j} + \frac{\sinh(k_i^* - k_j)(H-h_1) - \sinh(k_i^* - k_j)(H-h_3)}{k_i^* - k_j}\right)$$

(F.62)

$$part2$$
$$= \frac{a_i^* e_j}{2}\left(\frac{\sinh(-(k_i^* + k_j)h_1 + k_j H) - \sinh(-(k_i^* + k_j)h_3 + k_j H)}{k_i^* + k_j} + \frac{\sinh(-(k_i^* - k_j)h_1 - k_j H) - \sinh(-(k_i^* - k_j)h_3 - k_j H)}{k_i^* - k_j}\right)$$
$$+ \frac{b_i^* e_j}{2}\left(\frac{\cosh(-(k_i^* + k_j)h_1 + k_j H) - \cosh(-(k_i^* + k_j)h_3 + k_j H)}{k_i^* + k_j} + \frac{\cosh(-(k_i^* - k_j)h_1 - k_j H) - \cosh(-(k_i^* - k_j)h_3 - k_j H)}{k_i^* - k_j}\right)$$
$$+ \frac{c_i^* e_j}{2}\left(\frac{\cosh(-(\alpha_i^* + k_j)h_1 + k_j H) - \cosh(-(\alpha_i^* + k_j)h_3 + k_j H)}{\alpha_i^* + k_j} + \frac{\cosh(-(\alpha_i^* - k_j)h_1 - k_j H) - \cosh(-(\alpha_i^* - k_j)h_3 - k_j H)}{\alpha_i^* - k_j}\right)$$
$$+ \frac{d_i^* e_j}{2}\left(\frac{\sinh(-(\alpha_i^* + k_j)h_1 + k_j H) - \sinh(-(\alpha_i^* + k_j)h_3 + k_j H)}{\alpha_i^* + k_j} + \frac{\sinh(-(\alpha_i^* - k_j)h_1 - k_j H) - \sinh(-(\alpha_i^* - k_j)h_3 - k_j H)}{\alpha_i^* - k_j}\right)$$
$$+ \frac{e_i^* a_j}{2}\left(\frac{\sinh(-(k_i^* + k_j)h_1 + k_i^* H) - \sinh(-(k_i^* + k_j)h_3 + k_i^* H)}{k_i^* + k_j} + \frac{\sinh(-(k_i^* - k_j)h_1 + k_i^* H) - \sinh(-(k_i^* - k_j)h_3 + k_i^* H)}{k_i^* - k_j}\right)$$
$$+ \frac{e_i^* b_j}{2}\left(\frac{\cosh(-(k_i^* + k_j)h_1 + k_i^* H) - \cosh(-(k_i^* + k_j)h_3 + k_i^* H)}{k_i^* + k_j} - \frac{\cosh(-(k_i^* - k_j)h_1 + k_i^* H) - \cosh(-(k_i^* - k_j)h_3 + k_i^* H)}{k_i^* - k_j}\right)$$
$$+ \frac{e_i^* c_j}{2}\left(\frac{\cosh(-(k_i^* + \alpha_j)h_1 + k_i^* H) - \cosh(-(k_i^* + \alpha_j)h_3 + k_i^* H)}{k_i^* + \alpha_j} - \frac{\cosh(-(k_i^* - \alpha_j)h_1 + k_i^* H) - \cosh(-(k_i^* - \alpha_j)h_3 + k_i^* H)}{k_i^* - \alpha_j}\right)$$
$$+ \frac{e_i^* d_j}{2}\left(\frac{\sinh(-(k_i^* + \alpha_j)h_1 + k_i^* H) - \sinh(-(k_i^* + \alpha_j)h_3 + k_i^* H)}{k_i^* + \alpha_j} + \frac{\sinh(-(k_i^* - \alpha_j)h_1 + k_i^* H) - \sinh(-(k_i^* - \alpha_j)h_3 + k_i^* H)}{k_i^* - \alpha_j}\right)$$

(F.63)

*part*3

$$= \frac{a_i^* a_j}{2}\left(\frac{\sinh(-(k_i^*+k_j)h_1)-\sinh(-(k_i^*+k_j)h_3)}{k_i^*+k_j}+\frac{\sinh(-(k_i^*-k_j)h_1)-\sinh(-(k_i^*-k_j)h_3)}{k_i^*-k_j}\right)$$

$$+\frac{b_i^* a_j}{2}\left(\frac{\cosh(-(k_i^*+k_j)h_1)-\cosh(-(k_i^*+k_j)h_3)}{k_i^*+k_j}+\frac{\cosh(-(k_i^*-k_j)h_1)-\cosh(-(k_i^*-k_j)h_3)}{k_i^*-k_j}\right)$$

$$+\frac{c_i^* a_j}{2}\left(\frac{\cosh(-(\alpha_i^*+k_j)h_1)-\cosh(-(\alpha_i^*+k_j)h_3)}{\alpha_i^*+k_j}+\frac{\cosh(-(\alpha_i^*-k_j)h_1)-\cosh(-(\alpha_i^*-k_j)h_3)}{\alpha_i^*-k_j}\right)$$

$$+\frac{d_i^* a_j}{2}\left(\frac{\sinh(-(\alpha_i^*+k_j)h_1)-\sinh(-(\alpha_i^*+k_j)h_3)}{\alpha_i^*+k_j}+\frac{\sinh(-(\alpha_i^*-k_j)h_1)-\sinh(-(\alpha_i^*-k_j)h_3)}{\alpha_i^*-k_j}\right)$$

$$+\frac{a_i^* b_j}{2}\left(\frac{\cosh(-(k_i^*+k_j)h_1)-\cosh(-(k_i^*+k_j)h_3)}{k_i^*+k_j}-\frac{\cosh(-(k_i^*-k_j)h_1)-\cosh(-(k_i^*-k_j)h_3)}{k_i^*-k_j}\right)$$

$$+\frac{b_i^* b_j}{2}\left(\frac{\sinh(-(k_i^*+k_j)h_1)-\sinh(-(k_i^*+k_j)h_3)}{k_i^*+k_j}-\frac{\sinh(-(k_i^*-k_j)h_1)-\sinh(-(k_i^*-k_j)h_3)}{k_i^*-k_j}\right)$$

$$+\frac{c_i^* b_j}{2}\left(\frac{\sinh(-(\alpha_i^*+k_j)h_1)-\sinh(-(\alpha_i^*+k_j)h_3)}{\alpha_i^*+k_j}-\frac{\sinh(-(\alpha_i^*-k_j)h_1)-\sinh(-(\alpha_i^*-k_j)h_3)}{\alpha_i^*-k_j}\right)$$

$$+\frac{d_i^* b_j}{2}\left(\frac{\cosh(-(\alpha_i^*+k_j)h_1)-\cosh(-(\alpha_i^*+k_j)h_3)}{\alpha_i^*+k_j}-\frac{\cosh(-(\alpha_i^*-k_j)h_1)-\cosh(-(\alpha_i^*-k_j)h_3)}{\alpha_i^*-k_j}\right)$$

$$+\frac{a_i^* c_j}{2}\left(\frac{\cosh(-(k_i^*+\alpha_j)h_1)-\cosh(-(k_i^*+\alpha_j)h_3)}{k_i^*+\alpha_j}-\frac{\cosh(-(k_i^*-\alpha_j)h_1)-\cosh(-(k_i^*-\alpha_j)h_3)}{k_i^*-\alpha_j}\right)$$

$$+\frac{b_i^* c_j}{2}\left(\frac{\sinh(-(k_i^*+\alpha_j)h_1)-\sinh(-(k_i^*+\alpha_j)h_3)}{k_i^*+\alpha_j}-\frac{\sinh(-(k_i^*-\alpha_j)h_1)-\sinh(-(k_i^*-\alpha_j)h_3)}{k_i^*-\alpha_j}\right)$$

$$+\frac{c_i^* c_j}{2}\left(\frac{\sinh(-(\alpha_i^*+\alpha_j)h_1)-\sinh(-(\alpha_i^*+\alpha_j)h_3)}{\alpha_i^*+\alpha_j}-\frac{\sinh(-(\alpha_i^*-\alpha_j)h_1)-\sinh(-(\alpha_i^*-\alpha_j)h_3)}{\alpha_i^*-\alpha_j}\right)$$

$$+\frac{d_i^* c_j}{2}\left(\frac{\cosh(-(\alpha_i^*+\alpha_j)h_1)-\cosh(-(\alpha_i^*+\alpha_j)h_3)}{\alpha_i^*+\alpha_j}-\frac{\cosh(-(\alpha_i^*-\alpha_j)h_1)-\cosh(-(\alpha_i^*-\alpha_j)h_3)}{\alpha_i^*-\alpha_j}\right)$$

$$+\frac{a_i^* d_j}{2}\left(\frac{\sinh(-(k_i^*+\alpha_j)h_1)-\sinh(-(k_i^*+\alpha_j)h_3)}{k_i^*+\alpha_j}+\frac{\sinh(-(k_i^*-\alpha_j)h_1)-\sinh(-(k_i^*-\alpha_j)h_3)}{k_i^*-\alpha_j}\right)$$

$$+\frac{b_i^* d_j}{2}\left(\frac{\cosh(-(k_i^*+\alpha_j)h_1)-\cosh(-(k_i^*+\alpha_j)h_3)}{k_i^*+\alpha_j}+\frac{\cosh(-(k_i^*-\alpha_j)h_1)-\cosh(-(k_i^*-\alpha_j)h_3)}{k_i^*-\alpha_j}\right)$$

$$+\frac{c_i^* d_j}{2}\left(\frac{\cosh(-(\alpha_i^*+\alpha_j)h_1)-\cosh(-(\alpha_i^*+\alpha_j)h_3)}{\alpha_i^*+\alpha_j}+\frac{\cosh(-(\alpha_i^*-\alpha_j)h_1)-\cosh(-(\alpha_i^*-\alpha_j)h_3)}{\alpha_i^*-\alpha_j}\right)$$

$$+\frac{d_i^* d_j}{2}\left(\frac{\sinh(-(\alpha_i^*+\alpha_j)h_1)-\sinh(-(\alpha_i^*+\alpha_j)h_3)}{\alpha_i^*+\alpha_j}+\frac{\sinh(-(\alpha_i^*-\alpha_j)h_1)-\sinh(-(\alpha_i^*-\alpha_j)h_3)}{\alpha_i^*-\alpha_j}\right)$$

(F.64)

The calculation of elements of matrix $\mathbf{Q}_9$

$$\begin{aligned}
&\tau_{xz3}(0,z)\\
&=\rho_{ice}\nu_{e3}\left(2\frac{\partial^2\varphi_3(0,z)}{\partial x\partial z}+\frac{\partial^2\psi_3(0,z)}{\partial z^2}-\frac{\partial^2\psi_3(0,z)}{\partial x^2}\right)\\
&=\sum_{n=1}^{N+2}2i\rho_{ice}\nu_{e3}k_3^2(n)T(n)\left(A_3(n)\sinh k_3(n)z+B_3(n)\cosh k_3(n)z\right)\\
&+\sum_{n=1}^{N+2}\rho_{ice}\nu_{e3}\alpha_3^2(n)T(n)\left(C_3(n)\cosh\alpha_3(n)z+D_3(n)\sinh\alpha_3(n)z\right)\\
&+\sum_{n=1}^{N+2}\rho_{ice}\nu_{e3}k_3^2(n)T(n)\left(C_3(n)\cosh\alpha_3(n)z+D_3(n)\sinh\alpha_3(n)z\right)
\end{aligned}$$

(F.65)

We define new vectors $\mathbf{a}$, $\mathbf{b}$, $\mathbf{c}$, $\mathbf{d}$, $\mathbf{k}$ and $\boldsymbol{\alpha}$ as follows

$$\mathbf{a}=(0,0,0,\cdots,0,2i\rho_{ice}\nu_{e3}k_3^2(1)A_3(1),2i\rho_{ice}\nu_{e3}k_3^2(2)A_3(2),\cdots,2i\rho_{ice}\nu_{e3}k_3^2(N+2)A_3(N+2))^T$$

(F.66)

$$\mathbf{b}=(0,0,0,\cdots,0,2i\rho_{ice}\nu_{e3}k_3^2(1)B_3(1),2i\rho_{ice}\nu_{e3}k_3^2(2)B_3(2),\cdots,2i\rho_{ice}\nu_{e3}k_3^2(N+2)B_3(N+2))^T$$

(F.67)

$$\mathbf{c}=(0,0,0,\cdots,0,\rho_{ice}\nu_{e3}(\alpha_3^2(1)+k_3^2(1))C_3(1),\rho_{ice}\nu_{e3}(\alpha_3^2(2)+k_3^2(2))C_3(2),\cdots,\rho_{ice}\nu_{e3}(\alpha_3^2(N+2)+k_3^2(N+2))C_3(N+2))^T$$

(F.68)

$$\mathbf{d}=(0,0,0,\cdots,0,\rho_{ice}\nu_{e3}(\alpha_3^2(1)+k_3^2(1))D_3(1),\rho_{ice}\nu_{e3}(\alpha_3^2(2)+k_3^2(2))D_3(2),\cdots,\rho_{ice}\nu_{e3}(\alpha_3^2(N+2)+k_3^2(N+2))D_3(N+2))^T$$

(F.69)

$$\mathbf{k}=\left(k_1(1),k_1(1),k_1(2),\cdots,k_1(N+2),k_3(1),k_3(2),\cdots,k_3(N+2)\right)^T \quad \text{(F.70)}$$

$$\boldsymbol{\alpha}=\left(\alpha_1(1),\alpha_1(1),\alpha_1(2),\cdots,\alpha_1(N+2),\alpha_3(1),\alpha_3(2),\cdots,\alpha_3(N+2)\right)^T \quad \text{(F.71)}$$

Then we can obtain

$$Q_{ij}^{9} = \int_{-h_3}^{-h_1} (a_i^* \sinh k_i^* z + b_i^* \cosh k_i^* z + c_i^* \cosh \alpha_i^* z + d_i^* \sinh \alpha_i^* z)(a_j \sinh k_j z + b_j \cosh k_j z + c_j \cosh \alpha_j z + d_j \sinh \alpha_j z) dz$$

$$= \frac{a_i^* a_j}{2} \left(\frac{\sinh(-(k_i^* + k_j)h_1) - \sinh(-(k_i^* + k_j)h_3)}{k_i^* + k_j} - \frac{\sinh(-(k_i^* - k_j)h_1) - \sinh(-(k_i^* - k_j)h_3)}{k_i^* - k_j} \right)$$

$$+ \frac{b_i^* a_j}{2} \left(\frac{\cosh(-(k_i^* + k_j)h_1) - \cosh(-(k_i^* + k_j)h_3)}{k_i^* + k_j} - \frac{\cosh(-(k_i^* - k_j)h_1) - \cosh(-(k_i^* - k_j)h_3)}{k_i^* - k_j} \right)$$

$$+ \frac{c_i^* a_j}{2} \left(\frac{\cosh(-(\alpha_i^* + k_j)h_1) - \cosh(-(\alpha_i^* + k_j)h_3)}{\alpha_i^* + k_j} - \frac{\cosh(-(\alpha_i^* - k_j)h_1) - \cosh(-(\alpha_i^* - k_j)h_3)}{\alpha_i^* - k_j} \right)$$

$$+ \frac{d_i^* a_j}{2} \left(\frac{\sinh(-(\alpha_i^* + k_j)h_1) - \sinh(-(\alpha_i^* + k_j)h_3)}{\alpha_i^* + k_j} - \frac{\sinh(-(\alpha_i^* - k_j)h_1) - \sinh(-(\alpha_i^* - k_j)h_3)}{\alpha_i^* - k_j} \right)$$

$$+ \frac{a_i^* b_j}{2} \left(\frac{\cosh(-(k_i^* + k_j)h_1) - \cosh(-(k_i^* + k_j)h_3)}{k_i^* + k_j} + \frac{\cosh(-(k_i^* - k_j)h_1) - \cosh(-(k_i^* - k_j)h_3)}{k_i^* - k_j} \right)$$

$$+ \frac{b_i^* b_j}{2} \left(\frac{\sinh(-(k_i^* + k_j)h_1) - \sinh(-(k_i^* + k_j)h_3)}{k_i^* + k_j} + \frac{\sinh(-(k_i^* - k_j)h_1) - \sinh(-(k_i^* - k_j)h_3)}{k_i^* - k_j} \right)$$

$$+ \frac{c_i^* b_j}{2} \left(\frac{\sinh(-(\alpha_i^* + k_j)h_1) - \sinh(-(\alpha_i^* + k_j)h_3)}{\alpha_i^* + k_j} + \frac{\sinh(-(\alpha_i^* - k_j)h_1) - \sinh(-(\alpha_i^* - k_j)h_3)}{\alpha_i^* - k_j} \right)$$

$$+ \frac{d_i^* b_j}{2} \left(\frac{\cosh(-(\alpha_i^* + k_j)h_1) - \cosh(-(\alpha_i^* + k_j)h_3)}{\alpha_i^* + k_j} + \frac{\cosh(-(\alpha_i^* - k_j)h_1) - \cosh(-(\alpha_i^* - k_j)h_3)}{\alpha_i^* - k_j} \right)$$

$$+ \frac{a_i^* c_j}{2} \left(\frac{\cosh(-(k_i^* + \alpha_j)h_1) - \cosh(-(k_i^* + \alpha_j)h_3)}{k_i^* + \alpha_j} + \frac{\cosh(-(k_i^* - \alpha_j)h_1) - \cosh(-(k_i^* - \alpha_j)h_3)}{k_i^* - \alpha_j} \right)$$

$$+ \frac{b_i^* c_j}{2} \left(\frac{\sinh(-(k_i^* + \alpha_j)h_1) - \sinh(-(k_i^* + \alpha_j)h_3)}{k_i^* + \alpha_j} + \frac{\sinh(-(k_i^* - \alpha_j)h_1) - \sinh(-(k_i^* - \alpha_j)h_3)}{k_i^* - \alpha_j} \right)$$

$$+ \frac{c_i^* c_j}{2} \left(\frac{\sinh(-(\alpha_i^* + \alpha_j)h_1) - \sinh(-(\alpha_i^* + \alpha_j)h_3)}{\alpha_i^* + \alpha_j} + \frac{\sinh(-(\alpha_i^* - \alpha_j)h_1) - \sinh(-(\alpha_i^* - \alpha_j)h_3)}{\alpha_i^* - \alpha_j} \right)$$

$$+ \frac{d_i^* c_j}{2} \left(\frac{\cosh(-(\alpha_i^* + \alpha_j)h_1) - \cosh(-(\alpha_i^* + \alpha_j)h_3)}{\alpha_i^* + \alpha_j} + \frac{\cosh(-(\alpha_i^* - \alpha_j)h_1) - \cosh(-(\alpha_i^* - \alpha_j)h_3)}{\alpha_i^* - \alpha_j} \right)$$

$$+ \frac{a_i^* d_j}{2} \left(\frac{\sinh(-(k_i^* + \alpha_j)h_1) - \sinh(-(k_i^* + \alpha_j)h_3)}{k_i^* + \alpha_j} - \frac{\sinh(-(k_i^* - \alpha_j)h_1) - \sinh(-(k_i^* - \alpha_j)h_3)}{k_i^* - \alpha_j} \right)$$

$$+ \frac{b_i^* d_j}{2} \left(\frac{\cosh(-(k_i^* + \alpha_j)h_1) - \cosh(-(k_i^* + \alpha_j)h_3)}{k_i^* + \alpha_j} - \frac{\cosh(-(k_i^* - \alpha_j)h_1) - \cosh(-(k_i^* - \alpha_j)h_3)}{k_i^* - \alpha_j} \right)$$

$$+ \frac{c_i^* d_j}{2} \left(\frac{\cosh(-(\alpha_i^* + \alpha_j)h_1) - \cosh(-(\alpha_i^* + \alpha_j)h_3)}{\alpha_i^* + \alpha_j} - \frac{\cosh(-(\alpha_i^* - \alpha_j)h_1) - \cosh(-(\alpha_i^* - \alpha_j)h_3)}{\alpha_i^* - \alpha_j} \right)$$

$$+ \frac{d_i^* d_j}{2} \left(\frac{\sinh(-(\alpha_i^* + \alpha_j)h_1) - \sinh(-(\alpha_i^* + \alpha_j)h_3)}{\alpha_i^* + \alpha_j} - \frac{\sinh(-(\alpha_i^* - \alpha_j)h_1) - \sinh(-(\alpha_i^* - \alpha_j)h_3)}{\alpha_i^* - \alpha_j} \right)$$

(F.72)

Appendix G: Muller method

In the present study, we employ the Muller method to find the roots of the dispersion relation. Because for large period wave the viscoelastic model's dominant roots are very close to open water case, we can first calculate the roots for the open water case and use it as the initial guess for the Muller method. The Muller method will find the accurate location of the roots for viscoelastic model.

Muller's method is a recursive method which generates an approximation of the root z of $F(z)$ at each iteration. Starting with three initial values z_0, z_1 and z_2, the first iteration calculates the first approximation z_1, the second iteration calculates the second approximation z_2, the third iteration calculates the third approximation z_3, etc. Hence the kth iteration generates approximation z_k. Each iteration takes as input the last three generated approximations and the value of $F(z)$ at these approximations. Hence the kth iteration takes as input the values z_{k-1}, z_{k-2} and z_{k-3} and the function values $F(z_{k-1})$, $f(z_{k-2})$ and $f(z_{k-3})$. The approximation z_k is calculated as follows.

A parabola $y_k(z)$ is constructed which goes through the three points (z_{k-1}, $F(z_{k-1})$), (z_{k-2}, $F(z_{k-2})$) and (z_{k-3}, $F(z_{k-3})$). $y_k(z)$ is

$$y_k(z) = F(z_{k-1}) + (z - z_{k-1})F[z_{k-1}, z_{k-2}] + (z - z_{k-1})(z - z_{k-2})F[z_{k-1}, z_{k-2}, z_{k-3}] \quad \text{(G.1)}$$

where $F[z_{k-1}, z_{k-2}]$ and $F[z_{k-1}, z_{k-2}, z_{k-3}]$ denote divided differences:

$$F[z_{k-1}, z_{k-2}] = \frac{F(z_{k-2}) - F(z_{k-1})}{z_{k-2} - z_{k-1}} \quad \text{(G.2)}$$

$$F[z_{k-1}, z_{k-2}, z_{k-3}] = \frac{F[z_{k-2}, z_{k-3}] - F[z_{k-1}, z_{k-2}]}{z_{k-3} - z_{k-1}} \tag{G.3}$$

Eq. (G.1) can be rewritten as

$$y_k(z) = F(z_{k-1}) + w(z - z_{k-1}) + F[z_{k-1}, z_{k-2}, z_{k-3}](z - z_{k-1})^2 \tag{G.4}$$

where

$$w = F[z_{k-1}, z_{k-2}] + F[z_{k-1}, z_{k-3}] + F[z_{k-2}, z_{k-3}] \tag{G.5}$$

The next iterate z_k is given as the solution closest to z_{k-1} of the quadratic equation $y_k(z) = 0$. This yields the recurrence relation

$$z_k = z_{k-1} - \frac{2F(z_{k-1})}{w \pm \sqrt{w^2 - 4F(z_{k-1})F[z_{k-1}, z_{k-2}, z_{k-3}]}} \tag{G.6}$$

In this formula, the sign should be chosen such that the denominator is as large as possible in magnitude. We do not use the standard formula for solving quadratic equations because that may lead to loss of significance.

We note that z_k can be complex, even if the previous iterates were all real. This is in contrast with other root-finding algorithms like the secant method, Sidi's generalized secant method or Newton's method, whose iterates will remain real if one starts with real numbers. Having complex iterates can be an advantage (if one is looking for complex roots) or a disadvantage (if it is known that all roots are real), depending on the problem.

Appendix H: A parameterization based on OGCM

The oceanic general circulation model (OGCM) is a numerical model to study the behavior of ocean at the mesoscale and global scale. The two-dimensional momentum equations for sea ice are obtained by integrating the 3D equations through the thickness of the ice in the vertical direction. In this model, the momentum equation of the ice cover needs to be solved as an integral part of the model [108, 109]. In the ice momentum equation, the internal stress in sea ice dynamics model was an active research topic during the 1980s [108]. The most widely used ice dynamics model at present is the one adopted in the model CICE [109]: the Los Alamos sea ice model, in which, the internal stress follows that developed by Hibler [108] where for viscous-plastic model:

$$\tau_{mn} = -p\delta_{mn}/2 + (\lambda - \mu)\delta_{mn}\dot{S}_{ll} + 2\mu\dot{S}_{mn} \tag{H.2}$$

or equivalently:

$$\frac{1}{2\mu}\tau_{mn} + \frac{\mu - \lambda}{4\mu\lambda}\tau_{ll}\delta_{mn} + \frac{p}{4\lambda}\delta_{mn} = \dot{S}_{mn} \tag{H.3}$$

and for elastic-viscous-plastic model [105]

$$\frac{1}{E}\frac{d\tau_{mn}}{dt} + \frac{1}{2\mu}\tau_{mn} + \frac{\mu - \lambda}{4\mu\lambda}\tau_{ll}\delta_{mn} + \frac{p}{4\lambda}\delta_{mn} = \dot{S}_{mn} \tag{H.4}$$

Here, $\boldsymbol{\tau}$ is the internal stress tensor of sea ice, p is the average of normal stresses from the internal ice stress, and $\dot{S}_{mn}$ is the strain rate tensor. λ and μ are the nonlinear bulk and shear viscosities. E is Young's modulus.

This formulation is based on phenomenological arguments. It has been calibrated using the observed ice kinematics via remote sensing. Since the internal ice stress is a physical quantity, as suggested by Erick Roger of the Naval Research Office [personal

communications] its formulation should be consistent whether it appears in the ice dynamics or in the wave ice interactions. The study of such ice model may provide additional information to improve parameterization in wave ice interaction models.

The physical parameters in elastic-viscous-plastic sea ice model are as the following [110]

$$\lambda = \frac{P}{2\Delta}, \quad \mu = \frac{P}{2\Delta e^2}. \tag{H.5}$$

Here,

$$\Delta = \sqrt{D_D^2 + \left(D_T^2 + D_S^2\right)/e^2} \tag{H.6}$$

$$D_D = \dot{S}_{11} + \dot{S}_{22} \tag{H.7}$$

$$D_T = \dot{S}_{11} - \dot{S}_{22} \tag{H.8}$$

$$D_S = 2\dot{S}_{12} \tag{H.9}$$

$\dot{S}_{ij}$ is the strain rate tensor. In the spherical coordinate, we have [111]

$$D_S = \frac{1}{r_0 \cos\phi_0}\frac{\partial v}{\partial \theta_0} + \frac{1}{r_0}\frac{\partial u}{\partial \phi_0} + \frac{u}{r_0}\tan\phi_0 \tag{H.10}$$

$$D_T = \frac{1}{r_0 \cos\phi_0}\frac{\partial u}{\partial \theta_0} - \frac{1}{r_0}\frac{\partial v}{\partial \phi_0} - \frac{v}{r_0}\tan\phi_0 \tag{H.11}$$

$$D_D = \frac{1}{r_0 \cos\phi_0}\frac{\partial u}{\partial \theta_0} + \frac{1}{r_0}\frac{\partial v}{\partial \phi_0} - \frac{v}{r_0}\tan\phi_0 \tag{H.12}$$

Here, ϕ_0 is latitude, and θ_0 is longitude. r_0 is the radius of earth. First order finite difference method is employed to calculate spatial derivative. Then, the elasticity and viscosity are

$$E = \frac{\lambda}{T_c}, \; \nu_{ice} = \frac{\mu}{\rho_{ice}} \tag{H.13}$$

Here, P, u and v are read from input file. Parameter settings are as $T_c = 1200s$, $e = 2$. We used a data set provide by Rogers to test this idea. The resulting elasticity and viscosity paramters are shown in the figure below.

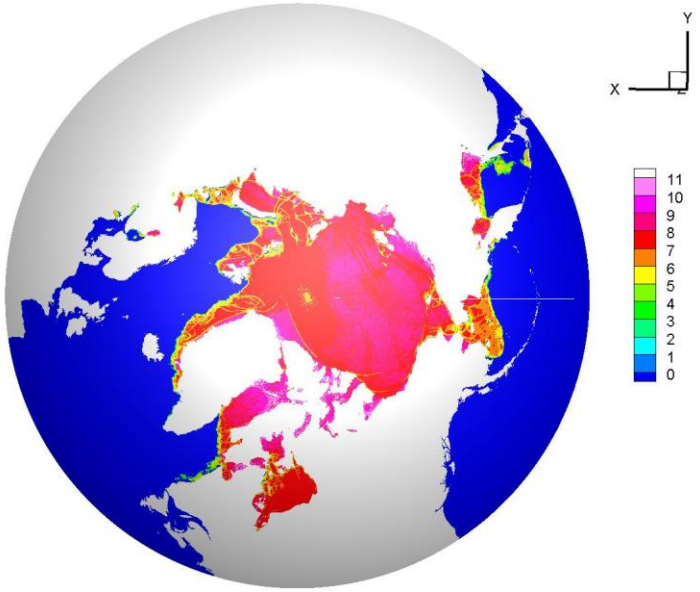

Fig. H-1 computed effective elasticity of Arctic ice cover in log scale.

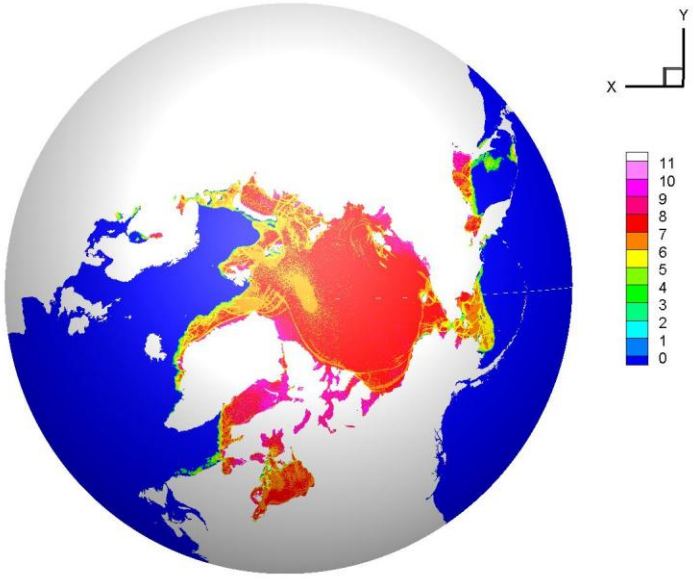

Fig. H-2 computed effective viscosity of Arctic ice cover in log scale.

From Fig. H-1 and H-2, the magnitude of the elasticity is found to be reasonable, but the viscosity has a very large order magnitude. But this is also obtained from oceanic general circulation model, in which the maximum cutoff value of the effective viscosity is 10^9 m^2/s. The large magnitude for the viscosity may be caused by the setting of e. e is the yield curve aspect ratio. For most sea ice models, e equals to 2 fits the observed ice kinematics well. Since the fitting is largely controlled by the over-all ice kinematics, for marginal ice zone applications, different calibration values may apply.

The method for parameterization is a simple way to obtain viscoelastic parameters. This is based on the assumption that the sea ice model in oceanic general circulation model is well calibrated for the parameters. However, lacking such calibration information, we still need to explore the direct relation of ice morphology and ice parameters to examine the parametrization method described in this study.